MODELING OF WORMHOLE PROPAGATION IN DOLOMITE RESERVOIRS

A Dissertation

by

MAHMOUD TAHA ALI

Submitted to the Office of Graduate and Professional Studies of
Texas A&M University
in partial fulfillment of the requirements for the degree of

DOCTOR OF PHILOSOPHY

Chair of Committee,	Hisham A. Nasr-El-Din
Committee Members,	Stephen A. Holditch
	Jerome Schubert
	Mahmoud El-Halwagi
Head of Department,	Jeff Spath

August 2019

Major Subject: Petroleum Engineering

ABSTRACT

The two-scale continuum (TSC) model for simulating carbonate acidizing gained substantial attention recently. The previous studies mainly dealt with matching experimental homogenous limestone experiments. The previous work only considered the pore volume to breakthrough (PVBT) to match experimental results and assumed linear kinetics for HCl-carbonate. The objectives of the current study are to 1) build a robust model for dolomite matrix acidizing simulation, 2) account for the effect of rock types in the TSC model, 3) study acid performance under field scale, 4) modify the traditional upscaling schemes utilizing the TSC model, and 5) quantify the effect of wormhole growth in vuggy and naturally fractured using field scale radial model.

Unlike previous studies, experiments were performed on 6 in. length and 1.5 in. diameter vuggy dolomite cores at two sets of temperatures (150 & 200ºF) and acid concentrations (15 and 20 wt% HCl). Computer tomography (CT) was used to generate porosity distribution and non-linear reaction kinetics was applied. The acid reaction rate and diffusion coefficient were modified based on X-ray fluorescence (XRF) results and effluent chemical analysis. Wormhole 3D shape and experimental PVBT were used to assess the quality of model results.

The tuned model was used to simulate a hypothetical 18 in. core as well as large scale radial experiments to assess its prediction capabilities, and then the model was utilized to predict the dolomite acidizing performance under field conditions. Simulation results were compared with traditional 1-D models. Finally, the radial model were used

to simulate multiple cases including vugs and natural fractured to assess the effect on the acidizing process.

The simulation runs emphasize that the exclusion of the wormhole shape and branching from the matching process results in an unrealistic match. It is important to simulate the cylindrical shape of the core using the actual porosity distribution to capture the wormhole growth, which is increasingly important when the wormhole propagates near the core perimeter.

The radial field scale model results show that the optimum velocity can be higher or lower than those predicted from lab experiments. Accordingly, caution must be taken when linear core flood data is used to predict acid propagation in the field. The simulations showed that traditional upscaling models over predict acid volumes, as the predicted volumes are double at moderate to high injection rates. Models using statistically distributed porosity can provide accurate acid propagation predictions, with a relative percentage error less than 25% at extremely high injection rates.

The simulation results of vuggy carbonates show that the presence of vugs results in faster and deeper acid propagation in the formation when compared with homogenous reservoirs at injection velocities lower than 8E-4 m/s. Results also revealed that the size and density of the vugs have a significant impact on acid consumption and the overall performance of the acid treatment. The output of the fractured model illustrates that under field conditions, fracture orientations do not affect the acid propagation velocity. The acid does not touch all the fractures around the well.

Current model was able to match multiple sets of experiments (Dolomite and Limestone) and follow the experimental trend of longer cores and large-scale radial experiments. It was used to predict acid performance under field conditions and to adjust the traditional upscaling models. The effect of vugs and natural fractures on carbonate acidizing was quantified utilizing the field scale model. A new workflow for carbonate matrix acidizing based on petrophysical, experimental, and simulation results is introduced.

DEDICATION

This dissertation is dedicated to

My Beloved wife (Soha Ali), for her love and endless support, I wouldn't have finished

my PhD without her;

My beloved parents (Taha and Khairia) for their support and love;

My dear son (Hamza), for his accompany and being a good friend of mine;

My dear daughter (Hla), for making my life joyful;

My sister (Lamia), for her love and support;

My brothers (Ahmed and Mohamed), for their support and encouragement;

ACKNOWLEDGEMENTS

CONTRIBUTORS AND FUNDING SOURCES

Contributors

This work was supervised by a dissertation committee consisting of Professor Hisham A. Nasr-El-Din [advisor] and Stephen A. Holditch and Jerome J. Schubert of the Department of [Home Department] and Professor Mahmoud M. El-Halwagi of the Department of [Outside Department].

All work conducted for the dissertation was completed by the student independently.

Funding Sources

NOMENCLATURE

a   Parameter in the Freundlich isotherm, 1/T, K^{-1}

a_{vo} Initial interfacial area per unit volume of the medium, 1/L, m^{-1}

a_v Interfacial area per unit volume of the medium, 1/L, m^{-1}

C   Covariance function

C/C_0 Normalized tracer concentration

C_f Original concentration of acid in the fluid phase, n/L^3, mol/L

C_s Concentration of acid at the solid-fluid interface, n/L^3, mol/L

CT   Computed tomography

Da   Damköhler number defined as the ratio of reaction rate to convection rate

De   Effective dispersion tensor, L^2/t, m^2/s

DeX   Effective longitudinal dispersion coefficient, L^2/t, m^2/s

DeT   Effective transverse dispersion coefficient, L^2/t, m^2/s

D_m Acid diffusivity, L^2/t, m^2/s

E   Activation energy, mL^2/nt^2, J/mol

K   Permeability tensor, L^2, m^2

K   Covariance matrix of the GP model

k   Vector of covariances

K_c Local mass transfer coefficient, L/t, m/s

k_f Actual fracture permeability, L^2, m^2

K_o Initial permeability tensor, L^2, m^2

viii

k_r	Rock permeability, L^2, m^2
k_t	Total (simulated fracture) permeability, L^2, m^2
k_s	Surface dissolution reaction rate constant, L/t, m/s
k_{so}	Frequency factor, L/t, m/s
n	Reaction exponent
N	Number of simulation runs conducted.
P	Dimension of the input data
PV	Pore volume
PVBT	Pore volume to breakthrough
Q	Acid injection rate, L^3/t, m^3/s
R	Universal gas constant, mL^2/nTt^2, J/mol/K
$R(C_s)$	Reaction rate, $n/t/L^2$, mol/s/m^2
Re_p	Pore scale Reynold's number
r_{po}	Initial pore radius, L, m
r_p	Pore radius, L, m
Sc	Schmidt number
Sh	Sherwood number
Sh_∞	Asymptotic Sherwood number
T	Absolute temperature, T, K
TSC	Two-scale continuum
U	Superficial velocity vector, L/t, m/s
w_r	Width of the rock (simulated fracture), L, m

w_f	Width of the actual fracture, L, m
X_m	Parameter in the Freundlich isotherm, mL^2/nt^2, J/mol
x*	Untried test location at which a prediction is desired.
Y	Vector of outputs
$\hat{Y}(x^*)$	Prediction of the GP model at any untried test location x^*
α	Dissolving power of acid, m/n, g/mol
$α_{os}$	Constant in dispersion correlations
β	Pore broadening parameter
γ	Pore-connectivity parameter
$σ^2$	Variance parameter in the GP covariance function
$θ_i$	Scale parameter in the GP covariance function
E	Porosity of the porous medium
ρ	Fluid density, m/L^3, kg/m3
$ρ_s$	Rock density, m/L^3, kg/m3
λX	Constant in the axial dispersion correlation
λT	Constant in the transverse dispersion correlation
μ	Fluid viscosity, m/Lt, mPa.s
ν	Kinematic viscosity, L^2/t, m^2/s

TABLE OF CONTENTS

LIST OF FIGURES

LIST OF TABLES

1. INTRODUCTION [1]

Oil and gas wells are prone to damage while drilling, completion, or during the life of the well due to the injection of incompatible fluids or poor production practices. Based on the source of the damage and reservoir depth and conditions, wells are treated or stimulated to by-pass/remove the damage and restore the performance of these wells. Among these stimulation methods is acidizing, which is divided into matrix acidizing and acid fracturing according to whether the injection pressure is below or above the formation fracturing pressure. The aim of matrix acidizing in carbonates is to bypass the damage by generating highly conductive channels called wormholes. In the oil and gas industry HCl solutions are usually used as acidizing fluids, but reservoir, fluids, and completion conditions may dictate the use of organic acids, chelating agents, or emulsified acids.

The understanding of the carbonate acidizing process was acquired through experimental work. Lund et al. (1973, 1975) studied the reaction kinetics of HCl solutions with both dolomite and limestone cores at different temperatures. Daccord (1987) studied the dissolution of plaster porous medium with de-ionized water in a radial geometry. Hoefner and Fogler (1988) conducted a set of experiments on both limestone and dolomite cores on linear mode. Wang et al. (1993) investigated the effect of injection rate, acid concentration, rock mineralogy, and temperature on the volume of

---

1 Partially reprinted with permission from "A Robust Model to Simulate Dolomite-Matrix Acidizing" by M. Ali and H. Nasr-El-Din, 2019. SPE-191136-PA, Copyright 2019 by Society of Petroleum Engineers.

acid required to fully penetrate a linear core. Fredd and Fogler (1999) conducted experiments to study the performance of organic acids and chelating agents as carbonate acidizing alternatives for HCl solutions. Bazin (2001) showed the effect of acid concentration, temperature, and permeability on acid efficiency curves. Taylor et al. (2006) had an insight on the effect of clays on acid reactivity with carbonates. A large-scale radial experiments were conducted on both dolomite and limestone samples by McDuff et al. (2010). Zakaria et al. (2015) showed the effect of carbonates pore structure on acidizing performance.

Many researchers translated their understanding of the acidizing phenomena into mathematical models to predict optimum injection rate, dissolution pattern, and/or to monitor the propagation of the wormhole (Hoefner and Fogler 1988; Hung et al. 1989, Daccord et al. 1993; Wang et al. 1993, Buijse 2000; Liu et al. 1997; Huang et al. 1997; Fredd and Fogler 1998, 1999; Golfier et al. 2002; Panga et al. 2002, 2005; Buijse and Glasbergen 2005; Kalia and Balakotaiah 2007, 2009; Izgec et al. 2010; Maheshwari et al. 2012, 2016; Furui et al. 2012; Tansey 2014; Wu et al. 2015; Ghommem et al. 2015, 2016; Akanni et al. 2017; Schwalbert et al. 2017; Mahrous et al. 2017; Beletskaya et al. 2017). For an extensive review of the different models and their applicability limits, we refer to Akanni and Nasr-El-Din (2015), and Fredd and Miller (2000). According to Akanni and Nasr-El-Din (2015), there are seven categories for carbonate acidizing models; the capillary tube approach, Damköhler number approach, transition pore theory, network models, Péclet number approach, semi-empirical approach, and two-scale (averaged continuum) models. The last two categories are the most used. The semi-

empirical for its simplicity and the two scale models as it captures the physics and flow mechanics of the acidizing process.

Buijse and Glasbergen (BG) (2005) introduced the first semi-empirical model for designing acid treatments. The model was based on matching experimental data. BG model requires information about optimum conditions from linear lab experiments to design field treatments. Tardy et al. (2007) conducted both linear and radial experiments and the results of the study demonstrated that BG model over-predicts acid volumes required. The outcome of Tardy et al. (2007) study was to multiply the wormhole velocity from BG model by a factor to obtain a more realistic result. Furui et al. (2012) conducted a comprehensive study based on experiments, field data, and numerical simulations. Unlike Tardy et al. (2007), they found that BG model underestimates the propagation velocity of the wormhole in carbonate wells. Furui et al. (2012) model requires lab experiments and information about the number of wormholes around the wellbore and wormholes diameter.

The two-scale models gained substantial attention lately for their capabilities of capturing the different dissolution patterns and accurately matching the pore volume of acid to breakthrough. The two-scale model was introduced by Liu et al. (1997) to model sandstone acidizing, but it was shown that it can capture the wormholing phenomenon in carbonates, as well. The main drawback of their model is that the effect of mass transfer on the reaction rate was not considered. Golfier et al. (2002) extended the work to develop a 3D linear model for carbonates, but their model ignored the reaction kinetics. Panga et al. (2002, 2005) developed a model that captures both mass

transfer and reaction kinetics, and built a 2D model. The work was extended by Kalia and Balakotaiah (2007) to simulate 2D radial flow, while Cohen et al. (2008) considered 3D radial flow simulations. Maheshwari et al. (2013) extended the work further to include 3D simulations. Their model showed a good match in comparison with Fredd and Fogler (1998) experimental data, which used uniform porosity distribution and changed the exponents of Carman-Kozeny correlation to tune the model. Ghommem et al. (2015) used Panga et al. (2002, 2005) model to match limestone acidizing experiments. The porosity was populated from the CT scan, and the same matching parameters as Maheshwari et al. (2012) were used. While the model PVBT matches well, it couldn't capture the wormhole tortuous path. Safari et al. (2014, 2016) performed a set of core flood experiments on dolomite cores from a gas reservoir in Iran, and they used the two-scale model to simulate the face dissolution of a dolomite core.

Liu et al. (2012) examined the effect of normally distributed porosities on wormholing patterns using radial geometry, and they showed that a substantial difference exists in PVBT between normally and uniformly distributed porosity models. Ghommem et al. (2015) mentioned in their study that porosity was distributed from CT scans, but they gave no elaboration or references for that step. Liu et al. (2016) used a spatial correlation for porosity distribution, the PVBT was similar to the case with uniform distribution, but they showed that wormhole shapes are closer to the experimental results.

Unlike the Panga et al. (2002, 2005) model, which relied on Darcy's equation for describing the fluid flow, De Oliveira et al. (2012), Wu et al. (2015), Akanni et al.

4

(2017) and Schwalbert et al. (2017) used Navier-Stokes equation with their two-scale model. Wu et al. (2015) compared the wormhole simulation with the Darcy and Darcy-Brinkman-Frochheimer (DBF) equation (an extended form of Navier-Stokes equation) and concluded that DBF equation gives more accurate simulations than Darcy equation for carbonate acidizing. Akanni et al. (2017) concluded that simulations with Navier-Stokes equation at very high injection rates require less wall-clock runtime when qualitatively compared with the Darcy equation (Maheshwari and Balakotaiah 2013).

Previous work on carbonate simulation (Maheshwari et al. 2012, 2016; Ghommem et al. 2015; Schwalbert et al. 2017) considered only limestone experiments. Those studies simulated the core as cuboid and assumed linear reaction kinetics for the HCl-CaCO3 reaction. These studies relied on changing Carman-Kozeny exponents to match acidizing experiments.

In the current study, two sets of experiments were performed on vuggy dolomitic cores using straight acid. The core was modeled as a cylinder inscribed inside a rectangular cube and porosity was generated from CT scans. The non-linear kinetics were included in our simulations and the reaction rate and diffusion coefficient were modified to match acidizing experiments. This combination of domain shape, porosity distribution, non-linear kinetics, and matching parameters were found to provide high quality and reliable match for both PVBT and wormhole 3D path. Also, the two-scale model was used to predict the acid performance in different limestone rock types. The tuned dolomite model was used to conduct simulations under radial flow conditions, and to study dolomite acidizing performance under field conditions. Finally, the effects of

vugs and natural fractures on the acidizing process were studied in Dolomite formations

using the radial model.

2. OBJECTIVES

The objectives of the present study are to: 1) Build a robust model for dolomite matrix acidizing simulation that matches both PVBT and wormhole shape, 2) Predict acid propagation in carbonate rocks based on the actual porosity distribution, 3) Utilize the tuned model to predict acid behavior under field scale, 4) Assess/Modify the prediction capabilities of the semi-empirical upscaling models, and 5) Quantify the effect of vugs and natural fractures on acid propagation under field scale.

3. TWO-SCALE MODEL USING NAVIER-STOKES FORMULATION[2]

3.1. Model Description

Current simulations were conducted using ANSYS FLUENT, a computational fluid dynamics (CFD) software. In ANSYS FLUENT, the flow field is described by Navier-Stokes momentum formulation. The equations for the Darcy scale and pore-scale are presented below.

3.1.1. Darcy Scale Equations

The fluid flow field is given by the Navier-Stokes formulation:

$$\frac{\partial(\rho\mathbf{u})}{\partial t} + \nabla \cdot (\rho\mathbf{uu}) = -\nabla p + \mu\nabla^2\mathbf{u} - \frac{\mu}{K}\mathbf{u} \dots\dots\dots\dots\dots\dots\dots\dots\dots\dots\dots\dots\dots\dots \textbf{Equation 1}$$

Where **u** is the superficial velocity vector, ρ is the fluid density, K is the permeability tensor, p is pressure, and μ is the fluid viscosity. The left-hand side of **Equation 1** accounts for the change in momentum where the first term is the rate of change and the second term is the convective acceleration. The right-hand side of Equation 1 accounts for the forces acting on the fluid where the three terms are the pressure drop, diffusion, and the Darcian losses, respectively. The porous medium inertial term was not included in the model, as it is only effective at extremely high velocities. In laminar flow through porous media, where the pressure drop becomes proportional to velocity, the convective acceleration and diffusion terms can be ignored and the model reduces to Darcy's equation. In the wormholes, the diffusion term becomes dominant, while the Darcian losses become negligible as permeability approaches infinity.

---

2 Partially reprinted with permission from "A Robust Model to Simulate Dolomite-Matrix Acidizing" by M. Ali and H. Nasr-El-Din, 2019. SPE-191136-PA, Copyright 2019 by Society of Petroleum Engineers.

The continuity, **Equation 2**, derived from the mass balance of fluids, accounts for the effect of local volume change during dissolution on the flow field:

$$\frac{\partial \varepsilon}{\partial t} + \nabla \cdot \mathbf{u} = 0 \; \ldots \ldots \ldots \ldots \ldots \ldots \ldots \ldots \ldots \ldots \ldots \ldots \ldots \ldots \ldots \ldots \ldots . \ldots \ldots \ldots \ldots \ldots . . \ldots \quad \textbf{Equation 2}$$

The Darcy scale description of the transport of acid species, from fluid phase balance of reacting acid species, is given by:

$$\underbrace{\varepsilon \frac{\partial C_f}{\partial t}}_{} + \underbrace{\mathbf{u} . \nabla C_f}_{} = \underbrace{\nabla \cdot \left(\varepsilon \mathbf{D_e} \cdot \nabla C_f \right)}_{} - \underbrace{k_c a_v \left(C_f - C_s \right)}_{} \ldots \ldots \ldots \ldots \ldots \ldots \ldots \ldots . \ldots \ldots \textbf{Equation 3}$$

| Acid Accumulation | Acid convection | Acid dispersion | Amount of acid transported to the rock surface from the fluid phase |

Where ε is the porosity of the medium, C_f is the concentration of the acid in the fluid phase, C_s is the concentration of the acid at the fluid-solid interface, $\mathbf{D_e}$ is the effective dispersion tensor, k_c is the local mass-transfer coefficient, and a_v is the interfacial area available for reaction per unit volume of the medium.

The local mass transfer and effective dispersion coefficients are obtained using correlations developed by Gupta and Balakotaiah (2001) and Balakotaiah and West (2002):

$$Sh = \frac{2 k_c r_p}{D_m} = Sh_\infty + 0.7 Re_p^{1/2} Sc^{1/3} \; \ldots \ldots \ldots \ldots \ldots \ldots \ldots \ldots \ldots \ldots \ldots \ldots \ldots . \ldots \ldots \textbf{Equation 4}$$

$$\mathbf{D_{eX}} = \alpha_{os} D_m + \frac{2 \lambda_X \|\mathbf{u}\| r_p}{\varepsilon} \; \ldots \ldots \ldots \ldots \ldots \ldots \ldots \ldots \ldots . . \ldots \ldots \ldots \ldots . \ldots \ldots \ldots . . \textbf{Equation 5}$$

$$\mathbf{D_{eT}} = \alpha_{os} D_m + \frac{2 \lambda_T \|\mathbf{u}\| r_p}{\varepsilon} \; \ldots \ldots \ldots \ldots \ldots \ldots \ldots \ldots . \ldots \ldots . . \ldots \ldots \ldots \ldots . . \ldots \ldots \ldots . \textbf{Equation 6}$$

Where *Sh* is the Sherwood number or dimensionless mass-transfer coefficient, r_p is the pore radius, D_m is the acid diffusivity, *Sh_∞* is the asymptotic Sherwood number, *Re_p* is the pore scale

Reynold's number defined by $\text{Re}_p = \frac{2\|u\|r_p}{v}$, and Sc is the Schmidt number given by $Sc = \frac{v}{D_m}$, v is the kinematic viscosity, α_{os} is a constant that depends on the structure of the porous medium (pore connectivity); D_{eX} is the longitudinal dispersion coefficient; D_{eT} is the transverse dispersion coefficient in the y- and z- directions; λ_X and λ_T are constants that depend on the structure of the medium. **Equations 4** through **6** account for both diffusive and convective contributions (Maheshwari and Balakotaiah 2013).

The reaction rate in **Equation 7** balances the amount of acid transferred from the fluid phase to the surface to the amount reacted at the surface:

$$k_c(C_f - C_s) = R(C_s) \ldots\ldots\ldots\ldots\ldots\ldots\ldots\ldots\ldots\ldots\ldots\ldots\ldots\ldots\ldots\ldots\ldots\ldots\ldots \textbf{Equation 7}$$

The porosity evolution equation as derived from the balance between the solid dissolved and fluid consumed, is given by:

$$\frac{\partial \varepsilon}{\partial t} = \frac{R(C_s)a_v\alpha}{\rho_s} \ldots\ldots\ldots\ldots\ldots\ldots\ldots\ldots\ldots\ldots\ldots\ldots\ldots\ldots\ldots\ldots\ldots \textbf{Equation 8}$$

$R(C_s)$ represents the reaction rate, ρ_s is the density of the rock, and α is the dissolving power of the acid. The reaction rate equation can be written as $R(C_s) = k_s C_s^n$ (where k_s is the dissolution rate constant and n is the reaction exponent).

The dissolution rate constant and the reaction exponent are obtained for HCl-dolomite system using correlations developed by Lund et al. (1973):

$$k_s = k_{so}e^{-\frac{E}{RT}} \ldots\ldots\ldots\ldots\ldots\ldots\ldots\ldots\ldots\ldots\ldots\ldots\ldots\ldots\ldots\ldots\ldots \textbf{Equation 9}$$

$$n = \frac{RT}{(1-aT)X_m} \ldots\ldots\ldots\ldots\ldots\ldots\ldots\ldots\ldots\ldots\ldots\ldots\ldots\ldots\ldots\ldots \textbf{Equation 10}$$

Where k_{so} is the frequency factor, E is the activation energy, R is the ideal gas constant, T is the absolute temperature, and a and X_m are parameters in the Freundlich isotherm. For HCl-Limestone system, the reaction exponent was set equal to 0.63 as proposed by Lund et al. (1975).

3.1.2. Pore Scale Equations

The acid propagation through the porous medium dissolves part of the solid phase. That acid reaction increases the rock porosity, which results in changes in permeability, pore-radius, and interfacial surface area per unit volume. The relationship between these rock properties and porosity are adapted from the Carman-Kozeny correlation and are given by the following pore scale equations (Maheshwari and Balakotaiah 2013):

$$\frac{K}{K_o} = \left(\frac{\varepsilon}{\varepsilon_o}\right)^{\gamma} \left(\frac{\varepsilon(1-\varepsilon_o)}{\varepsilon_o(1-\varepsilon)}\right)^{2\beta} \dots\dots\dots\dots\dots\dots\dots\dots\dots\dots\dots\dots\dots\dots \textbf{Equation 11}$$

$$\frac{r_p}{r_{po}} = \left(\frac{\varepsilon(1-\varepsilon_o)}{\varepsilon_o(1-\varepsilon)}\right)^{\beta} \dots\dots\dots\dots\dots\dots\dots\dots\dots\dots\dots\dots\dots\dots\dots \textbf{Equation 12}$$

$$\frac{a_v}{a_{vo}} = \left(\frac{\varepsilon}{\varepsilon_o}\right) \left(\frac{\varepsilon(1-\varepsilon_o)}{\varepsilon_o(1-\varepsilon)}\right)^{-\beta} \dots\dots\dots\dots\dots\dots\dots\dots\dots\dots\dots\dots\dots \textbf{Equation 13}$$

Where γ is the pore-connectivity parameter, and β is the pore broadening parameter.

3.1.3. Initial and Boundary Conditions

To solve Equations 1 and 3, boundary conditions should be defined at the inlet, outlet and side walls. At model inlet, a constant acid concentration is injected at a constant velocity, while a constant pressure is applied at the outlet. In the transverse direction, a no flow boundary condition is applied. Before injection, acid concentration is zero all over the domain with an initial porosity obtained from Computer Tomography (CT) scans or uniformly distributed, as will be shown below.

3.2. Comparison with Previous Studies

Carbonate acidizing models utilizing Navier-Stokes formulation were proven to capture all dissolution patterns occurring during the acidizing process (De Olivera, 2012; Akanni et al. 2017). The model accuracy was studied by Wu et al. (2015). In the current section, the simulation runs conducted by Maheshwari et al. (2012) will be reproduced. We built a rectangular cube of 3.5 cm x 1.4 cm x 1.4 cm and was divided into 540,000 grid blocks. The simulations were run on Texas A&M University (TAMU) High Performance Research Computing (HPRC) clusters. The time step used ranged from 2 seconds for the highest injection rate to 50 seconds at the lowest injection rate. The wall-clock runtime using 8 processing cores was in days at very low injection rates, about 10 hours around the optimum rate, and about 3 hours at the very high injection rate. In comparison with Maheshwari et al. (2012) and Ghommem et al. (2015) simulation models, which were based on Darcy's law, the current model is less computationally expensive at very high injection rates. This finding was noticed by Akanni et al. (2017) based on a qualitative comparison.

The porosity distribution and all model parameters were extracted from Maheshwari et al. (2012). In their work, they defined the breakthrough of the acid as a 50 time decrease in the pressure drop across the core from the initial value. **Figure 1** shows a plot of the PVBT versus the inverse of Damköhler number (Da), defined as the ratio between reaction rate and convective mass transport rate, for the Maheshwari et al. (2012) and current model simulations. Current model PVBT is always lower than the Maheshwari et al. (2012) model, because our model uses Navier-Stokes equation, which simultaneously considers flow through porous media and wormholes. Wu et al. (2015) highlighted the advantages of using Navier-stokes in comparison with Darcy simulations.
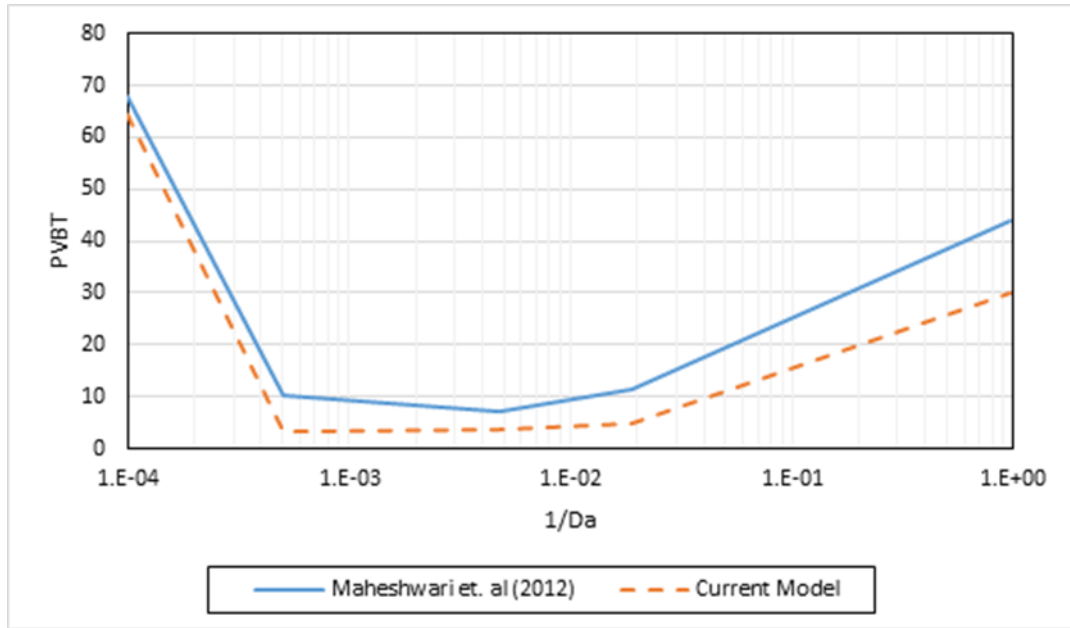
Figure 1 Acid efficiency curves. A comparison of present work with Maheshwari et al. (2012) simulation results.

4. EXPERIMENTAL STUDIES[3]

4.1. Core-flood Experiments

Silurian dolomite cores of 6 in. length and 1.5 in. diameter were used to conduct linear acidizing coreflood experiments with regular 15 wt% HCl acid at 150^0F and regular 20 wt% HCl acid at 200^0F. After cutting the cores, they were dried in an oven for minimum 6 hours at 200^0F, then were completely saturated for 4 hours in deionized water (resistivity of 18.2 MΩ.cm at room temperature) obtained from an in-house purification water unit. The weight difference method was used to calculate porosity and pore volume. The cores were imaged using a CT scanner before and after saturation. The stimulation hydrochloric acid was prepared by diluting a 36.46 wt% ACS grade HCl with deionized water. 1 wt% corrosion inhibitor was added to protect equipment from corrosion.

The core flood setup used is shown in **Figure 2**. A back pressure of 1,200 psi was applied to keep most of CO_2 in solution. A confinement pressure of 1,800 psi was applied to ensure that no fluids bypass the core. First, deionized water was injected at room temperature at 3 different injection rates (3, 5, and 7 cm^3/min) to measure core permeability. Then, the system was heated to 150^0F for 3 hours while injecting deionized water and waiting for pressure stabilization. Finally, acid solution was injected while monitoring the pressure drop using a pressure transducer; the acid breakthrough was marked by a negligible pressure drop across the core. **Tables 1 and 2** summarize the dolomite cores properties and core flood experiment results,

---

3 Partially reprinted with permission from "A Robust Model to Simulate Dolomite-Matrix Acidizing" by M. Ali and H. Nasr-El-Din, 2019. SPE-191136-PA, Copyright 2019 by Society of Petroleum Engineers.
.

while **Figure 3** shows the cores after acidizing for the experiments conducted using 15 wt% HCl

acid at 150^0F.
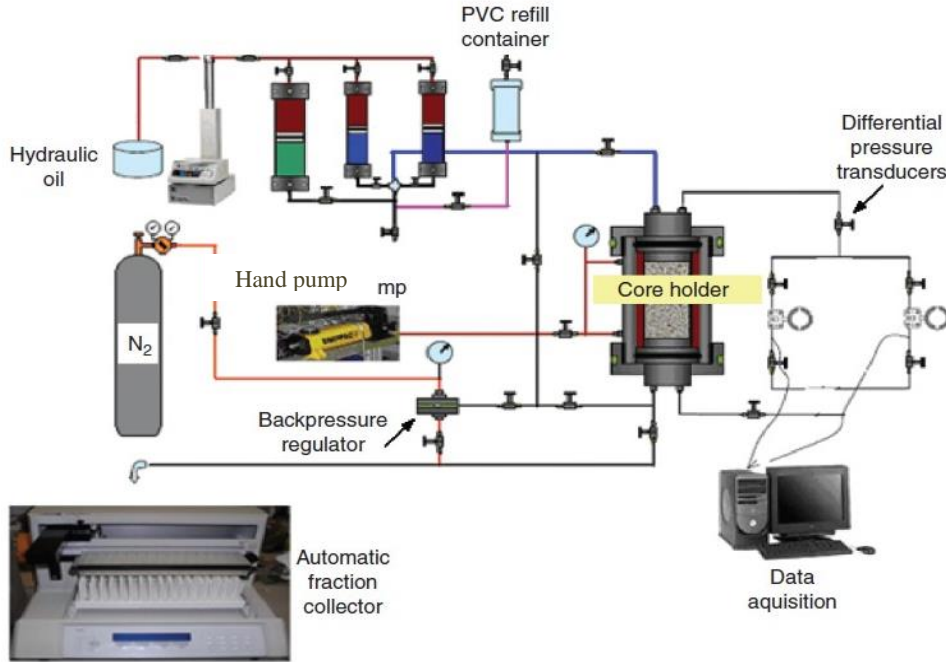
Figure 2 Core flood setup.

Table 1 Properties of dolomite cores and coreflood results. 15 wt% HCl at 150^0F.

Core ID	Injection rate, cm^3/min	PV, cm^3	Initial total porosity, vol%	Initial Vugs Volume/PV, %*	Initial permeability, md	PVBT
1008	1	25.91	14.91	40	65	4.65
1001	3	28.11	16.18	26	80	4.20
1007	5	23.18	13.34	48	50	3.30
1003	7	29.66	17.07	15	50	3.70
1010	10	26.41	15.20	21	65	4.85

* Calculated from CT scan data, voxels with porosities higher than 35 vol% are considered vugs.

Table 2 Properties of dolomite cores and coreflood results. 20 wt% HCl at 200°F.

Core ID	Injection rate, cm^3/min	PV, cm^3	Initial total porosity, vol%	Initial permeability, md	PVBT
1201	1	26.23	15.25	62	2.82
1203	3	28.12	16.35	80	1.84
1204	5	23.35	13.57	40	1.65
1202	7	24.36	14.16	47	1.88
1206	10	27.72	16.12	76	2.09
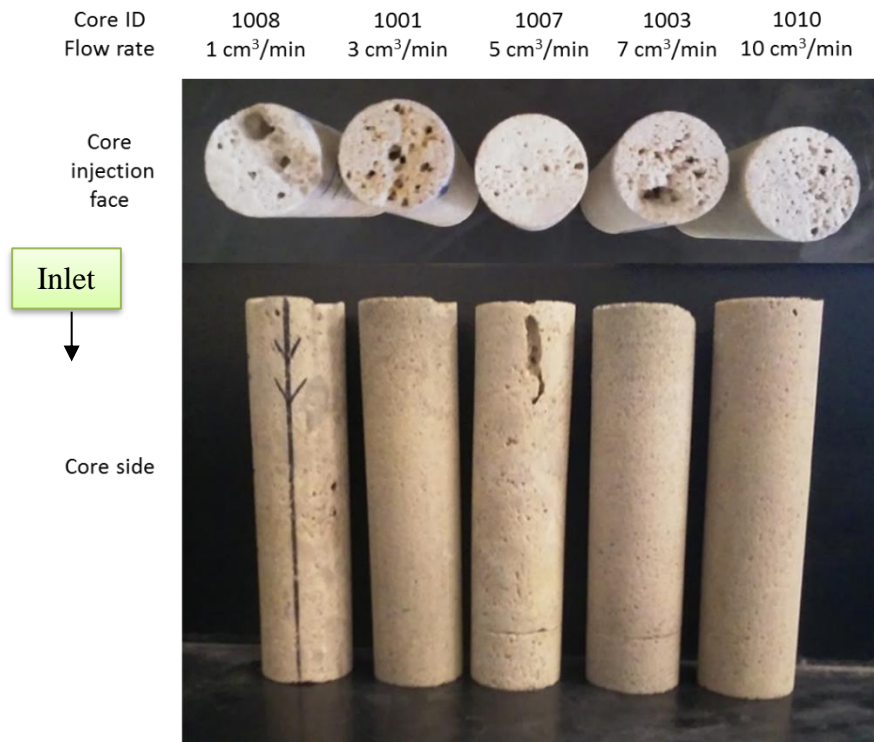
Figure 3 Dolomite cores after injection of 15 wt% HCl at 150°F.

16

4.2. Vugs Characterization using X-ray CT Scanning

The vugs present in the cores were determined qualitatively from the CT images, as shown in **Figure 4**. CT numbers are indicators of material density where the negative numbers indicate low-density material (air) and high positive numbers indicate high-density material (solid). Accordingly, in Figure 4, the blue color (negative CT number) indicates vugs, the red color (high positive CT number) indicates solid or matrix with very low porosity and white color indicates moderate to high porosity matrix. After identifying the vugs of the cores qualitatively, they were quantified following Izgec et al. (2010). In their work, they divided the porosity voxels generated from the CT scan into matrix for low range porosity, mud filled vugs for average porosity and clean vugs for very high porosity values. In the current study, the cores did not contain mud. Therefore, the porosities were divided into matrix and vugs based on a 35 vol% porosity cut-off. The well-packed balls into a box give 45 vol% porosity; accordingly, 35 vol% porosity is a reasonable cut-off. The vugs as a fraction of the total pore volume are given in Table 1. The next section discusses the porosity generation from CT images.
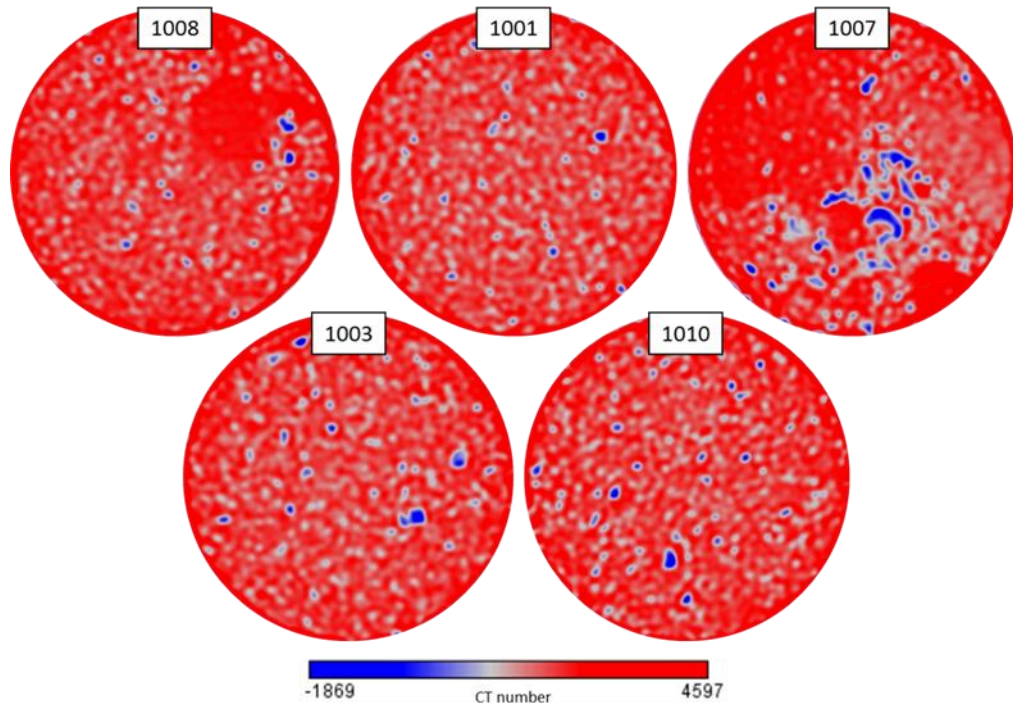
Figure 4 CT scan images (1.5 in. diameter) for the studied dolomite cores. Blue color (negative CT number) indicates vugs/void spaces, red color (high positive CT number) indicates solid/ low porosity and white color indicates medium to large porosity. Numbers inside the boxes are the cores ID's.

5. EFFECT OF POROSITY DISTRIBUTION ON ACID PROPAGATION IN CARBONATES[4]

5.1. Generating Porosity Distribution

An important step in building an acidizing simulation model is the initial porosity distribution. Panga et al. (2002, 2005) and Maheshwari et al. (2012, 2016) used a uniform distribution for porosity. Liu et al. (2012) showed that normal distribution provides better simulation results against Tardy's (2007) experimental data. Later, Liu et al. (2016) concluded that models with porosity distributed using spatially correlated techniques yields more realistic simulation results. Porosity distribution was built from CT scans by Ghommem et al. (2015).

In the present study, dry and wet CT scans were translated into porosity distribution. The core was marked, as shown in **Figure 3** (the black line along core 1008), to ensure that the scan starts from the same point, and more importantly, that dry and wet images coincide with each other. Finally, porosity is generated using **Equation 14**. (Akin and Kovscek 2003):

$$\varepsilon = \frac{CT_{wet} - CT_{dry}}{CT_{water} - CT_{air}} \quad \ldots\ldots\ldots\ldots\ldots\ldots\ldots\ldots\ldots\ldots\ldots\ldots\ldots\ldots\ldots\ldots\ldots\ldots\ldots\ldots \textbf{Equation 14}$$

The porosity distribution is assessed by comparing high porosity voxels with negative CT values, as shown in **Figure 5**. Then, the porosity values from CT scan were adjusted, so the average matches the weight difference porosity value. It is worth noting that the erroneous high porosity voxels around the edges shown in Fig. 5 were removed before comparing CT scan porosity average with the experimental average.

---

4 Partially reprinted with permission from "A Robust Model to Simulate Dolomite-Matrix Acidizing" by M. Ali and H. Nasr-El-Din, 2019. SPE-191136-PA, Copyright 2019 by Society of Petroleum Engineers.

Figure 5 CT scan slices from the dry (left) and wet (middle) cores. Porosity distribution (right), high porosity voxels are indicated in white. Red circles show the good match between the original CT scans and calculated porosity.

5.2. Predicting Acid Performance Using Porosity Distribution

Bize and Ziauddin (2007) studied the effect of pore structure on acid performance. Zakaria et al. (2015) conducted a detailed study of 6 different types of limestone and generated a master curve based on the flowing fraction; which is defined as the volume injected that corresponds to the normalized tracer concentration at $\frac{c}{c_0} = 0.5$. In the following, we are investigating the use of porosity distribution from the CT scanner as a non-destructive tool to predict acid performance.

   Figure 6 shows the 3D images of the dry CT scan of 6 limestones and one dolomite cores. The images were created using ImageJ software. The vugs are shown in white. The number of vugs changes significantly between rock types. Indiana Limestone and Austin chalk have almost no vugs and the number of vugs increases from Pink desert to Edwards yellow to Winterset. Edwards white contains highly connected vugs. The CT scan of the Silurian Dolomite shows many vugs as well.

(a) Indiana Limestone (b) Austin Chalk (c) Pink Desert (d) Edwards Yellow

(e) Winterset (f) Edwards White (g) Silurian Dolomite
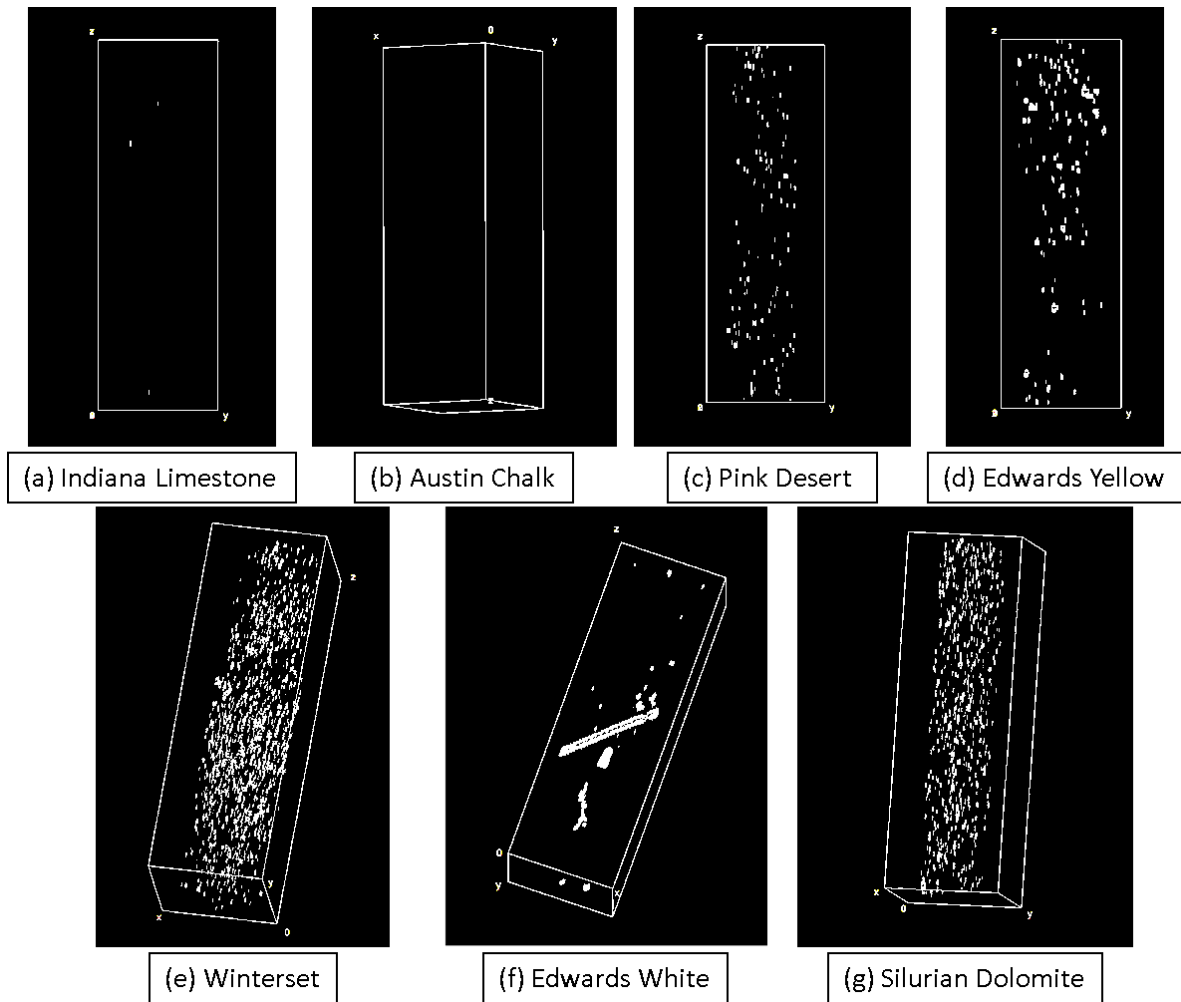
Figure 6 3D images of the dry CT scan of seven carbonate rocks: (a) Indiana limestone, (b) Austin chalk, (c) Pink desert, (d) Edwards yellow, (e) Winterset, (f) Edwards white, and (g) Silurian dolomite. White color indicates vugs.

Figure 7 presents the porosity histograms of 7 rock types. The porosity was created by subtracting the wet and dry CT images (Ali and Nasr-El-Din 2019). The porosity histograms shown in Figure 7 were generated using ImageJ software. The shape of the histogram and the standard deviation agree well with the CT scan 3D images shown in Figure 6. Indiana limestone and Austin chalk have the lowest standard deviation values of 0.09 and 0.11, respectively. As the

21

number of vugs increases in Pink desert, Edwards yellow, and Winterset, the standard deviation values increased to 0.178, 0.17, and 0.25, respectively. The Edwards white didn't show a high value of standard deviation because the total volume of vugs is relatively small. The large number of vugs in Silurian dolomite agrees well with the high standard deviation of 0.19.

Zakaria et al. (2015) conducted tracer experiments on 6 limestone rock types to find the flowing fraction for each rock type. In the current paper, the flowing fraction was measured for Silurian dolomite cores and it was found to be 0.89 (**Figure 8**). A comparison between the flowing fraction and the porosity standard deviation for the 7 rock types is shown in **Figure 9**. There is an inverse relationship between the flowing fraction and the standard deviation of porosity for all the rock types studied except for Edwards White limestone. Although the high connectivity in the vugs system of Edwards white affects the flowing fraction, it doesn't result in high standard deviation in porosity.

The effect of the porosity distribution on the TSC model performance will be discussed in the next chapter.
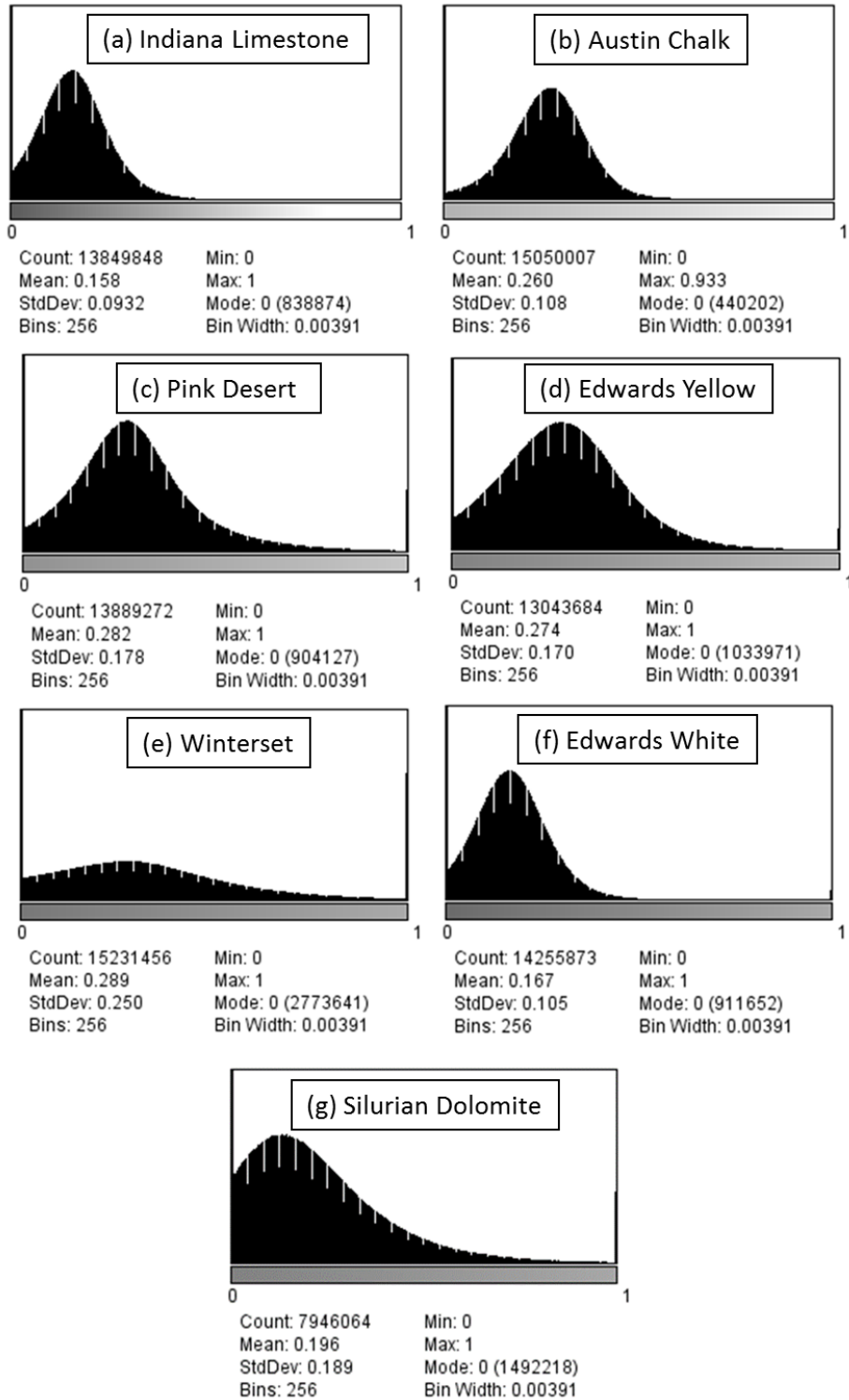
Figure 7 Porosity histogram of 7 carbonate rocks: (a) Indiana limestone, (b) Austin chalk, (c) Pink desert, (d) Edwards yellow, (e) Winterset, (f) Edwards white, and (g) Silurian dolomite.
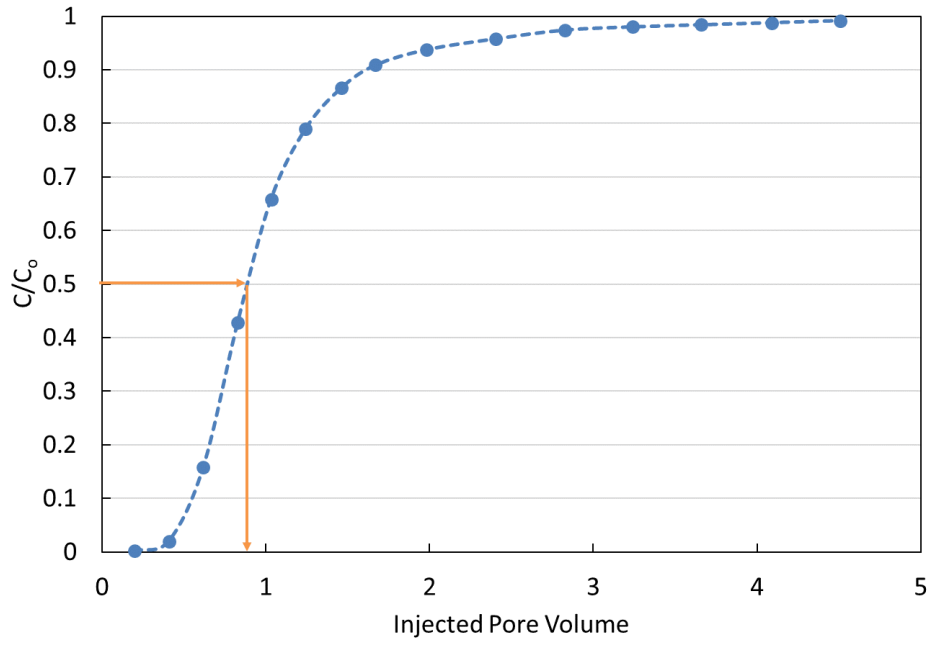
Figure 8 Tracer Profile for Silurian Dolomite Core.
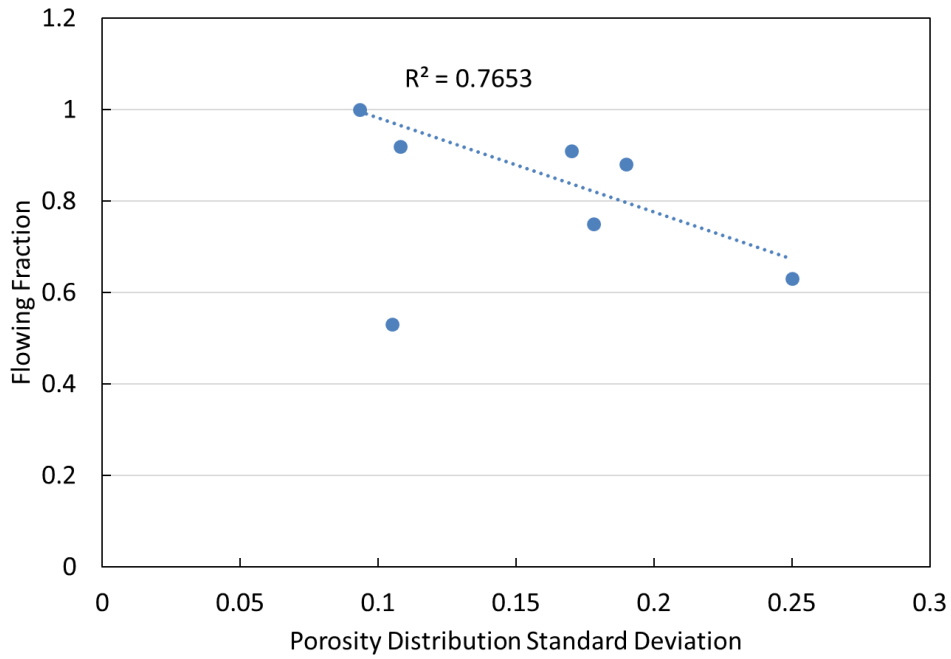
Figure 9 Correlation Between Flowing Fraction and Porosity Distribution Standard Deviation of the Seven Rock Types Presented in This Study.

6. SIMULATING LINEAR ACIDIZING EXPERIMENTS [5]

6.1. Introduction.

Simulating acidizing experiments using a rectangular cube domain (Maheshwari and Balakotaiah 2013; Ghommem et al. 2015; Maheshwari et al. 2016; Schwalbert et al. 2017) facilitates the task of building a high-quality mesh avoiding many of the convergence problems, but the real cylindrical shape of the core is ignored. Matching of the wormhole propagation and branching using rectangular cube domain is impossible, especially when the wormhole propagates near the core edges. De Olivera et al. (2012), Safari et al. (2016), and Akanni et al. (2017) built cylindrical domains for their simulations. Although it matches the real shape, building a high-quality mesh for that domain is a time consuming and tedious process. In the current work, a rectangular cube domain was built with the cylindrical core inscribed inside to model the real shape of the core without losing solution accuracy (**Figure 10**). In the model, the part out of the cylindrical core is given a very low porosity (< 0.3 vol%) to act as a no-flow boundary; porosity was not set to zero to avoid solution divergence errors in the simulation model. The current model dimensions are 1.5 in. x 1.5 in. x 6 in., and it contains 495,000 of equal sized cells.

Maheshwari and Balakotaiah (2013), Ghommem et al. (2015), Maheshwari et al. (2016), and Schwalbert et al. (2017) modeled the acidizing experiments by modifying the exponents in the Carman-Kozeny correlation. Safari et al. (2016) did not mention changing any parameters in their matching process of a dolomite core face dissolution. The β parameter in Carman-Kozeny correlation (Eq. 9) was determined experimentally for carbonates by McCune et al. (1979) using

a 1.5 in. diameter x 0.25 in. thickness disk, and more recently by Rötting et al. (2015) using a 25

mm diameter x 12 mm thickness disk and was found to be as high as 242 in some cases. Here,

we question using high numbers in simulations for matching the carbonate acidizing

experiments, because in simulation, the Carman-Kozeny correlation is applied at the pore scale.

As an example, Maheshwari and Balakotaiah (2013) applied Carman-Kozeny correlation on cells

with volumes of nearly $1.7e^{-4}$ cm^3 in comparison with Rötting et al. (2015) work, which has a

volume of approximately 59 cm^3.
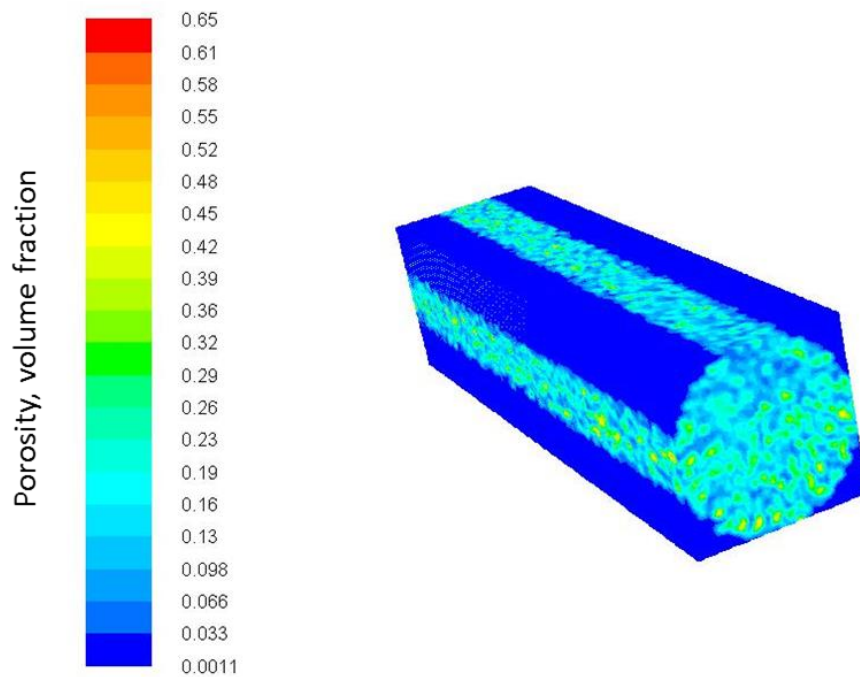
Figure 10 Simulation domain, showing the cylindrical core inscribed inside a rectangular cube domain.

6.2. Dolomite Experiments Using 15 wt% HCl at 150⁰F.

In the current work, Carman-Kozeny exponents γ and β were set to unity. Experiments were matched by increasing both the reaction rate and diffusion coefficient. That was supported by the XRF data of two samples (1.5 in. x 1 in.), which gave a Ca/Mg molar ratio larger than one. That confirms the presence of calcite in the studied cores. **Table 3** shows the XRF data, while **Table 4** shows the calculated molar ratio of Ca/Mg for the two samples. Also, the chemical analysis of the effluent of the 3 cm^3/min experiment showed a molar ratio of Ca/Mg greater than unity, as shown in **Figure 11**. The presence of calcite will result in a higher overall reaction rate constant, but it will not have a perceptible effect on the reaction exponent because it is 0.63 for the HCl-calcite system and 0.65 for the HCl-dolomite system at 150⁰F (Lund et al. 1973, 1975). Also, the presence of two competing minerals (dolomite and calcite) will result in an increase in the acid species dispersion. For simplicity, the diffusion coefficient was increased to account for the effect of dispersion.

The reaction exponent value was calculated from Lund et al. (1973), and the 15 wt% HCl solution viscosity at 150ºF was extracted from Nishikata et al. (1981) by extrapolation. Initial mean pore size, initial interfacial area per unit volume, constant in dispersion correlation, constant in axial dispersion correlation, and constant in transverse dispersion correlation values were considered as given by Maheshwari and Balakotaiah (2013). The list of the simulation parameters used for matching dolomite cores acidizing is given in **Table 5**.

Table 3 Elemental analysis of two dolomite cores using the XRF technique.

	Concentration, wt%	
Element	Sample #1	Sample#2
Ca	45.9	44.2
O	32.5	33.2
Mg	18.1	19.3
Fe	0.8	0.4
Si	0.7	0.3
Cl	0.7	0.3
S	0.5	1.3
K	0.4	0.7
Al	0.4	0.2

Table 4 Calcium/Magnesium molar ratio in dolomite cores used in the present study.

		Moles	Molar Ratio of Ca/Mg
Sample #1	Ca	1.15	1.54
	Mg	0.74	
Sample #2	Ca	1.10	1.39
	Mg	0.79	

Unlike previous studies, the PVBT, along with the 3D wormhole shape, are considered in the matching process because considering the wormhole propagation path in the tuning process will increase the model accuracy and reliability. This allows models to be tuned with a low number of experiments, and then be used with confidence in predicting additional experiments.
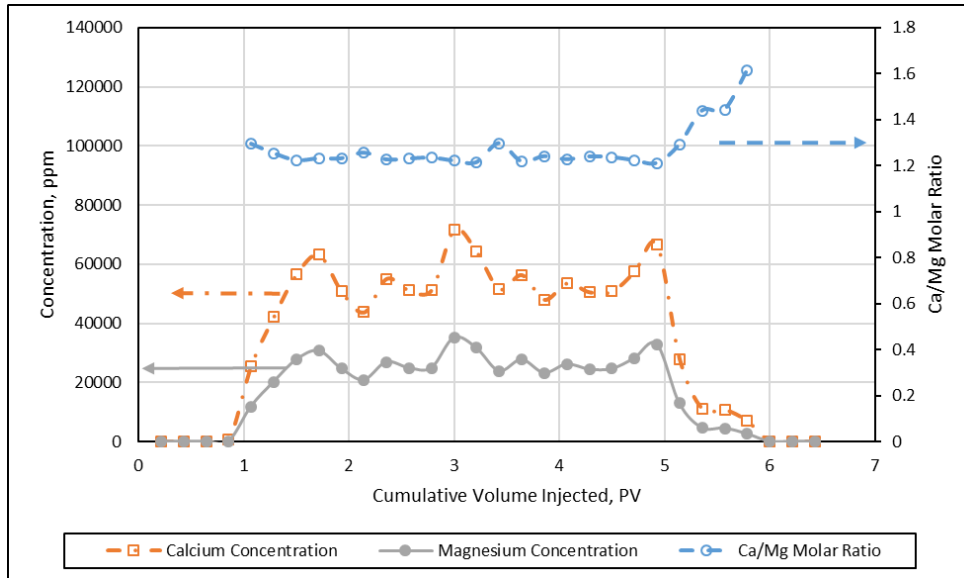
Figure 11 Dissolved calcium ion and magnesium ion concentrations and calcium/magnesium molar ratio for the 3 cm3/min experiment as a function of cumulative volume injected. 15 wt% HCl at 150ºF.

For the following simulations, the PVBT is defined as a two order of magnitude pressure drop reduction over the core. The simulation time step was varying between 0.06 to 0.5 seconds, and the wall-clock runtime was in the range of 24 to 72 hours using 8 processing cores at TAMU high performance research computing clusters. **Figure 12** presents a comparison between the experimental and simulation PVBT. A good agreement with experimental results is obtained, as shown in Fig. 8. The absolute percentage error varies between 3% for the 5 cm^3/min rate experiment and 8% for the 7 cm^3/min rate experiment, with an average percentage error of 3.8% for the five experiments.

Table 5 List of the simulation parameters used in the present study. 15 wt% HCl at 150ºF.

Parameter	Value	Source
Length	6 in.	Measured
Initial average porosity (ε)	13.3-17.1 vol%	Measured
Initial average permeability (k)	50-80 md	Measured
Initial mean pore size (r_{p_O})	1 μm	Maheshwari and Balakotaiah (2013)
Initial interfacial area per unit volume (a_{v_o})	50 cm^{-1}	Maheshwari and Balakotaiah (2013)
Pore connectivity parameter (γ)	1	Carman (1956)
Pore broadening parameter (β)	1	
Rock density (ρ_s)	2.77 g/cm^3	Measured
Surface reaction rate constant (k_s)	5×10^{-3} $mole^{1-n}/(cm^{2-3n}.s)$	Matching parameter
Surface reaction exponent (n)	0.65	Lund et al. (1973)
Acid diffusion coefficient (D_m)	5×10^{-4} cm^2/s	Matching parameter
15 wt% HCl viscosity (μ)	0.65 cp	Nishikata et al. (1981)
Constant in dispersion correlation (α_{os})	0.5	Maheshwari and Balakotaiah (2013)
Constant in axial dispersion correlation (λ_x)	0.5	Maheshwari and Balakotaiah (2013)
Constant in transverse dispersion correlation (λ_l)	0.1	Maheshwari and Balakotaiah (2013)
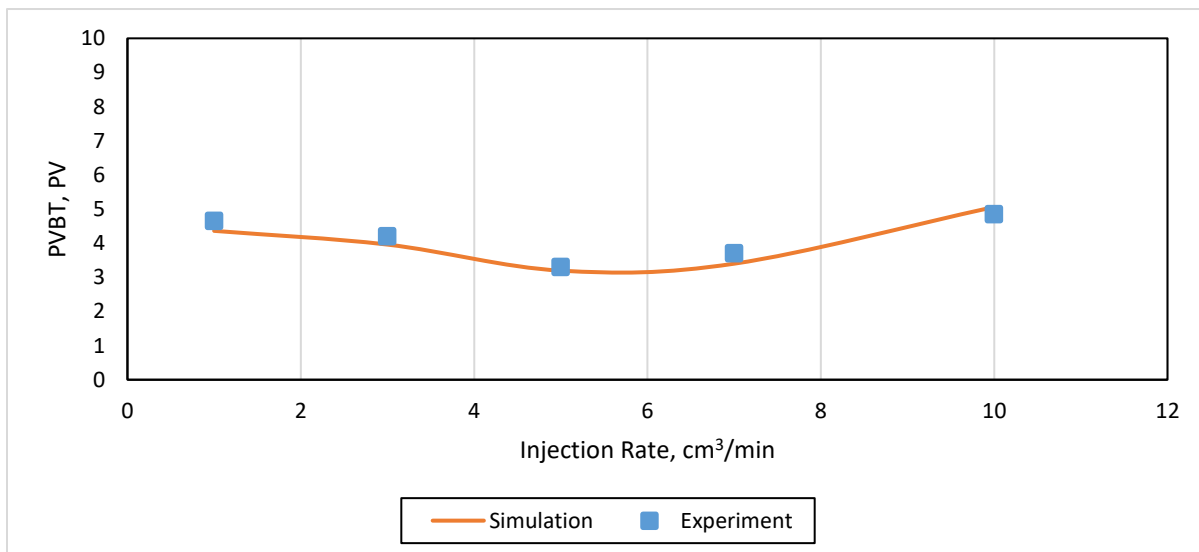
Figure 12 Acid efficiency curve. A comparison between simulation and experimental results using 15 wt% HCl at 150ºF.

Figure 13 shows the simulated dissolution pattern along with the after acidizing CT scan for the 1 cm^3/min experiment. The match is considered moderate because the simulation shows the same dissolution pattern and wormhole path for more than half of the core, but a reduction in the pressure drop of 100 times is observed before actual acid breakthrough. The reason is the small tilting of the wet core during the CT scan operation as shown in **Figure 14**. Because the two scan images did not coincide with each other, the error in the calculated porosity increases and does not reflect the actual porosity distribution. It is concluded that even a small tilting in the core during the CT scan could have an immense effect on the wormhole dissolution pattern. It is also recommended to run the dry core CT scan, then saturate the core under the CT scanner (in place), and finally run the wet core CT scan to ensure the coincidence of the two images. This simulation run shows the importance of including the spatial wormhole propagation in assessing the match quality. Because in the current simulation, although the match was very good for the PVBT, no actual breakthrough was observed in the simulation.

Figure 15 shows the simulated dissolution pattern, along with the after acidizing CT scan for the 3 cm^3/min experiment. The match is considered well to excellent because the model was able to capture the correct wormhole path and the branching near the middle of the core. Also, the curvature in the wormhole near the core outlet was well captured.
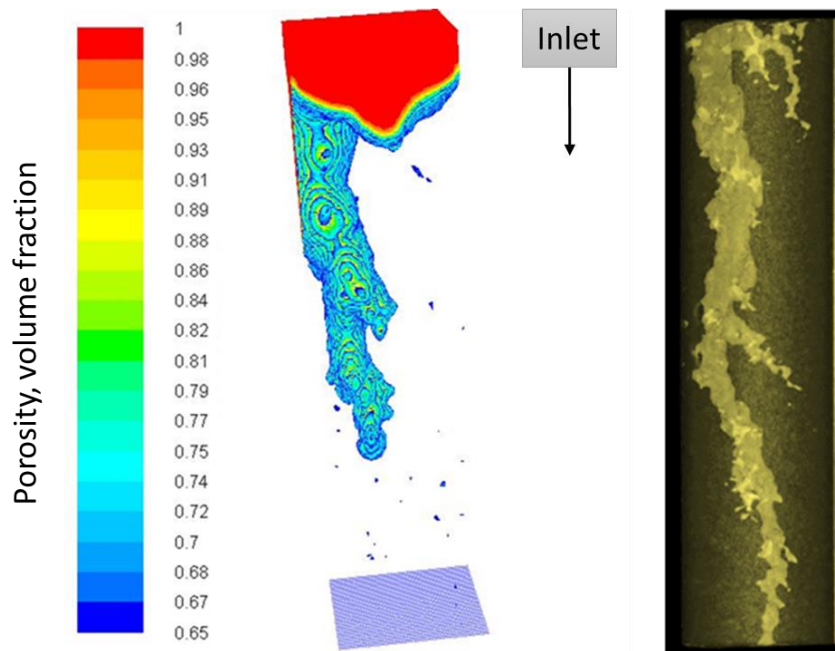
Figure 13 Dissolution pattern. A comparison between simulation (right) and CT scan (left) for the 1 cm3/min experiment. 15 wt% HCl at 150⁰F.
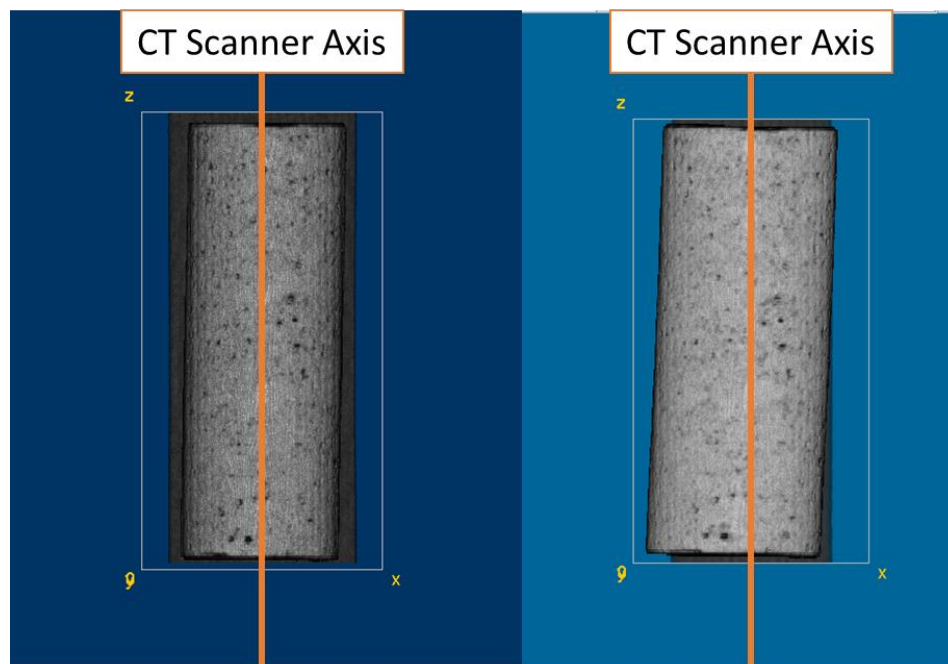
Figure 14 CT scan 3D view. A position comparison between the dry core (left) and wet core (right).
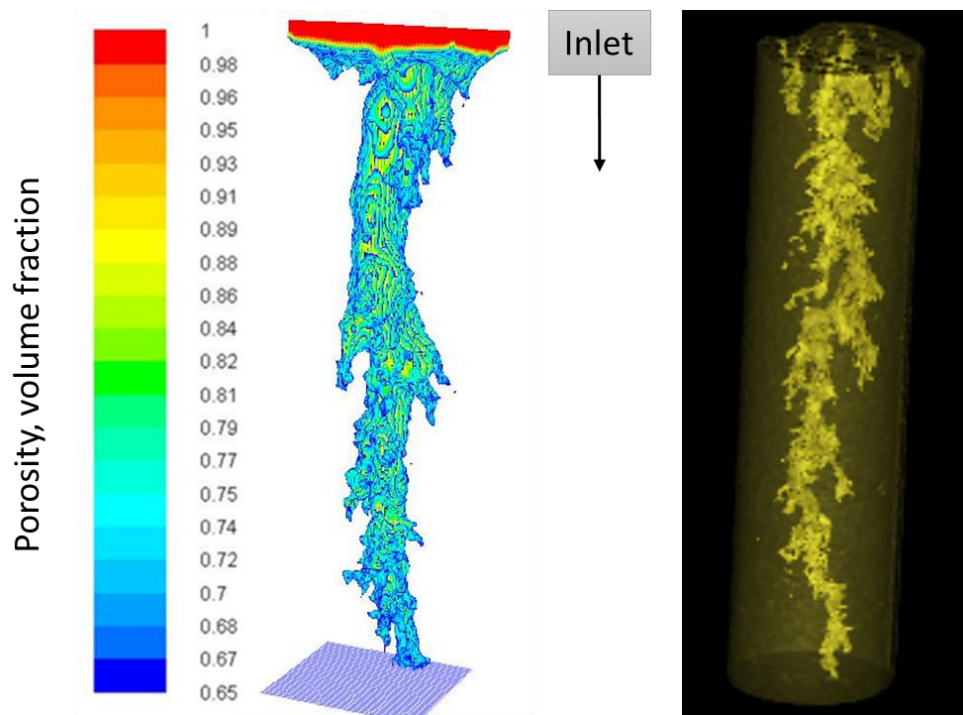
Figure 15 Dissolution pattern. A comparison between simulation (right) and CT scan (left) for the 3 cm3/min experiment. 15 wt% HCl at 150⁰F.

Figure 16 shows the simulated dissolution pattern, along with the after acidizing CT

scan, for the 5 cm^3/min experiment. The match is considered well to excellent because the highly

tortuous path of the wormhole was accurately captured by the model. The real core image

(**Figure 3**, core 1007) showed a dissolution on the edge of the core close to the inlet, which was

captured by the model. That emphasizes the importance of considering the real cylindrical shape

of the core in simulation models. The abrupt change in the wormhole path is attributed to the

high concentration of vugs in that region, as shown in **Figure 17**.
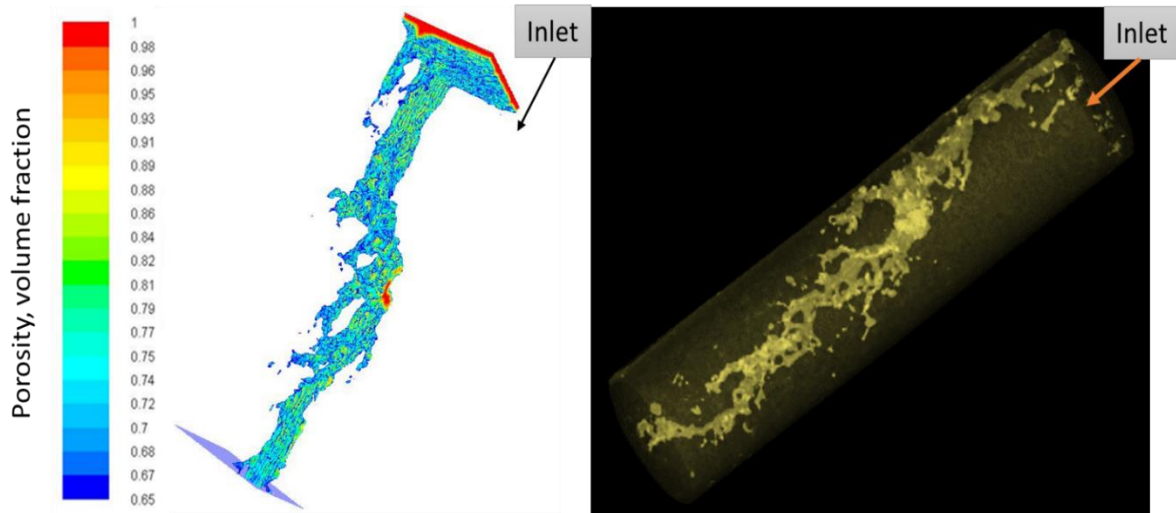
Figure 16 Dissolution pattern. A comparison between simulation (right) and CT scan (left) for the 5 cm³/min experiment. 15 wt% HCl at 150ºF.
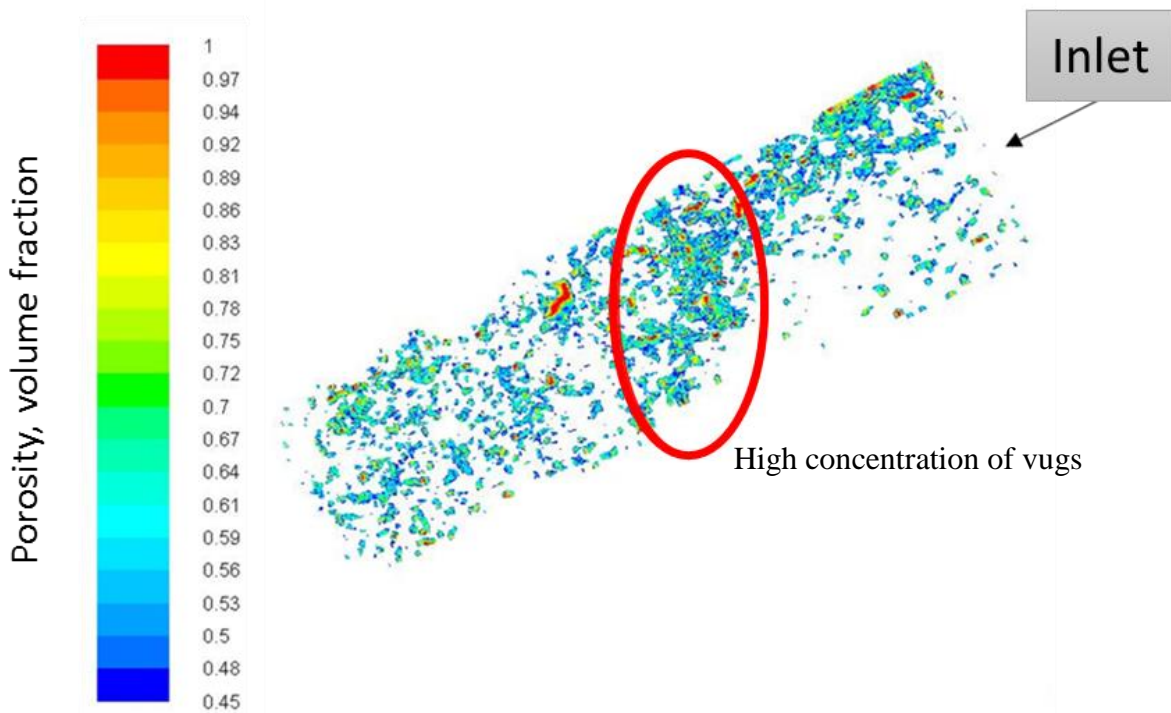
Figure 17 Initial porosity distribution (porosity > 0.45 is shown). The red circle indicates the high concentration of vugs region.

Figure 18 shows the simulated dissolution pattern, along with the after acidizing CT scan, for the 7 cm^3/min experiment. The match is considered well to excellent because the path of the wormhole was captured by the model. There was a delay in the model at the beginning in capturing the wormhole curvature, and a delay in the branching was noticed near the outlet. However, the wormhole was initiated near the core edge, and the presence of two competing wormholes at the beginning was well captured. The model was also able to capture the wormhole thinning and breakthrough near the middle of the core.
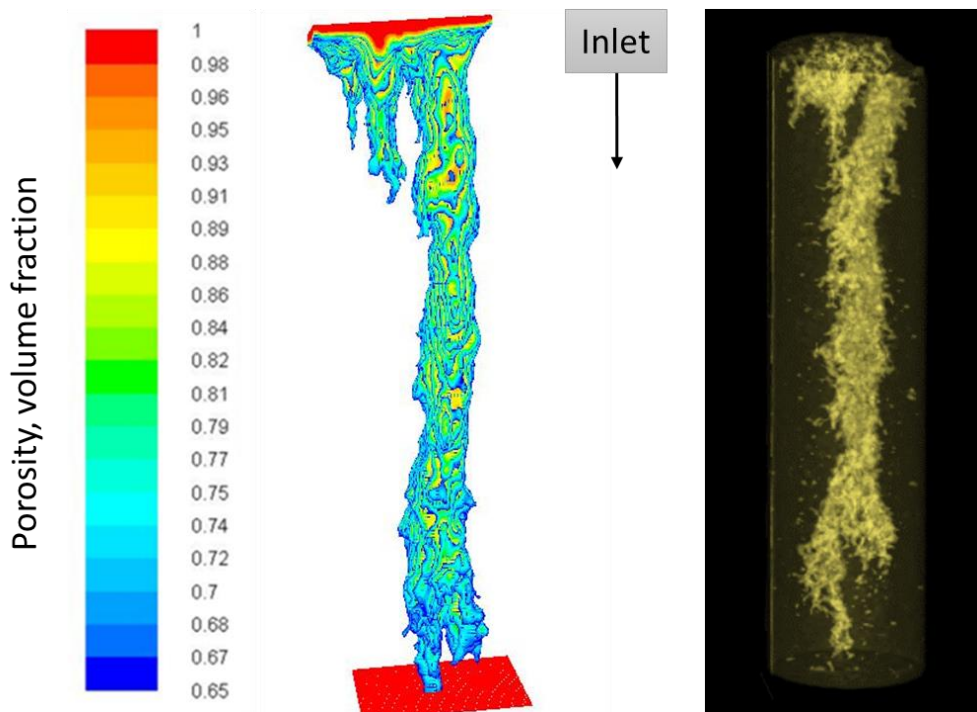
Figure 18 Dissolution pattern. A comparison between simulation (right) and CT scan (left) for the 7 cm3/min experiment. 15 wt% HCl at 150ºF.

Figure 19 shows the simulated dissolution pattern along, with the after acidizing CT

scan, for the 10 cm^3/min experiment. The match is considered good because the curvy path of the

wormhole was captured by the model. The model captures the curvature in the wormhole path,

but the actual wormhole path was curvier.
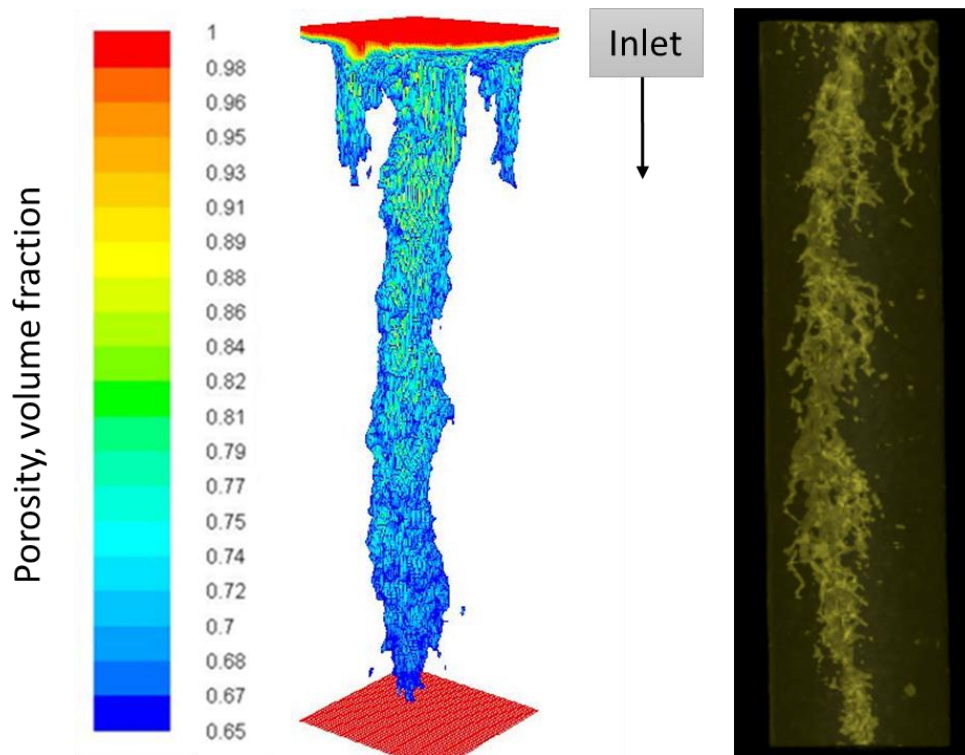
Figure 19 Dissolution pattern. A comparison between simulation (right) and CT scan (left) for the 10 cm3/min experiment. 15 wt% HCl at 150ºF.

The matching process included four experiments, while the fifth experiment (10 cm^3/min)

was used to validate the prediction capabilities of the tuned model. It was realized from the

matching runs performed for the first set of experiments that the model parameters can be

adjusted using as low as three experiments. The three experiments account for the mass transfer

controlled regime (the lowest injection rate), kinetically controlled regime (the highest injection rate), and the combined effect of mass transfer and reaction kinetics (moderate injection rate).

6.3. Dolomite Experiments Using 20 wt% HCl at 200^0F.

To study the predictability of the model under different acid concentration and temperature, a second set of experiments were conducted at 200^0F using 20 wt% HCl. The increase in acid concentration will result into higher reactivity as the number of H^+ cations in solution increases, while the higher temperature will result in higher reactivity through the increase in both reaction kinetics (constant and exponent) and acid diffusion coefficient. In the model, the acid concentration was increased to 20 wt% while the reaction exponent was increased to 0.8 to account for both the increase in temperature and the presence of Calcite in the dolomitic cores (Lund et al. 1973, 1975). To be consistent with previous simulations, only diffusion coefficient and reaction constant were modified to match the second set of experiments. The rest of the simulation parameters were kept the same as previous section (**Table 5**).

Unlike the previous section simulations where we built a porosity distribution for every single experiment, the second set of experiments was matched using one porosity distribution, namely, core 1010 porosity distribution. The properties of core 1010 are close to the average of the five cores used in the second set of experiments (Table 2). Using one porosity distribution for matching the five experiments was encouraged by the fact that under field conditions, it is impossible to have a detailed porosity distribution similar to the one provided by CT scanner. Only three experiments were used to match the model, the lowest rate (1 cm^3/min), the highest rate (10 cm^3/min), and a moderate rate (5 cm^3/min), validating our proposed approach from the first set of experiments. To match the three experiments, the diffusion coefficient was set to 3 X

37

10^{-3} cm^2/s and the reaction rate constant was an order of magnitude higher than the value presented in Table 5. The high values of the matching parameters can be attributed to the presence of pure calcite in the cores as discussed in the previous sections and proved experimentally from the effluent samples as shown in **Fig. 20**. The matching parameters may be a little bit different if the actual porosity distribution of each core was used instead of using one porosity distribution to match the five experiments. But, in the context of validating our matching approach by considering different acid concentrations and temperatures, we believe that using one averaged porosity distribution that considers the actual distribution and pore structure is enough.

Fig. 21 presents a comparison between the experiments and the simulation runs using 20 wt% HCl at 200^{0}F. The absolute percentage error between the experiment and the simulation varies between 16.8% for the 3 cm3/min and 4.2% for the 5 cm3/min. The average percentage error for the five experiments is nearly 2.6%. The results show a good agreement between the experiments and the simulation runs. The 3 cm3/min and the 7 cm3/min experiments were not included in the matching process but they were used to validate the prediction capabilities of the tuned model. The two sets of experiments confirm that a few number of experiments can be used to build a robust model for modeling dolomite matrix acidizing.
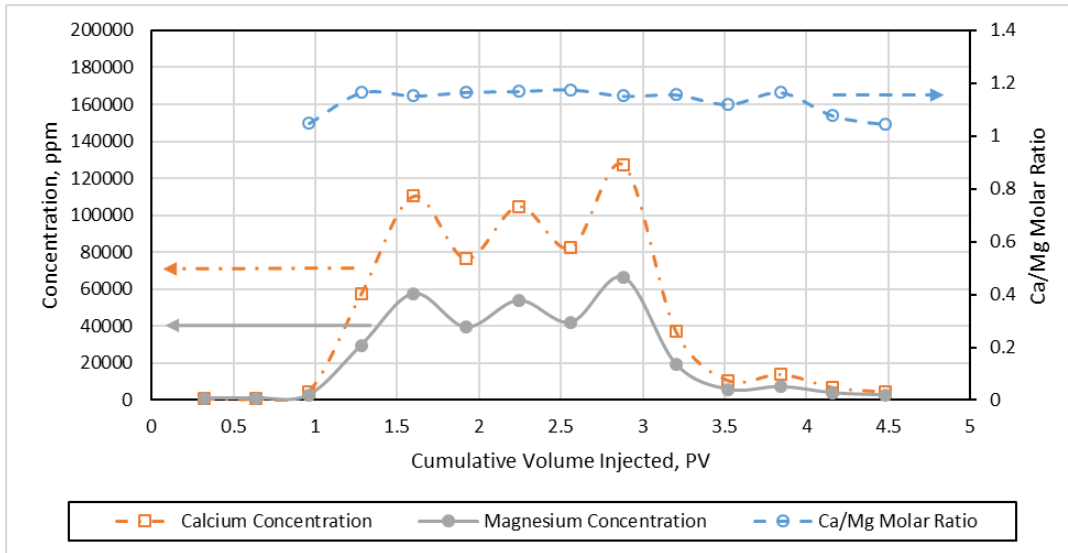
Figure 20 Dissolved calcium ion and magnesium ion concentrations and calcium/magnesium molar ratio for the 3 cm³/min experiment as a function of cumulative volume injected. 20 wt% HCl at 200⁰F.
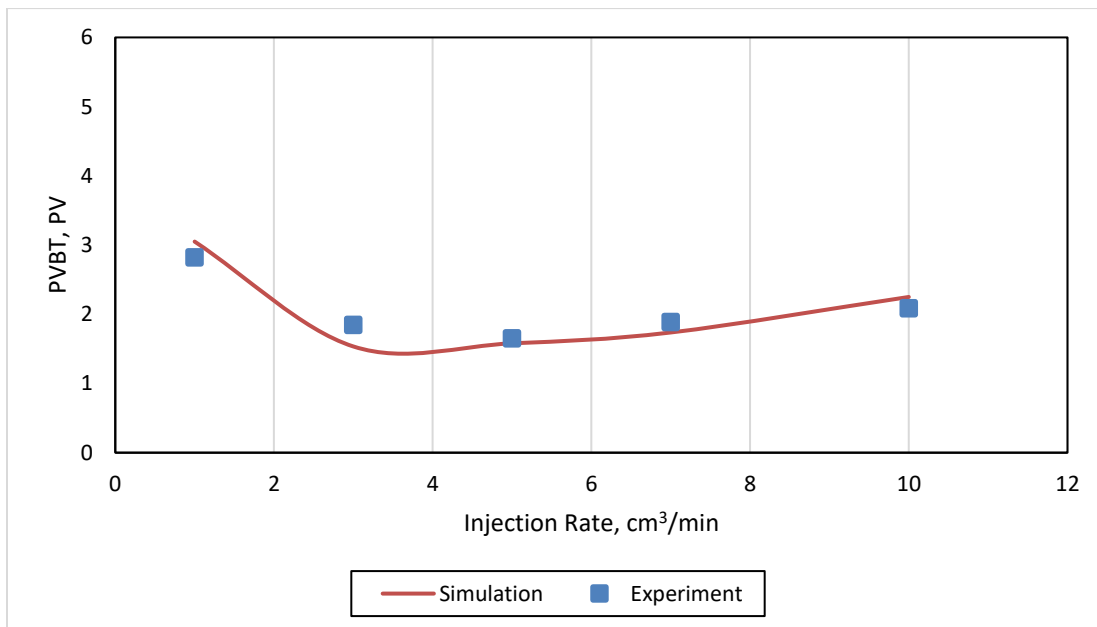
Figure 21 Acid efficiency curve. A comparison between simulation and experimental results using 20 wt% HCl at 200⁰F.

6.4. Limestone Experiments Using 15 wt% HCl at 150^{0}F. (Effect of Rock Type)

It was shown in the previous chapter that the porosity distribution exported from CT scanner change from rock type to another. Hereafter, we are studying the ability of the TSC to predict carbonate rock types based on the initial porosity distribution from the CT scanner.

Fig. 22 presents a comparison between Zakaria et al. (2015) experiments and the TSC model simulations for Indiana Limestone cores acidizing using 15 wt% HCl at 150°F. Similar to the Dolomite cases, the diffusion coefficient and the reaction rate constant were the only tuning parameters. A good match with an absolute average percentage error (AAPE) around 11% was achieved between experiments and simulations.
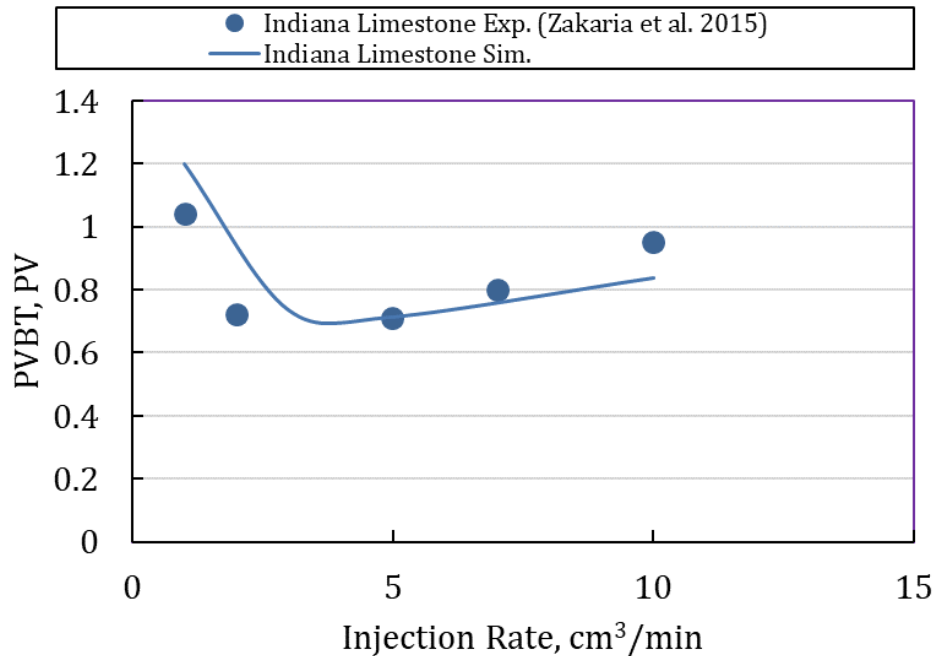
Figure 22: A comparison between Zakaria et al. (2015) Indiana Limestone experiments (symbols) and TSC model simulations (line) using 15 wt% HCl at 150°F.

The effect of the porosity distribution on the TSC model was studied and assessed by simulating Edwards White experiments using the simulation matching parameters of the Indiana limestone experiments. **Fig. 6** shows a comparison between Zakaria et al. (2015) experiments and the TSC model simulations for Edwards White cores acidizing using 15 wt% HCl at 150°F. A moderate match between the experiments and the simulations was achieved. The AAPE was nearly 26%, the decrease in the quality of match for the Edwards White experiments can be attributed to the effect of the pore connectivity on the acid dispersion, which requires further tuning of the simulation model. A more holistic way to assess the capabilities of the TSC model to simulate different rock types using the same parameters is the ratio between Indiana Limestone PVBT to Edwards White PVBT. **Fig. 7** presents the ratio for experiments and TSC model simulations which reveals that at the low and the high rate the TSC model can capture the effect of the rock type, but the percentage error increases near the optimum conditions to reach 29%. For the two sets of experiments, the simulation model can capture the effect of the rock type to up to 15%. The ability of the TSC model to capture the effect of rock types will have a prominent effect on field stimulation treatment designs.
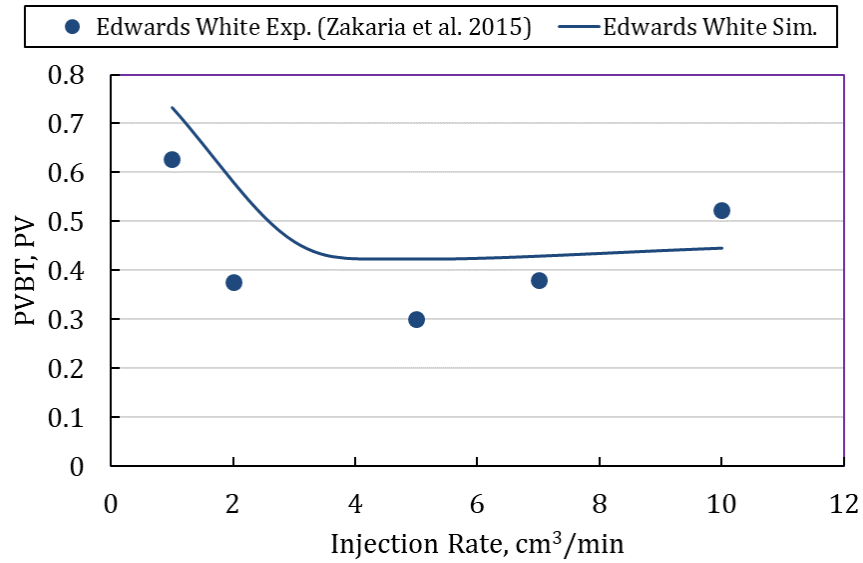
Figure 23 A comparison between Zakaria et al. (2015) Edwards White experiments (dots) and TSC model simulations (line) using 15 wt% HCl at 150°F.
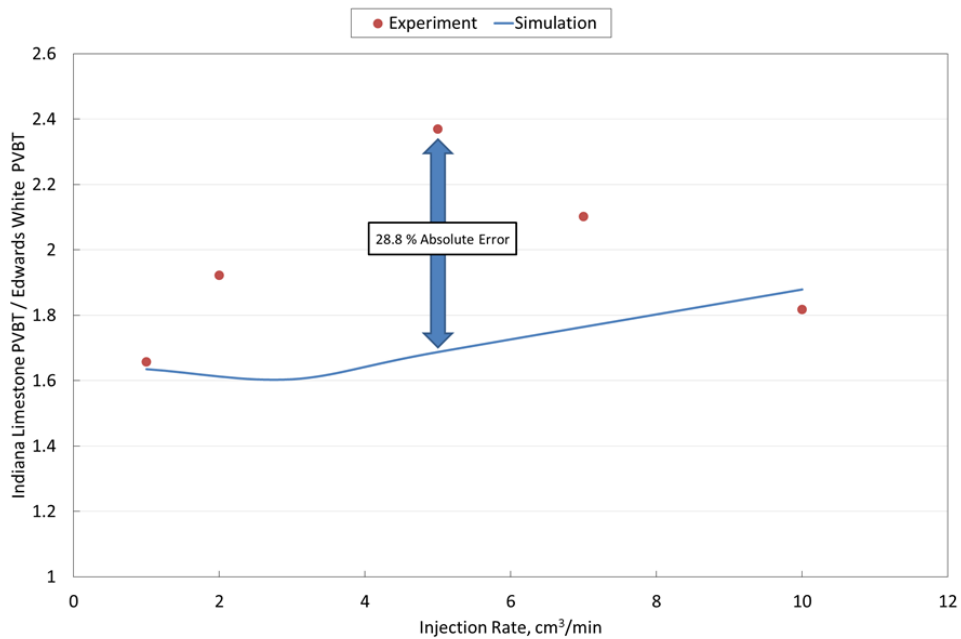
Figure 24 The ratio between Indiana Limestone PVBT to Edwards White PVBT at Different Rates from Zakaria et al. (2015) Experiments and Simulation Data.

7. SIMULATING RADIAL FLOW OF ACID IN HOMOGENEOUS DOLOMITE RESERVOIRS [6]

7.1. Large Scale Radial Experiments

Before using the current model to simulate actual field scale, the tuned model for 15 wt% HCl at 150ºF was utilized to simulate McDuff et al. (2010) results. To the best of our knowledge, McDuff et al. (2010) conducted the largest acidizing experiment on both limestone and dolomite blocks. They drilled a hole inside a 14 ft^3 block to mimic the radial flow geometry in field conditions. In their study, they used smaller blocks of 0.8 ft^3 for dolomite experiments. To simulate McDuff et al. (2010) experiments, a radial model was built with a diameter of 1 ft. and thickness of 1 ft. and wellbore diameter of 0.05 ft. The initial porosity distribution was generated using the distributions generated by CT scanner for the previously studied Dolomite cores; to ensure that porosity distribution is closest to natural distribution (**Figure 25**). The spatial propagation of the wormhole from simulation (**Figure 26**) and McDuff et al. (2010) study (**Figure 27**) are very similar.

---

6 Partially reprinted with permission from "A Robust Model to Simulate Dolomite-Matrix Acidizing" by M. Ali and H. Nasr-El-Din, 2019. SPE-191136-PA, Copyright 2019 by Society of Petroleum Engineers.
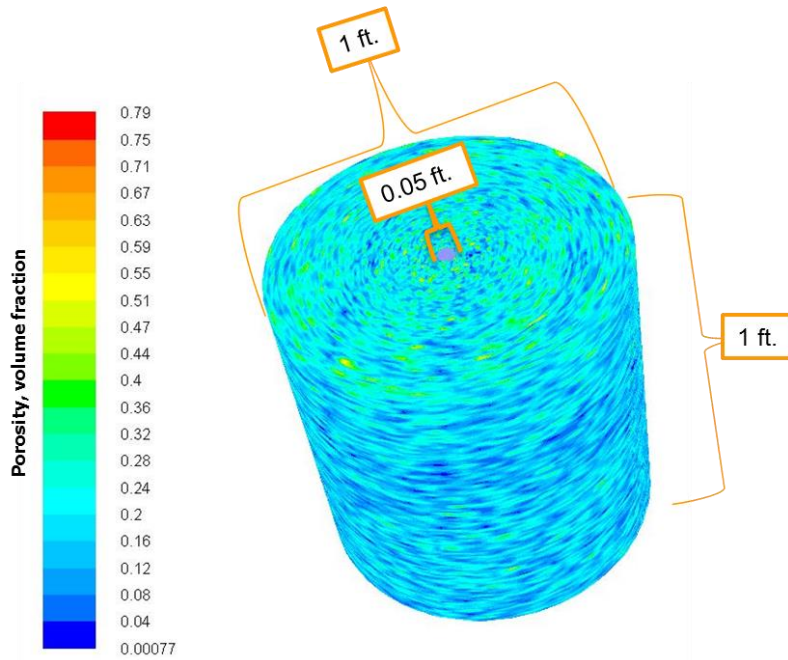
Figure 25 Initial porosity distribution for the 1 ft. diameter radial model.

Figure 26 Top and side views of dissolution pattern from the optimum rate simulation. A is the original wellbore diameter, while B is the after acidizing wellbore diameter. 15 wt% HCl at 150^{0}F.
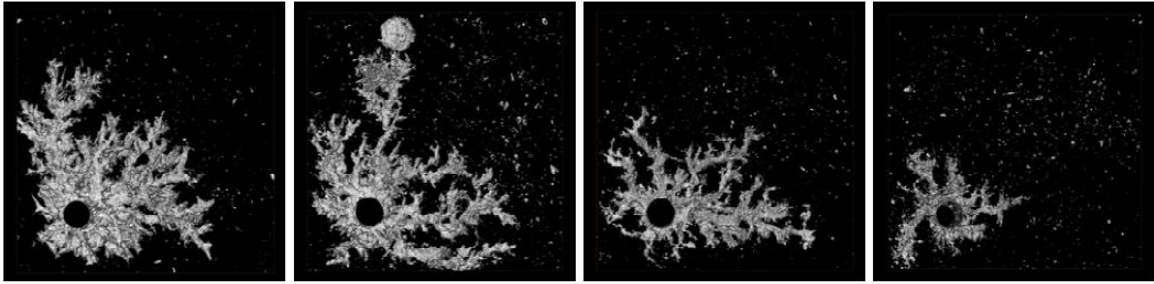
Figure 27 Top views of wormhole structures from Silurian dolomite.

7.2. Field Scale Radial Simulations.

To mimic field conditions, a radial model was built with 1 ft. thickness and borehole of 0.5 ft. diameter. Two domains were built with formation depth of investigations of 0.5 and 1 ft. as shown in **Figure 28**. The porosity distributions were generated as previously discussed using the five cores CT scan data. In the absence of actual porosity distribution from CT scans, it is recommended to distribute the porosity in a spatially correlated manner as proposed by Liu et al. (2016). The tuned model for 15 wt% HCl at 150^0F was used. **Figure 29** shows the acid efficiency curve for the experimental data, radial 1.5 ft. diameter domain, and radial 2.5 ft. diameter domains. The graph depicts that the optimum PVBT and velocity were strictly lowered for the radial flow cases in comparison to the linear core flood. Furui et al. (2012) results show that lower PVBT is expected under radial geometry. The increase of the domain diameter for radial model increases the optimum injection velocity, this result agrees with that from linear core flooding (Duong et al. 2014). The higher optimum injection velocity can be attributed to the fluid losses. Contrarily, the optimum PVBT decreases with the increase of the domain diameter, which is opposite to the trend from linear core flooding. That trend in the radial models can be

explained by the increase in the volume with the diameter (volume α (diameter)^2), which surpasses the effect of the fluid losses.
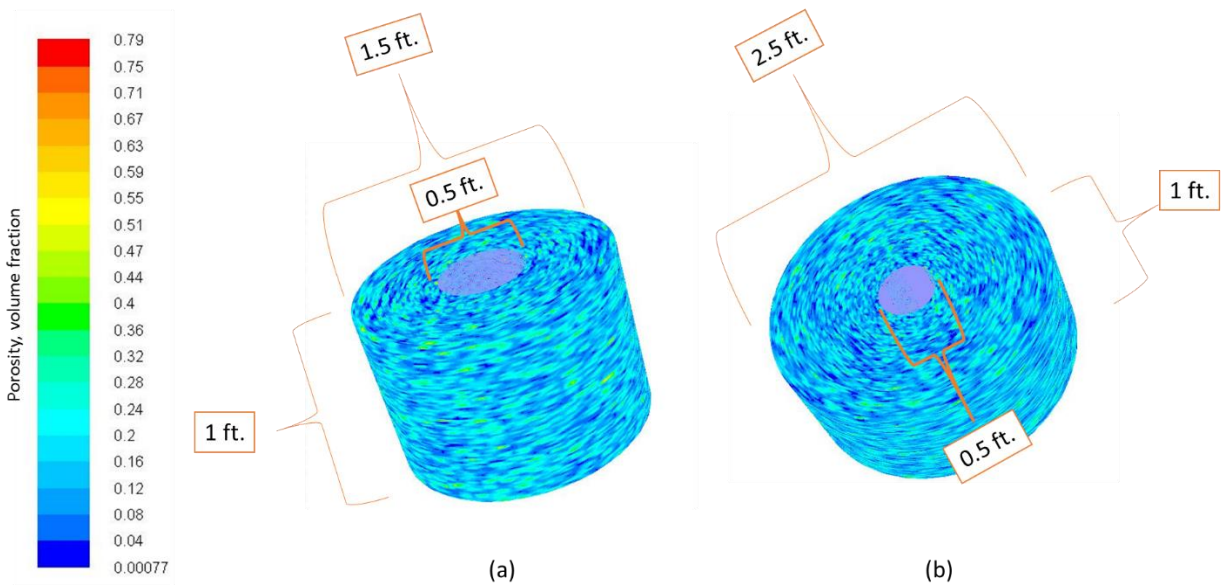
Figure 28 Field scale models initial porosity distribution. (a) 1.5 ft. diameter model and (b) 2.5 ft. diameter.

Figure 29 confirms that the PV of acid required in the field applications is strictly lower than that required for linear core-flood. But, the upscaling of velocity from linear core-flood to field application will remain questionable because as shown in **Figure 28**, the optimum velocity for the radial cases increases with the increase in the acid traveling depth into the formation. Accordingly, it can be lower, equal, or higher than the optimum velocity from linear core-flood. Besides, it is proven by Bazin (2001), Furui et al. (2012), and Duong et al. (2014) that the change

in the optimum velocity will be attributed to changes in the core dimensions (length and diameter).
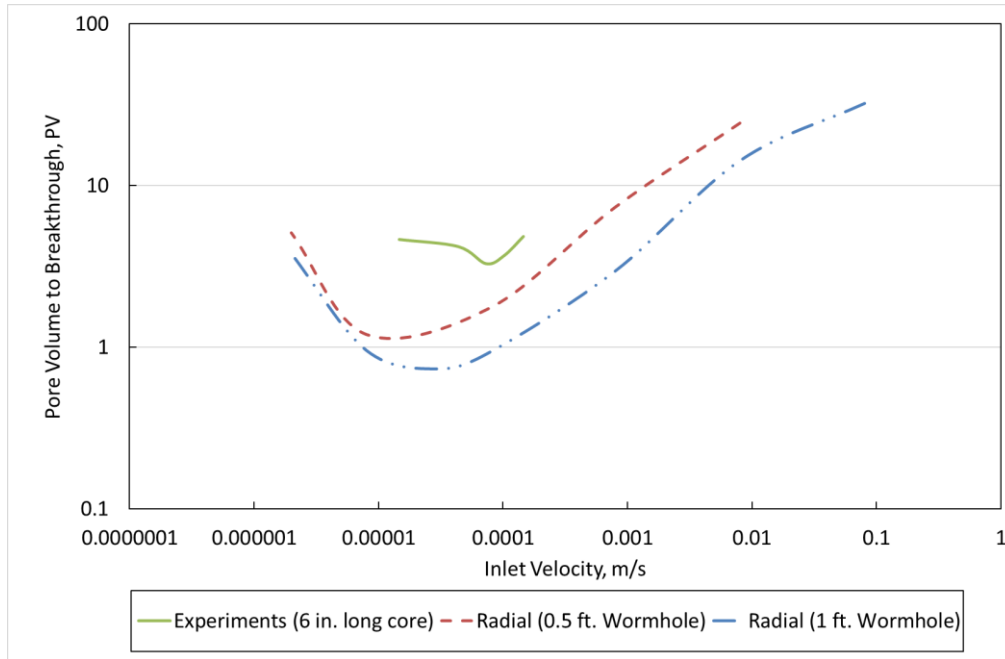
Figure 29 A comparison of acid efficiency curves for linear experiments (green), 1.5 ft. diameter model (maroon), and 2.5 ft. diameter model (blue).15 wt% HCl at 150^{0}F.

To overcome the core dimensions issue, especially when optimum PVBT and injection velocity are to be used into upscaling models (Buijse-Glasbergen 2005; Tardy et al. 2007; Furui et al. 2012), it is proposed to modify those models based on radial simulations as will be shown in next section.

Figures 30 to 32 present the dissolution pattern for the radial 1.5 ft. diameter domain at low, moderate, and high injection rates, respectively. The acidizing process at field scale is

47

accompanied with wellbore enlargement. The degree of the enlargement is high at low injection

rate to low/moderate at moderate and high injection rates. The wellbore enlargement

phenomenon was firstly noticed by McDuff et al. (2010) while conducting the radial large-scale

acidizing experiments.
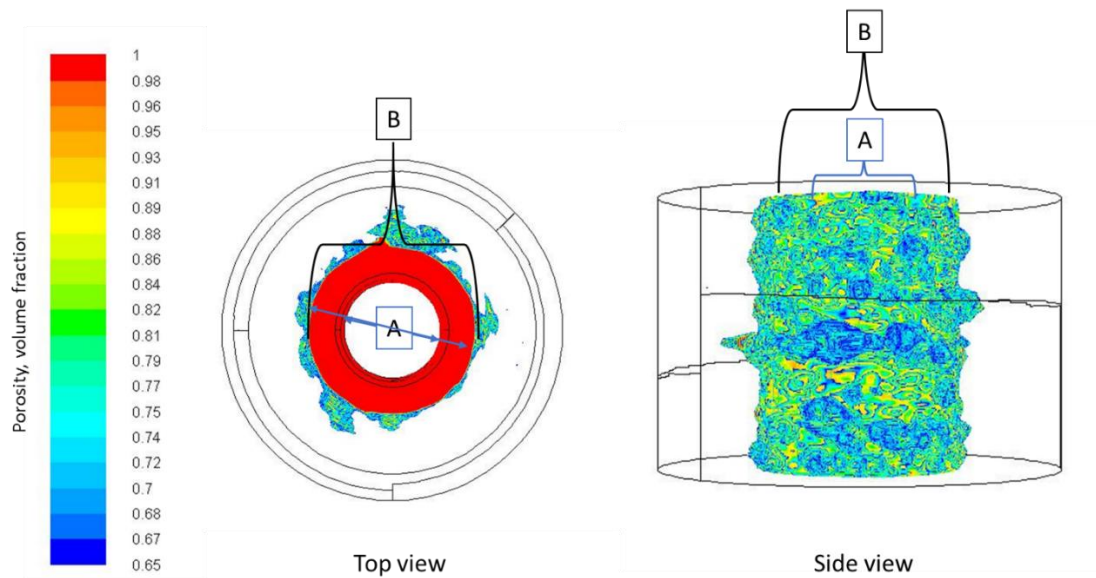
Figure 30 Top and side views of dissolution pattern from the low rate simulation. A is the original wellbore diameter, while B is the after acidizing wellbore diameter. 15 wt% HCl at 150⁰F.
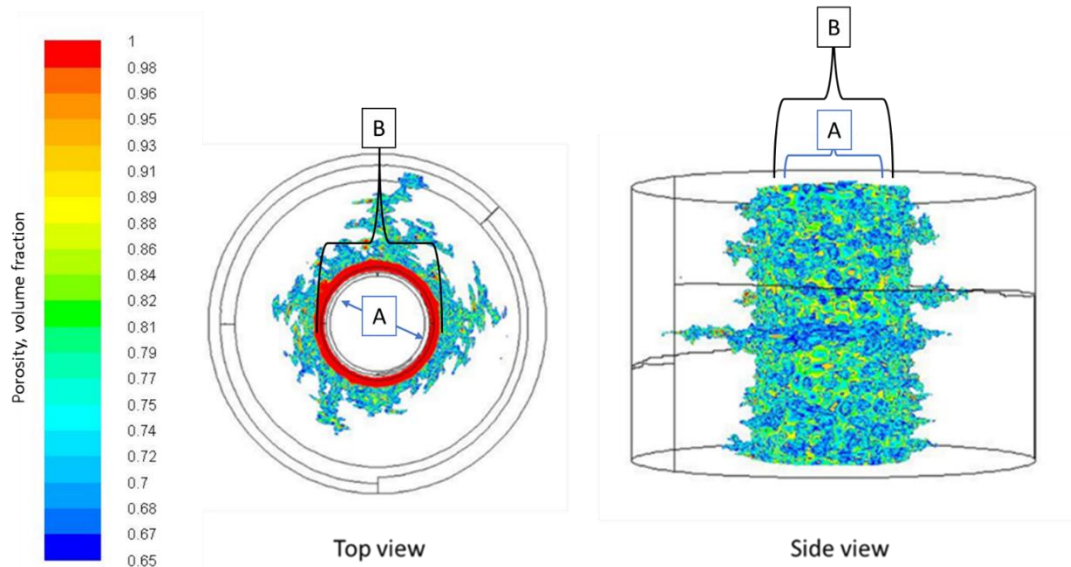
Figure 31 Top and side views of dissolution pattern from the optimum rate simulation. A is the original wellbore diameter, while B is the after acidizing wellbore diameter. 15 wt% HCl at 150^{0}F.
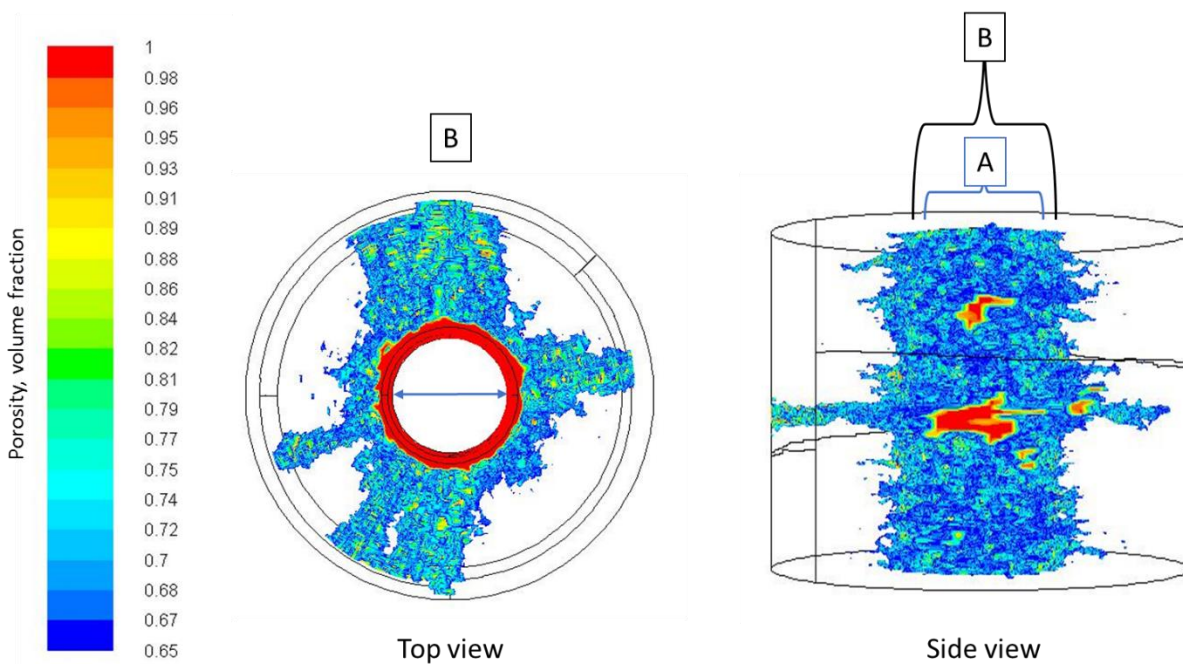
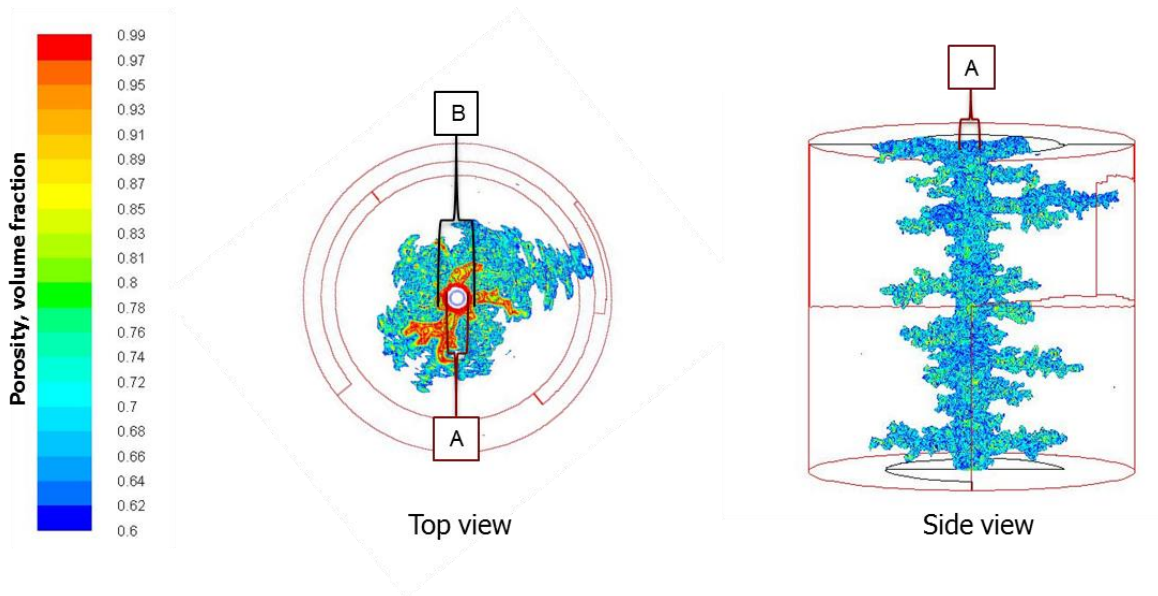**Figure 32 Top and side views of dissolution pattern from the high rate simulation. A is the original wellbore diameter, while B is the after acidizing wellbore diameter. 15 wt% HCl at 150^{0}F.**

At low injection rates, a wellbore enlargement from 6 in. diameter to nearly 10 in. was noticed. The total injection time to penetrate the 0.5 ft. of the formation was about 17 hours using a total volume of 4.5 gallons of acid. The injection rate seems to be unpractical, but under real field conditions where hundreds of feet's of different properties and formation pressures are treated. It is not uncommon to have zones with near zero injection rates. At moderate and high injection rates, a wellbore enlargement from 6 in. diameter to about 7.5 in. was noticed. Near optimum injection time to penetrate the 0.5 ft. of the formation was about 1 hour using a total volume of 1 gal of acid. It is intuitively obvious that for rates higher than the optimum, the higher the rate, the less the time and the higher the total acid volumes. **Figure 33** presents the total volume of acid to breakthrough as a function of the inlet velocity. Regardless the injection rate, the deeper the acid penetration, the more volume of acid will be required (**Fig. 33**). This explains the low volumes of acid in current simulations in comparison with real field data, where the volumes of acid reaches 75 gal/ft. for an average stimulation radius of 15 ft. (Furui et al. 2012).
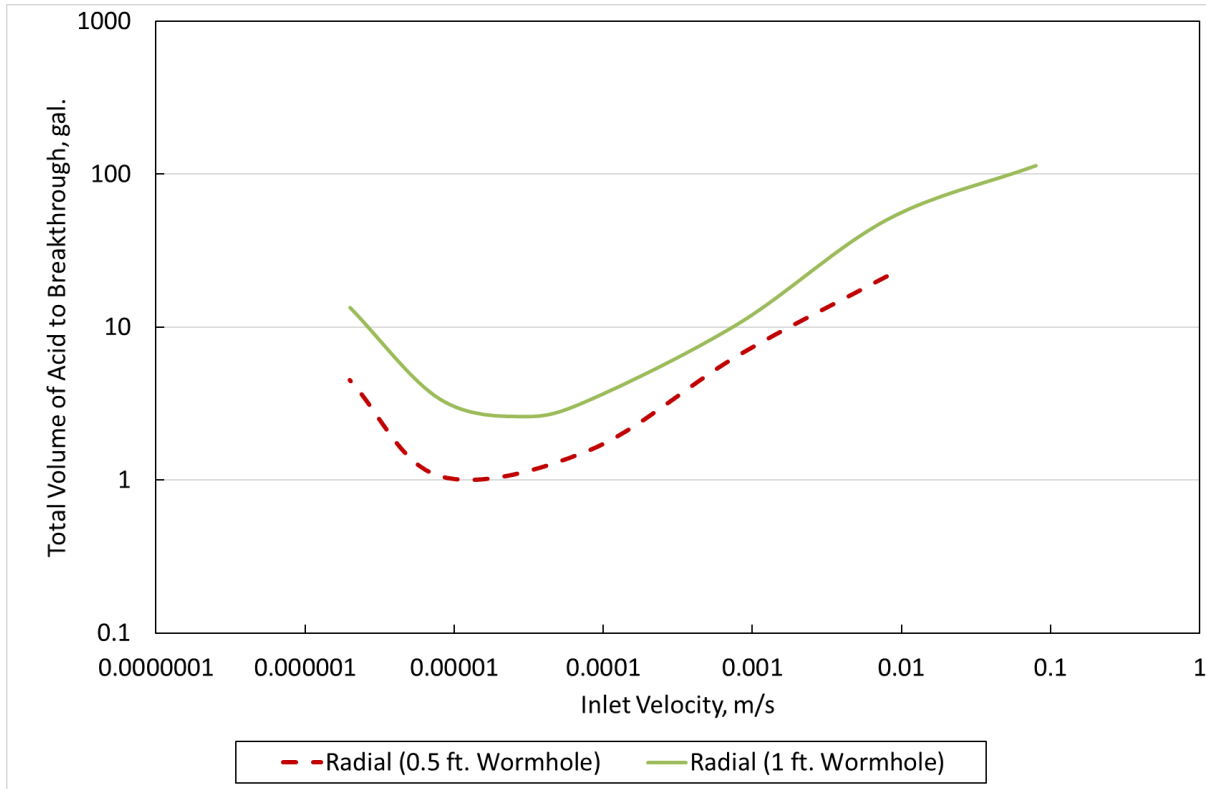
Figure 33 A comparison of the acid volume to breakthrough curves for the 1.5 ft. diameter model (maroon, dashed line), and the 2.5 ft. diameter model (green, solid line). 15 wt% HCl at 150⁰F.

Based on the previous results, it is expected to have large volumes of unspent acid around the wellbore during acidizing operations. Those volumes are mainly driven by gravity, leading to acid flow downward. That causes cross-flow and in worst case acid flow path can invade the underlying water. That may explain the increase in water production after many acidizing operations. Accordingly, current acidizing design simulators should account for the gravity component during acidizing operations to provide a more realistic design.

7.3. Adjusting The 1-D Upscaling Models Based on Radial Simulations

In this section, a half-cylinder model was built to allow deeper investigations inside the formation. The model was built with a wellbore of 0.5 ft. and formation that extends 3 ft. deep; the thickness of the model is 1 ft. as shown in **Figure 34**. Like the previous radial models, the porosity distribution was obtained from the Dolomite cores CT scans to assure natural porosity distribution.
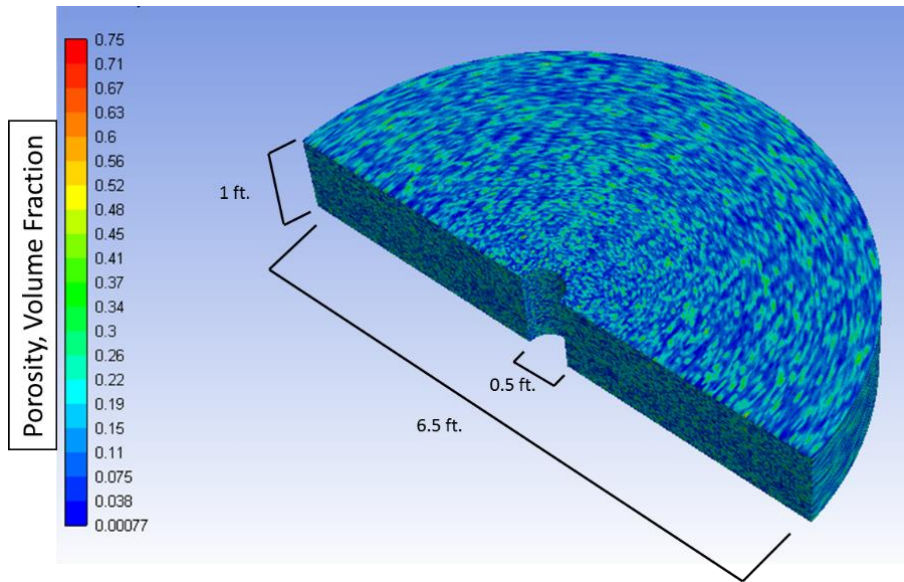
Figure 34 Initial porosity distribution of the Semi-cylindrical simulation model.

Figures 35 and 36 show the simulations of the large-scale model for 15 wt% HCl at 150°F and 20 wt% HCl at 200°F in comparison with the lab experiments, respectively. Injection velocity in the range of 8e-5 to 8e-2 m/s was studied using the large-scale model, lower rates are computationally expensive. The simulations of the 15 wt% HCl with dolomite at 150°F show

that the optimum injection velocity under field conditions is smaller than the optimum obtained using the 6 in. long and 1.5 in. diameter cores. Contrarily, the 20 wt% HCl with dolomite at 200°F simulations show that higher injection velocities are required to reach optimum conditions under field conditions. The discrepancy in the field behavior of the two studied cases can be attributed to the increase in the reaction rate and diffusive forces. As temperature increased from 150 to 200°F and acid concentration increased from 15 to 20 wt%, higher injection rates are required to overcome both the increase in the reaction rate and the H^+ diffusion. **Figures 37** presents a comparison between large-scale model simulations using 15 wt% HCl at 150°F and 20 wt% HCl at 200°F in field units.
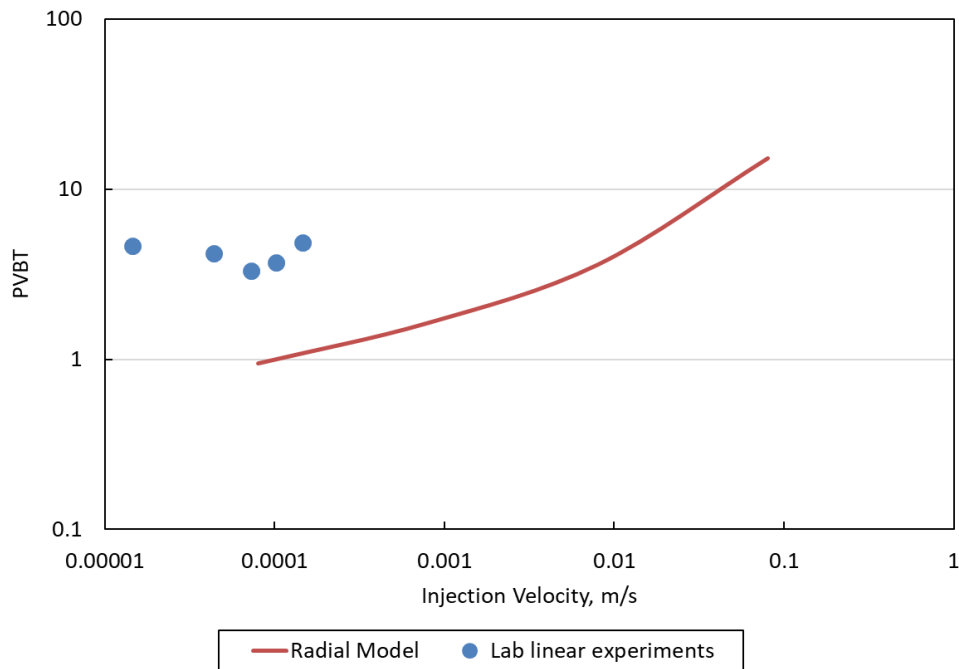
Figure 35 A comparison between lab experiments and large-scale model simulations. 15 wt% HCl at 150°F.
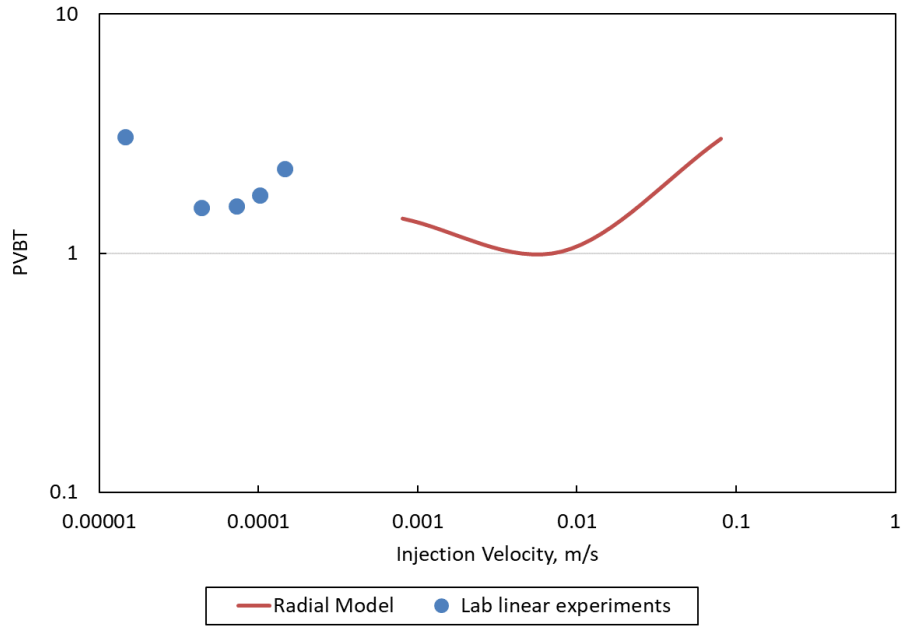
Figure 36 A comparison between lab experiments and large-scale model simulations. 20 wt% HCl at 200°F.
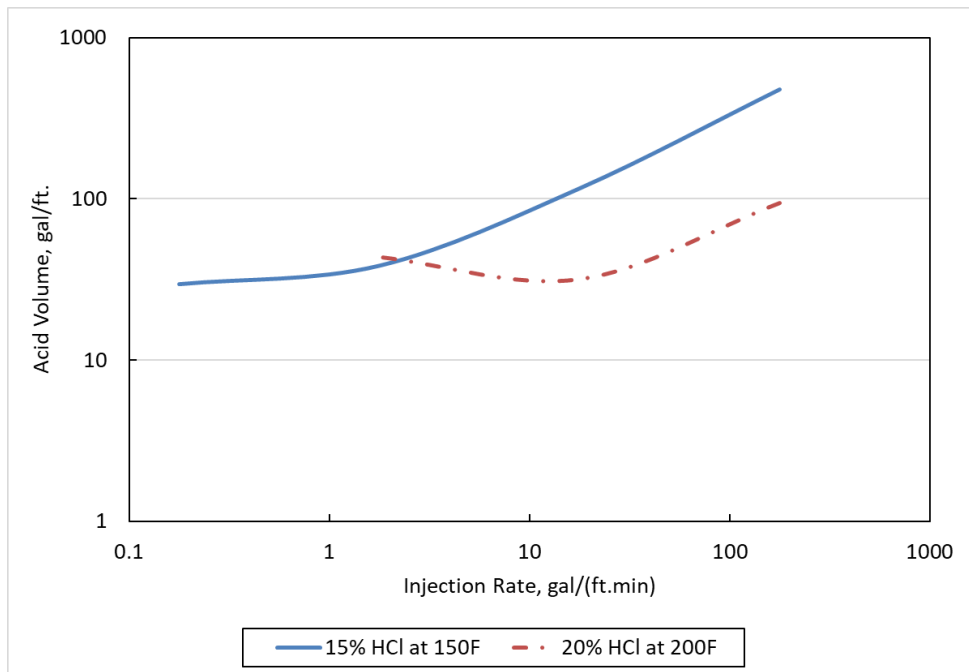
Figure 37 A comparison between large-scale model simulations using 15 wt% HCl at 150°F and 20 wt% HCl at 200°F.

Figure 38 shows a comparison between the two studied conditions on both lab and field scale. The results reveal that relations between different conditions of temperature and acid concentrations at field scale can be different than what established from linear core-flood experiments. This raises a concern about the accuracy of the traditional upscaling models (Buijse and Glasbergen 2005; Tardy et al. 2007), which rely on linear experiments to predict acid propagation in carbonate wells.
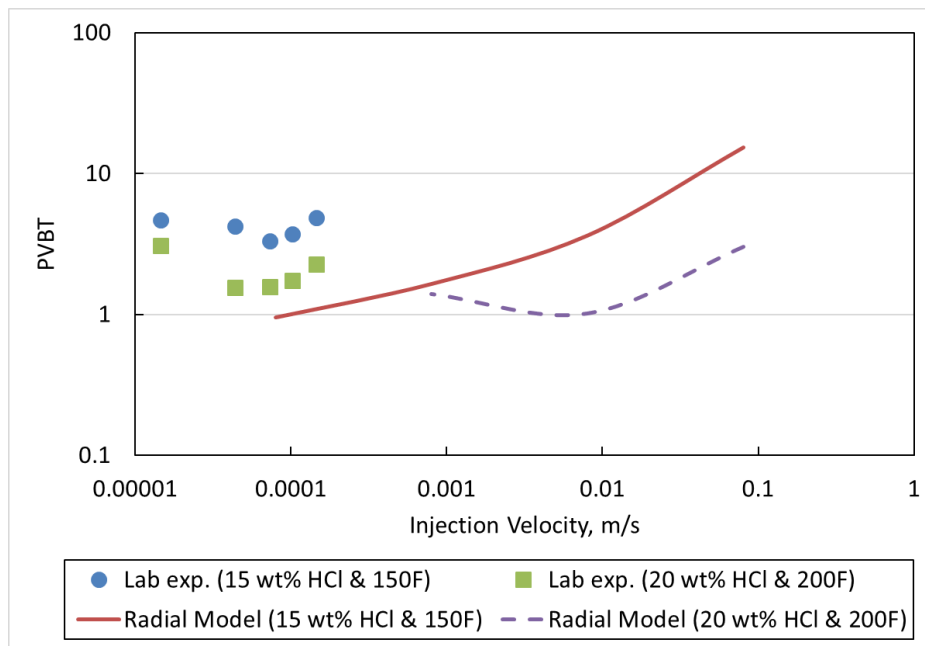
Figure 38 A comparison between lab experiments and radial model simulations using 15 wt% HCl at 150°F and 20 wt% HCl at 200°F.

Figure 39 presents a comparison between the large-scale model simulations, BG model and Tardy et al. model using 15 wt% HCl at 150°F. The simulation results show that acid treatment designs based on BG model can result in higher acid volumes. The results of the

simulation agree with the post field jobs analysis, which shows lower skin values than predicted based on the BG model (Furui et al. 2012). It is recommended to modify the BG model based on large scale simulations for better field designs. In the present study, the BG model was modified by changing the optimum interstitial velocity, the optimum PVBT, and the gamma exponent. Gamma exponent represents the loss in wormholing efficiency at velocities above the optimum (Buijse and Glasbergen 2005). Lower optimum conditions and higher gamma exponent were used to modify BG model. The modified BG model is shown in **Figure 39**.
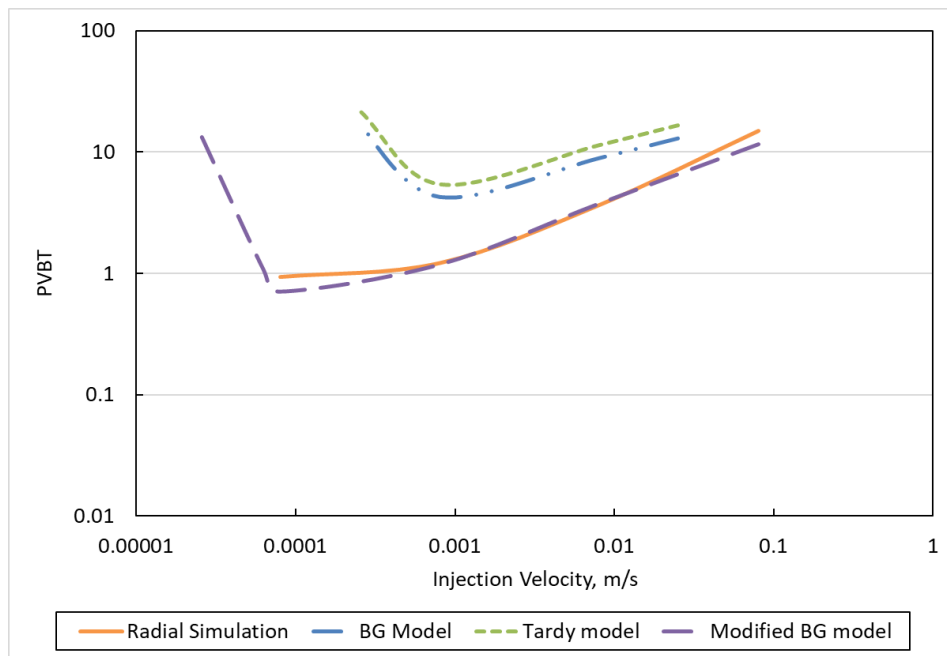
Figure 39 A comparison between simulation, BG, Tardy et al., and modified BG models. 15 wt% HCl at 150°F.

The comparison between the large-scale model simulations, BG model and Tardy et al. model using 20 wt% HCl at 200°F is shown in **Figure 40**. Contrarily to Fig. 11, the simulation

model predicted higher optimum injection velocity. Similar to the previous case, BG and Tardy et al. models predicted higher acid volumes than the large-scale simulation model. BG model was modified to follow the simulation model by decreasing the optimum PVBT and increasing both optimum injection velocity and gamma exponent.
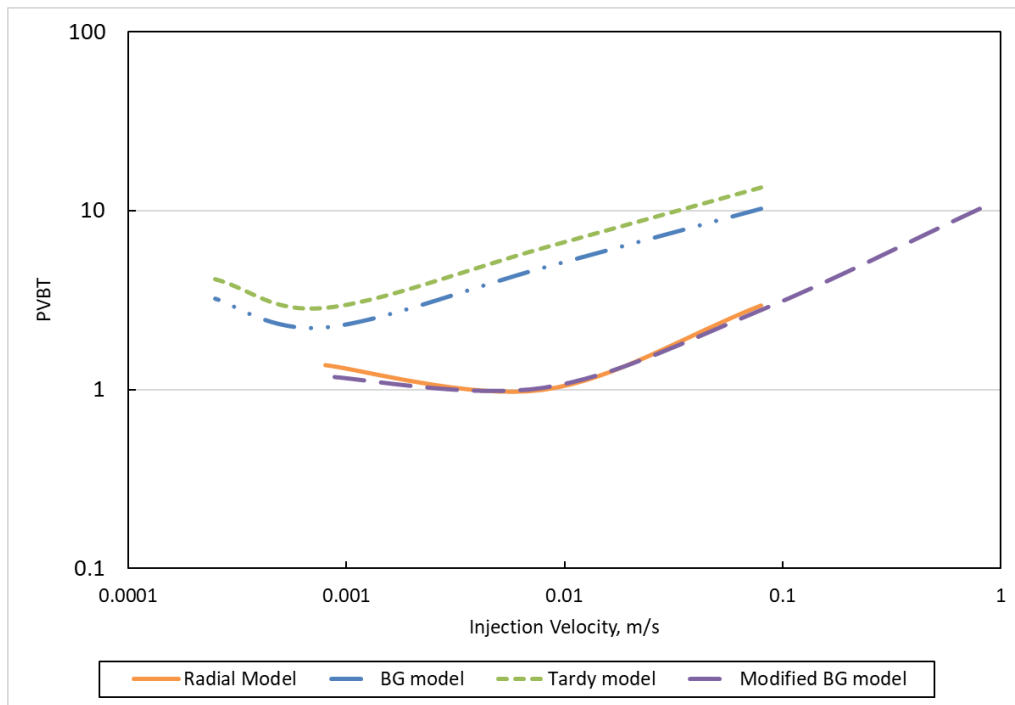
Figure 40 A comparison between simulation, BG, Tardy et al., and modified BG models. 20 wt% HCl at 200°F.

7.4. Using Radial Model in The Absence of Experiments

Collecting cores from the field and running CT scans and linear experiments is time-consuming and expensive. In the following, we present a methodology to predict acid performance using data from well logs only.

Figures 22 and 23 show that the porosity distribution can capture the effect of acid on different rock types. In the previous simulations, porosity distributions were extracted from CT scans, which is not available on the field scale. Accordingly, a reliable approach is to distribute the porosity statistically based on the natural porosity distribution in different rock types. **Figure 7** shows the porosity distribution in seven carbonate rocks; every rock type has its unique distribution. We recommend to statistically produce porosity distributions similar to natural porosity distributions found from CT scans.

Figure 41 shows the effect of porosity distribution on simulation results for dolomite acidizing at 150°F using 15 wt% HCl. Two of the distributions were generated based on CT scans, while the other three are statistically distributed. Statistical distribution was generated by fitting the CT scan based distribution to a gamma distribution or by randomly selecting values from the CT scan based distribution to generate the new distribution. **Figure 41** reveals that porosity distribution can cause up to 23% difference in the predicted acid volumes.
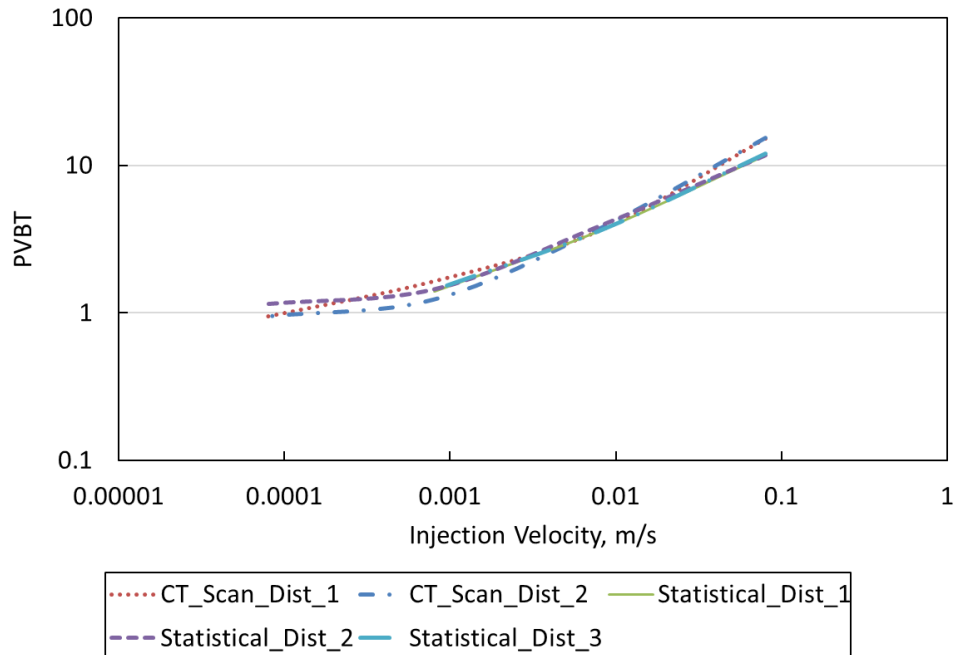
Figure 41 Effect of porosity distribution on simulation model results. 15 wt% HCl at 150°F.

The effect of porosity distribution on simulation results for dolomite acidizing at 200°F using 20 wt% HCl is presented in **Figure 42**. Two porosity distributions are shown, one generated from the CT scan while the other was statistically generated. At these conditions of temperature and concentration, the porosity distribution can cause around 21% difference in the predicted acid volumes. To account for the effect of porosity distribution in field designs, 25% extra volumes should be pumped.
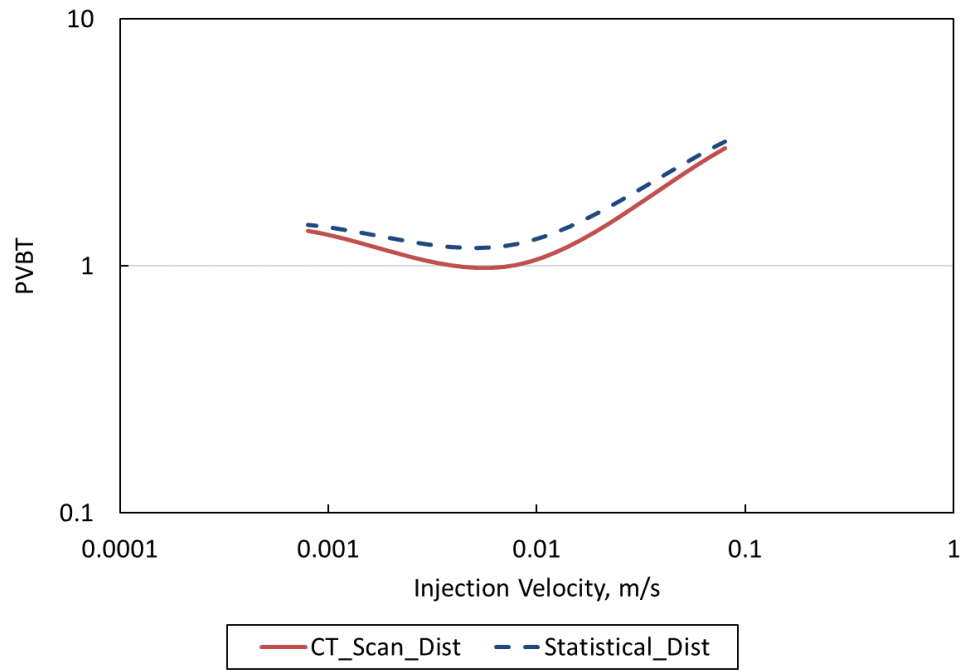
Figure 42 Effect of porosity distribution on simulation model results. 20 wt% HCl at 200°F.

8. SIMULATING RADIAL FLOW OF ACID IN HETEROGENEOUS DOLOMITE RESERVOIRS

8.1. Introduction

The presence of vugs and natural fractures in carbonate reservoirs is very common, and most of the world's prolific fields produce from these reservoirs. The co-existence of porous rock and open spaces over a wide range of scale complicates these reservoirs characterization and fluid flow modeling (Lucia 2007, Fadlelmula et al. 2015). Vugs and fractures can be characterized on the reservoir scale using seismic attributes and well test analysis; on the well scale using a combination of conventional, borehole image and nuclear-magnetic resonance (NMR) logs; and on the lab scale using routine core analysis, thin section, capillary pressure measurements, X-ray computed tomography, and NMR (Cannon et al. 1998; Iwere et al. 2002; Mai and Kantzas 2002, 2003; Gomaa et al. 2006; Narr et al. 2006; Lucia 2007; Nair et al. 2008; Izgec et al. 2010; Al-Muraikhi et al. 2012; Shafiei and Dusseault 2012; Ibrayev et al. 2016; Ali and Nasr-El-Din 2019). Fluid flow in these reservoirs should be described using equations that can simultaneously handle flow in porous and free-flow domains (Brinkman 1949; Arbogast and Brunson 2007; Popov et al. 2007; Yao et al. 2010).

Matrix acidizing is not well understood for vuggy and naturally fractured reservoirs because it is difficult to study in the lab, especially in the presence of large-scale vugs and/or natural fractures (Lucia 2007; Nair et al. 2008). Dong et al. (1999) studied experimentally the acid propagation in one fracture and they concluded that the width of the fracture affects the etching pattern. Dong et al. (2001) developed a mathematical model based on experimental work to study acid propagation in naturally fractured reservoirs and concluded that deeper acid penetration is expected in the presence of natural fractures. Chen et al. (2018) used a 3D linear

model to study the effect of fracture size, orientation, and permeability on acid propagation. They concluded that more acid volumes are required for larger fracture perpendicular to the flow direction. Ma et al. (2018) extended the work to include the effect of temperature and studied the process using a small-scale 3D model. The fractures were normally distributed and they concluded that lower acid volume is required in the presence of natural fractures. Aidagulov et al. 2019 conducted large scale radial experiments on a block with pre-existing fractures and they concluded that most of the acid is consumed in the fracture system. Dong et al. 2019 proposed a new numerical scheme to simulate complex acidizing processes. They studied the effect of natural fractures using a 2D linear model and concluded that the wormhole growth is strongly affected by the fracture system. Qi et al. 2019 studied the effect of fractures orientation on wormhole growth using the Two-Scale model. They concluded that parallele fractures accelerate the growth of the wormhole, while the perpendicular fractures hinder the acid propagation.

Izgec et al. (2010) conducted experiments and simulations to study the effect of vugs on acid propagation in limestone rocks. They used regular HCl acid at room temperature for the experiments and used the CT scan to predict the preferential flow path of the acid. They concluded that vugs accelerate the acid propagation in the carbonate rocks. Wang (2011) studied experimentally the acid response on homogeneous and vuggy carbonates using regular HCl acid at room temperature. Wang (2011) concluded that less acid is required for vuggy carbonates; the larger the vugs fraction the less the acid volume required. Also, it was shown that the size of the core has a significant effect of permeability and acid propagation. Zakaria et al. (2014) studied the propagation of emulsified acid at 230°F in vuggy dolomitic rocks. They concluded that smaller volume of acid is required in the presence of vugs. Akanni et al. (2017) studied the effect

of vugs on a 2D linear model and similar to the experimental results, they concluded that lower volumes of acid are required for the vuggy rocks.

All the previous studies discussed the qualitative effect of vugs and natural fractures, but none of these studies took a step toward quantifying the effects of the vugs and/or natural fracture on acid treatments. Also, none of the previous studies cited herein examined the effect of vugs and natural fractures using a radial model. Vugs and natural fracture size can be too large to be studied under lab conditions (Lucia 2007), which complicates the use of the experimentally based predictive models.

The objectives of this chapter are to use a field scale radial model to: (1) understand the effect of vugs size and number on acid propagation, (2) understand the effect of natural fractures length, angle, conductivity, and density on acid propagation, (3) build a surrogate model for each case to quantify the effect of vugs or natural fractures on acid propagation, and (4) study the composite effect of vugs and natural fractures on acid stimulation treatments.

8.2. Simulation Model Description

The 6.5 ft. diameter half-cylinder model presented in the previous section was utilized through this part of the study. The simulation parameters are identical to the values used for matching Silurian dolomite experiments using 15 wt% HCl at 150°F (**Table 5**). The simulations were run on the Texas A&M University (TAMU) High Performance Research Computing (HPRC) clusters. The wall-clock runtime using 32 processing cores was approximately 12 hrs at the highest rate, and nearly 10 days at the lowest studied rate (near optimum rate).

The quantification of the effect of vugs and natural fractures on the volume of injected acid is challenging because it involves a large number of parameters. Three variables are

63

considered to study the effect of vugs, whereas five variables are taken into account with the study of natural fractures. The study of this relatively large number of variables requires an engineered approach to save time and effort and, more importantly, to obtain general conclusions. In this study, the design of the simulation runs was conducted using a space-filling experimental design approach instead of changing one factor at a time (OFAT) (Santner et al. 2003). Initially, a number of runs were randomly generated for exploratory purposes, then a Latin Hypercube Design (LHD) is generated to augment the initial design with space-filling runs. Once the simulation runs have been conducted, a Gaussian Process (GP) model, which is a common statistical technique in computer simulation literature, was used to generate a surrogate model that accurately describes the functional relationship between the inputs and the corresponding response. The generated model can accurately predict acid performance at any condition within the space of variables.

8.3. The Gaussian Process Model

A Gaussian Process (GP) model is a non-parametric statistical technique commonly used in the computer simulation literature for surrogate modeling due to several desired properties including its flexibility and interpolative ability (Rasmussen et al. 2006). In a GP, the joint probability distribution of any finite collection of outputs $\boldsymbol{Y} = [Y_1, \dots, Y_N]^T$ follows as a multivariate normal distribution with an $N \times N$ covariance matrix denoted $\boldsymbol{K}$.

The main challenge in constructing a GP model involves determining the entries of $\boldsymbol{K}$ using a pre-specified parametric covariance function. A covariance function can be regarded as a measure of similarity between any pair of observations and is denoted by $\boldsymbol{C}(.,.)$. Assuming stationarity, a common choice is the Squared Exponential (SE) covariance function, which only

depends on the distance between any pair of observations, and can be written as shown in **Equation 15** (Rasmussen et al. 2006):

$$C(x_1, x_2) = \sigma^2 \exp\left(-\sum_{i=1}^{p} \theta_i |x_{1i} - x_{2i}|^2\right) \dots\dots\dots\dots\dots\dots\dots\dots\dots\dots\dots\dots \textit{Equation } \mathbf{15}$$

where $x_1 = \left[x_{11}, x_{12}, \dots, x_{1p}\right]^T$ is a realization of the set of input variables, p is the dimension of the input data, and $\{\sigma^2, \theta_1, \dots, \theta_p\}$ are the variance and scale parameters that are estimated given the available data using Maximum Likelihood Estimation (MLE). Once a GP is trained and the parameters are estimated, a point prediction at any untried test location x^* can be calculated as a linear combination of the observed outputs, as shown in **Equation 16** (Rasmussen et al. 2006):

$$\hat{Y}(x^*) = kK^{-1}Y \dots\dots\dots\dots\dots\dots\dots\dots\dots\dots\dots\dots\dots\dots\dots\dots\dots\dots\dots\dots \textit{Equation } \mathbf{16}$$

where k is the $1 \times N$ vector of covariances between the $N \times 1$ vector of observed outputs and $Y(x^*)$. For more details, authors refer to Rasmussen et al. (2006).

8.4. Base (Homogeneous) Case

In this case, the simulations were run without including the effect of vugs or natural fractures. Using the natural distribution obtained from the CT scans, four different injection velocities were studied to cover a broad range of field treatments. The radial model simulations for the 15wt% HCl at 150°F is shown in **Figure 35** (maroon curve) in terms of PVBT and in **Figure 37** (blue curve) in terms of field volumes. The dissolution patterns at the four rates appear in **Figure 43**, following the expected trend above the optimum point. At the lowest rate (near optimum), a wormhole pattern was achieved; as the rate increased, the wormholes became

thicker and more branched. The uniform dissolution was realized at the highest rate. In the

following sections, the lowest rate was excluded because it was computationally expensive.
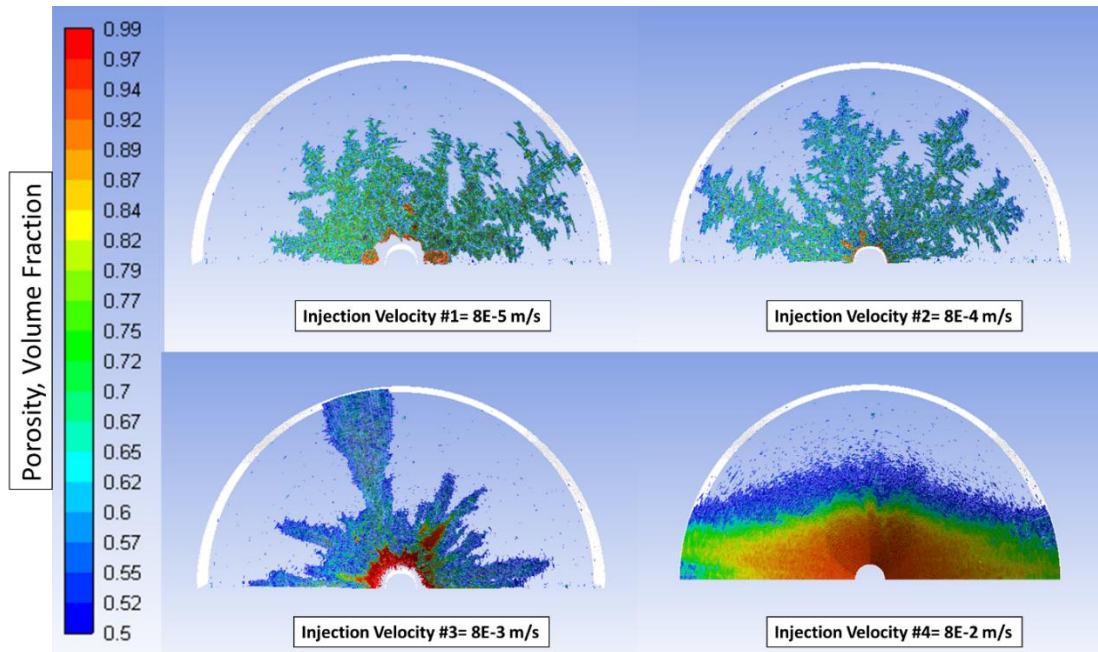
Figure 43 Acid dissolution patterns at different injection velocities. 15 wt% HCl at 150ºF.

8.5. Effect of Vugs

Vugs exist over a wide range of scales and shapes (Lucia, 2007; Huang et al. 2011).

Figure 44 shows actual examples of vuggy carbonates. Some vugs can be larger than the

wellbore, which prohibits studying flow in these rocks under lab conditions. For simplicity, the

current study assumes that all the vugs are spheres and have equal size. Vug radii ranging from

0.05 - 0.5 ft. were studied. Also, the number of vugs in the vicinity of the wellbore ranged from 1

to 50. The current section is concerned with separate vugs; the effect of the connected vugs will be presented in the following section.
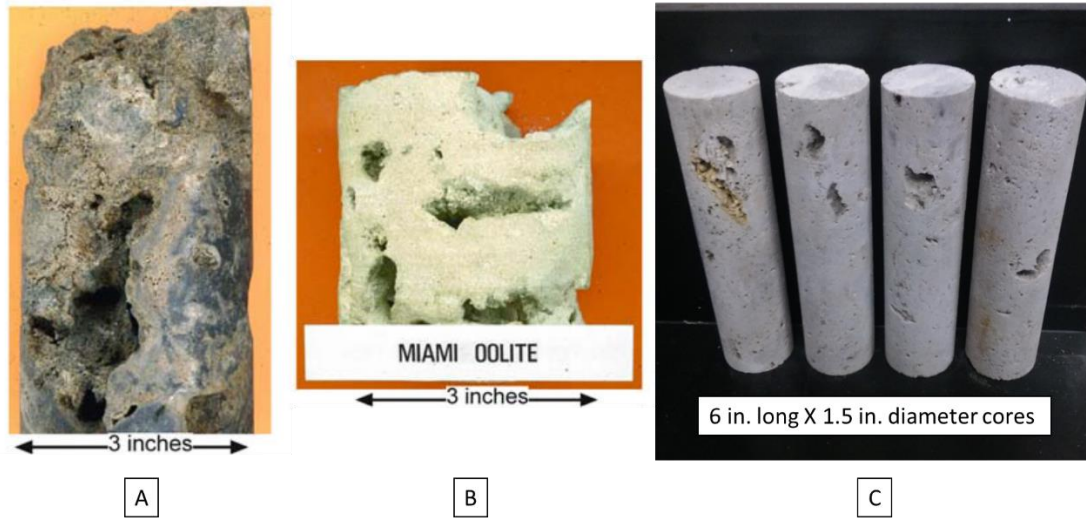
Figure 44 Real examples of large vugs: A) Cavernous pore space in a Niagran reef (after Lucia 2007), B) Caverneous pore space in Miami oolite (after Lucia 2007), and C) Vuggy pore space in Silurian dolomite cores.

Thirty-three simulations were run on the TAMU HPRC clusters to thoroughly study the effect of vug size and density on acid performance at three injection velocities. The vug parameters along with the injection rates were selected randomly (twenty-three runs) and using Latin hypercube sampling approach (ten runs) to ascertain full coverage of the variables. **Table 6** presents the simulation parameters for the thirty-three runs.

Figure 45 shows the effects of the vug size and number on the acid injection performance at the three studied rates. The y-axis of **Figure 45** quantifies the pore volume to breakthrough

(PVBT) indicator, which is the product of the injection velocity in m/s and time to breakthrough in seconds. At 8E-4 m/s injection rate (**Figure 45 A and B**), the increase in vug size and number results in a lower volume of acid to stimulate the reservoir; the presence of vugs always results in lower acid volumes. At 8E-3 m/s injection rate (**Figure 45 C and D**), there is no direct relation between vugs size and PVBT indicator but increasing the number of vugs decreases the PVBT indicator. At 8E-2 m/s injection rate (**Figure 45 E and F**), the relation between vug radius and PVBT indicator is almost constant up to vugs radii of 0.32 ft. and PVBT indicator decreases for higher vug radii. The relation between vug number and PVBT indicator is almost constant at the highest rate.

Table 6 A list of the simulation run inputs and outputs (injection rate, vug radius, and number of vugs). 15 wt% HCl at 150⁰F.

Case Number	Injection rate, m/s	Radius, ft.	Number of vugs
V1*	8.E-04	0	0
V2	8.E-04	0.5	1
V3	8.E-04	0.25	1
V4	8.E-04	0.1	1
V5	8.E-04	0.25	2
V6	8.E-04	0.1	12
V7	8.E-04	0.1	32
V8	8.E-04	0.25	32
V9	8.E-04	0.05	32
V10	8.E-04	0.25	18
V11	8.E-04	0.45	8
V12	8.E-04	0.21	21
V13	8.E-04	0.30	40.5
V14*	8.E-03	0	0
V15	8.E-03	0.5	1
V16	8.E-03	0.25	1
V17	8.E-03	0.1	1
V18	8.E-03	0.1	32
V19	8.E-03	0.25	32
V20	8.E-03	0.05	32
V21	8.E-03	0.5	8
V22	8.E-03	0.25	12
V23	8.E-03	0.15	45
V24	8.E-03	0.40	2
V25	8.E-03	0.08	18
V26*	8.E-02	0	0
V27	8.E-02	0.5	1
V28	8.E-02	0.25	1
V29	8.E-02	0.1	1
V30	8.E-02	0.1	32
V31	8.E-02	0.25	32
V32	8.E-02	0.05	32
V33	8.E-02	0.05	50
V34	8.E-02	0.13	32
V35	8.E-02	0.18	36
V36	8.E-02	0.32	24.5

* Base case runs.
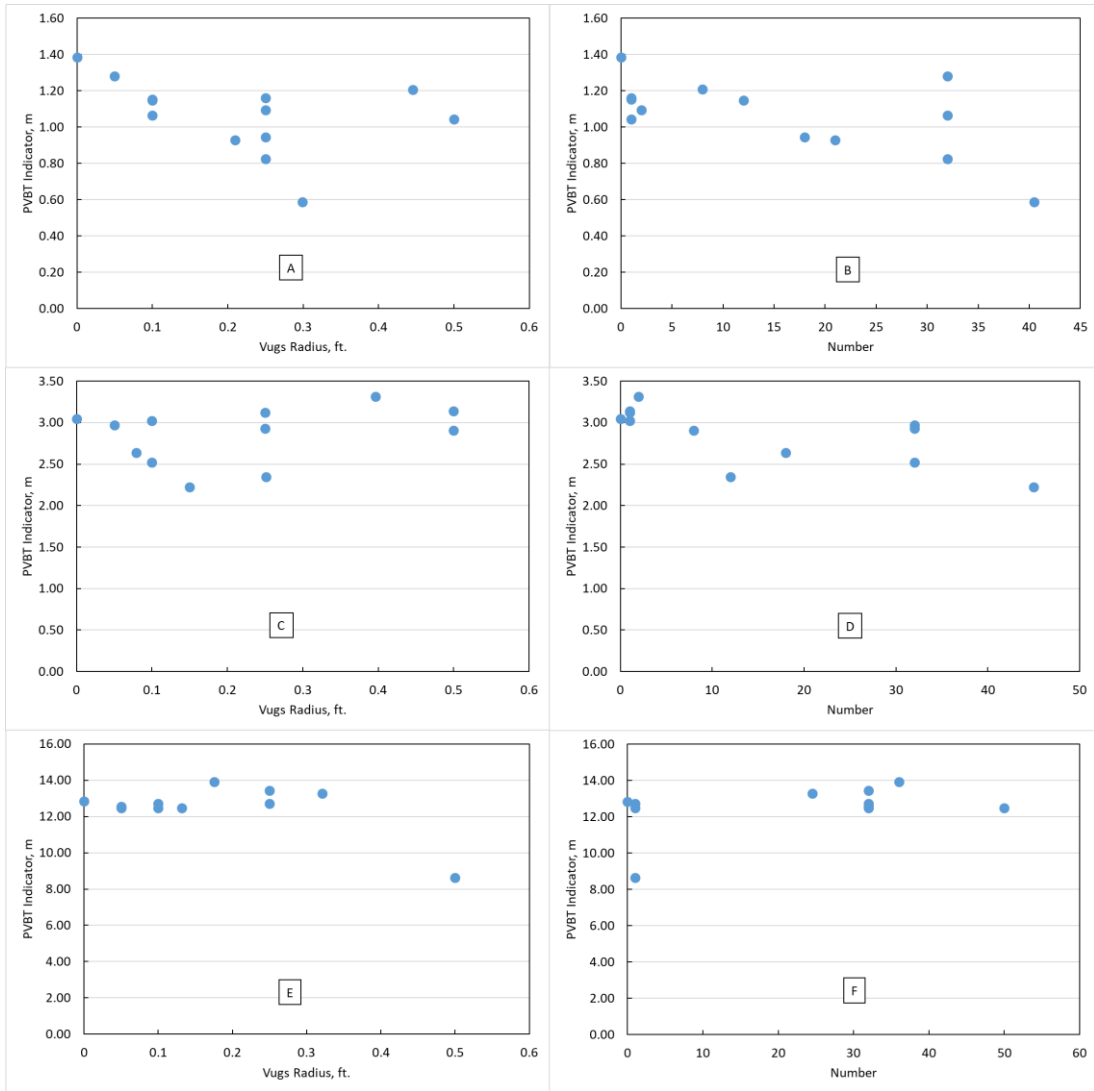
Figure 45 The effect of vug properties on PVBT indicator at different injection rates. A) Effect of vugs radius at 3E-4 m/s. B) Effect of the number of vugs at 3E-4 m/s. C) Effect of vug radius at 3E-3 m/s. D) Effect of the number of vugs at 3E-3 m/s. E) Effect of vug radius at 3E-2 m/s. F) Effect of the number of vugs at 3E-2 m/s.

The results of **Figure 45** shed light on the effect of large vugs. At the lowest rate, large vugs (radius > 0.45 ft.) resulted in an increase in PVBT indicator, because these large spaces will consume a large amount to be filled. At the highest rate, these large vugs assisted the acid

70

propagation because only a large low resistance path can drive the large volumes of acid injected. At the intermediate injection rate, the effect is a combination of the two previous cases.

Figures 46 and **47** present the simulation results of case V12 in **Table 6**. **Figure 46** shows the porosity distribution before and after acid injection. A comparison between **Figures 43 and 46** reveals that the presence of vugs guided the flow of acid and resulted in less branching. **Figures 43 and 46** explain the decrease in the PVBT indicator from 1.38 to 0.93 m due to the existence of vugs. **Figure 47** presents the acid concentration in the model after acid injection, it draws attention to the substantial amount of acid present after acid injection.
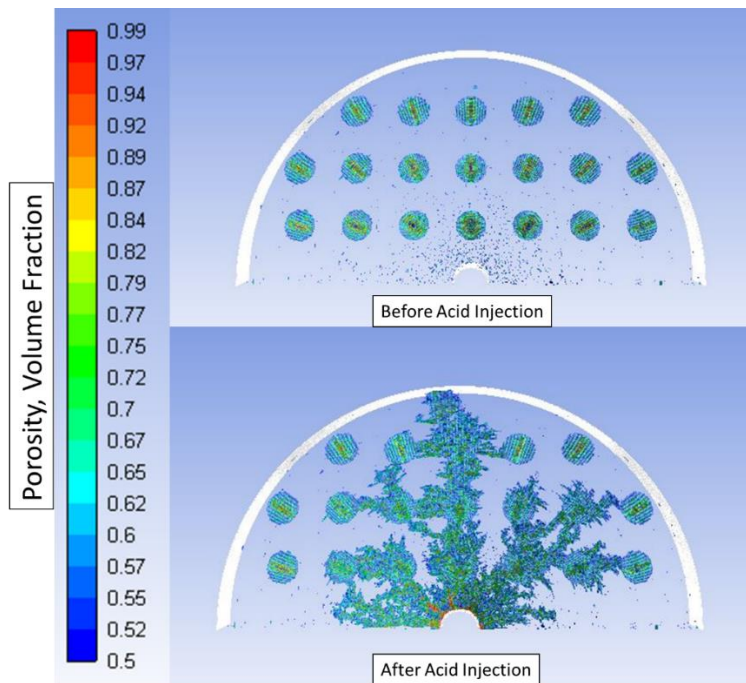

Figure 46 Case V12 porosity distribution before (top) and after (bottom) acid injection.
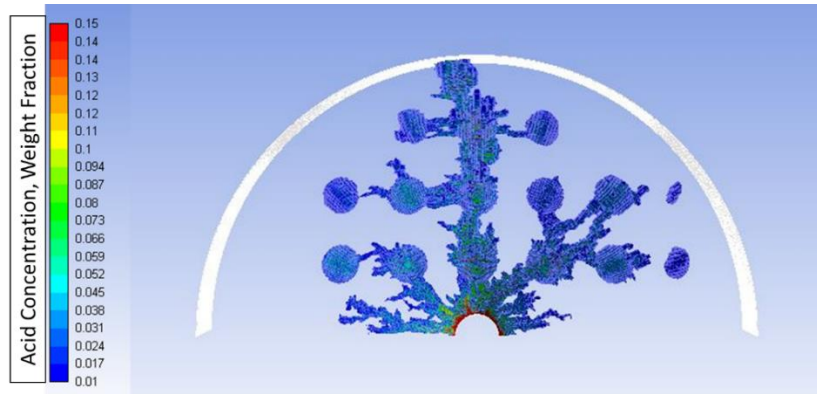
Figure 47 Case V12 acid concentration after acid injection.

Figures 48 and **49** present the simulation results of case V22 in **Table 6**. A comparison between **Figures 43 and 48** shows that the acid propagation path followed the vug pattern, decreasing the PVBT indicator from 3.05 to 2.34 m. **Figure 49** presents the acid concentration in the model after acid injection. Similar to case V12, a substantial amount of acid is present after acid injection.

Figures 50 and **51** present the simulation results of case V35 in **Table 6**. Contrary to the two previous cases, **Figure 50** shows that the presence of vugs results in guiding the acids to a larger volume around the wellbore when compared to the base case (**Figure 43**). The increase in PVBT indicator from 12.8 to 13.9 m complements the results shown in **Figure 50**. The acid concentration in the model after acid injection is shown in **Figure 51**. Again, a large amount of acid is present after acid injection. Acidizing flowback analyses in vuggy carbonates showed high acid concentrations in the samples. The field observations indicate the existence of unreacted acid at the end of the treatment and supports current simulation results. Accordingly, it is recommended to increase the soaking time in these reservoirs.
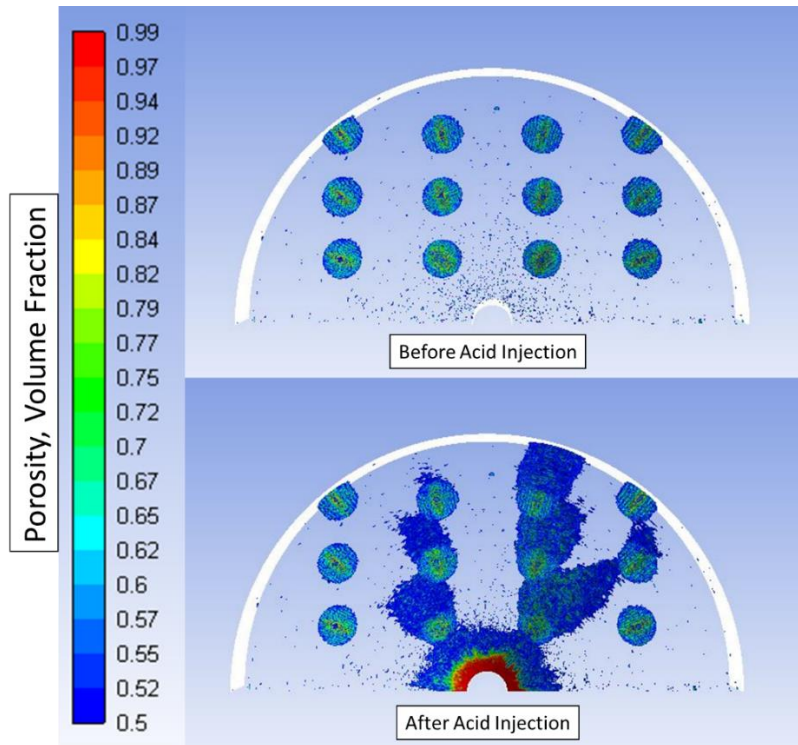
Figure 48 Case V22 porosity distribution before (top) and after (bottom) acid injection.
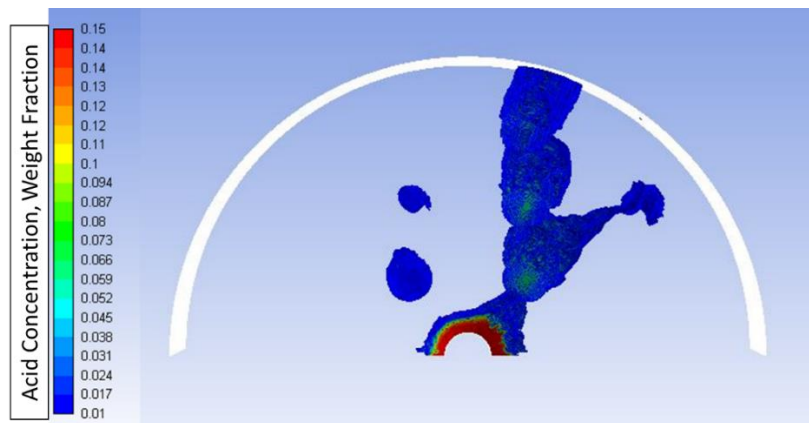
Figure 49 Case V22 acid concentration after acid injection.
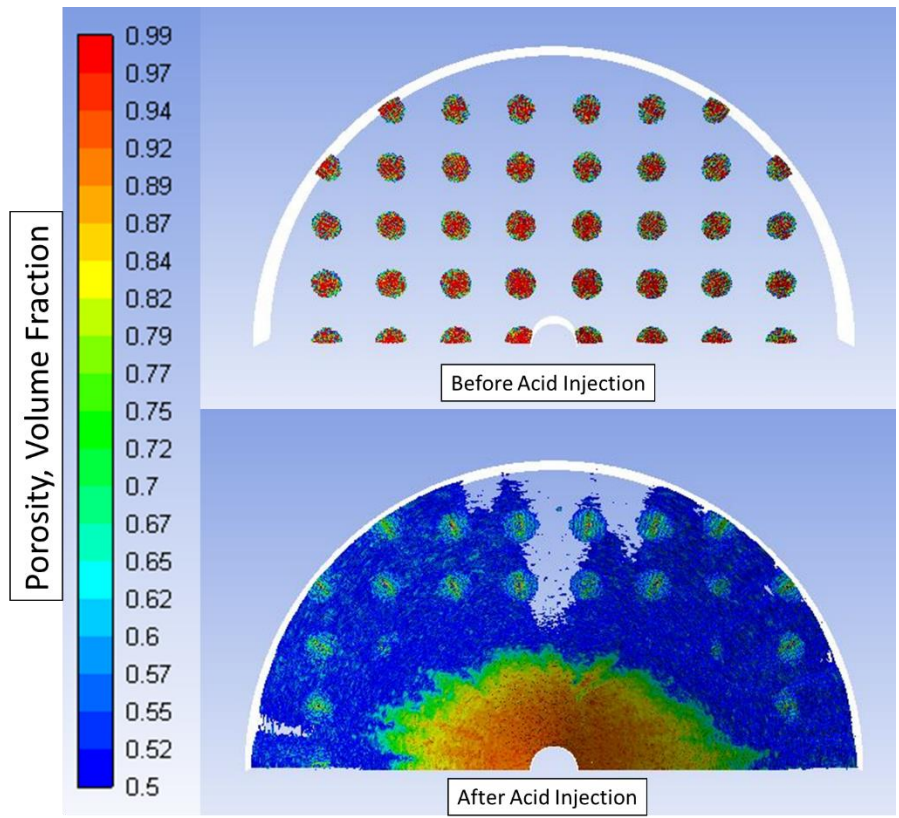
Figure 50 Case V35 porosity distribution before (top) and after (bottom) acid injection.
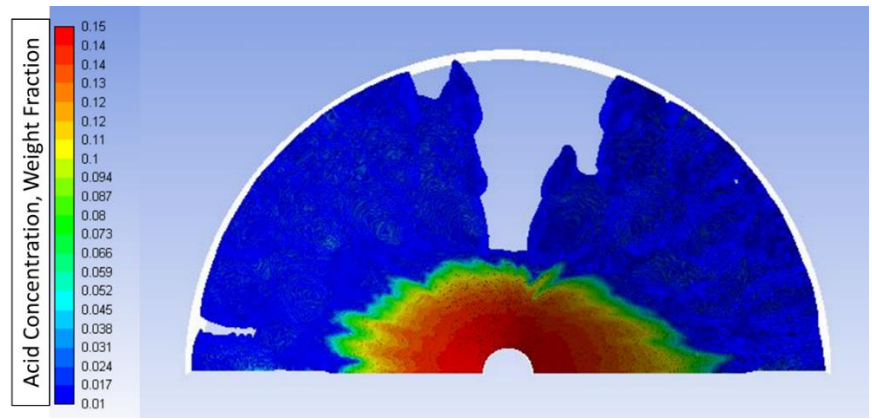
Figure 51 Case V35 acid concentration after acid injection.

The surrogate model was generated using the GP model, as mentioned earlier. For testing the predictive ability of the final surrogate model, six points were randomly selected out of the thirty-six available data points. As such, the remaining thirty data points are used to train the GP model as shown in **Figure 52**. The actual testing observations and their corresponding GP predictions are presented in **Figure 53**. The proximity of the predicted to the actual values indicates that the GP is able to produce a satisfactory prediction performance. The mean absolute percentage error is 10.3%. **Figure 54** visualizes the actual observations versus the predictions, which approximately lie on the diagonal line, indicating quality predictive power.
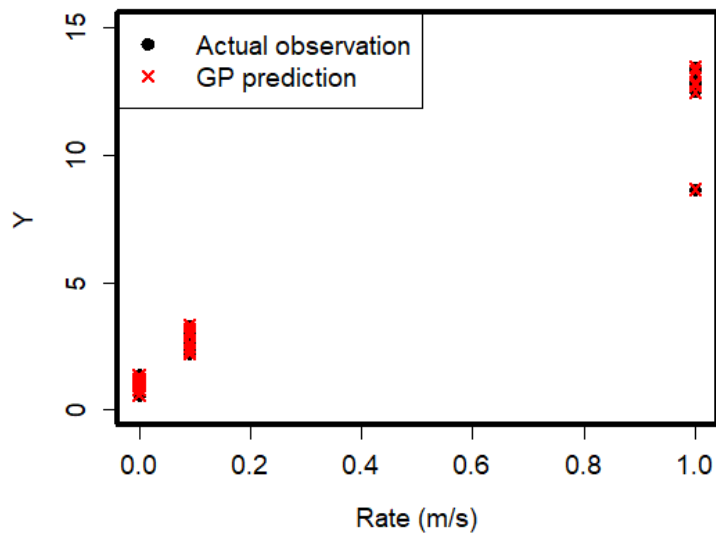
Figure 52 The match between actual observations (black dots) and GP model predictions (red x's) for the vug case training data set. Y is the PVBT indicator.
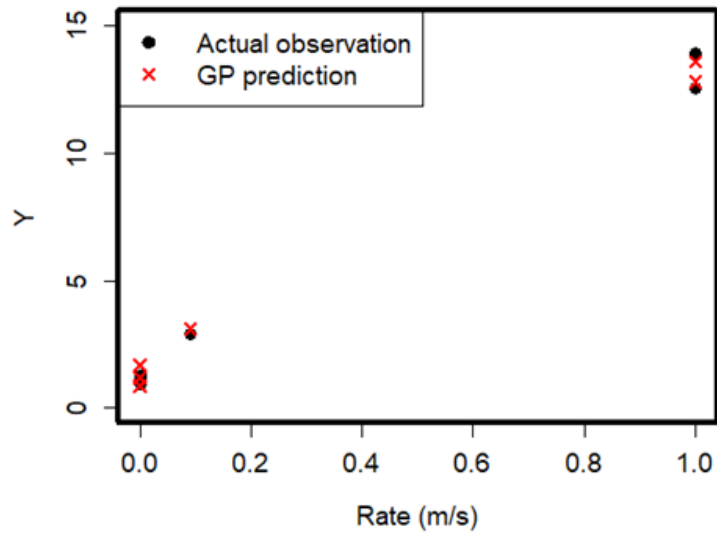
Figure 53 The match between actual observations (black dots) and GP model predictions (red x's) for the vugs case testing (blind) data set. Y is the PVBT indicator.
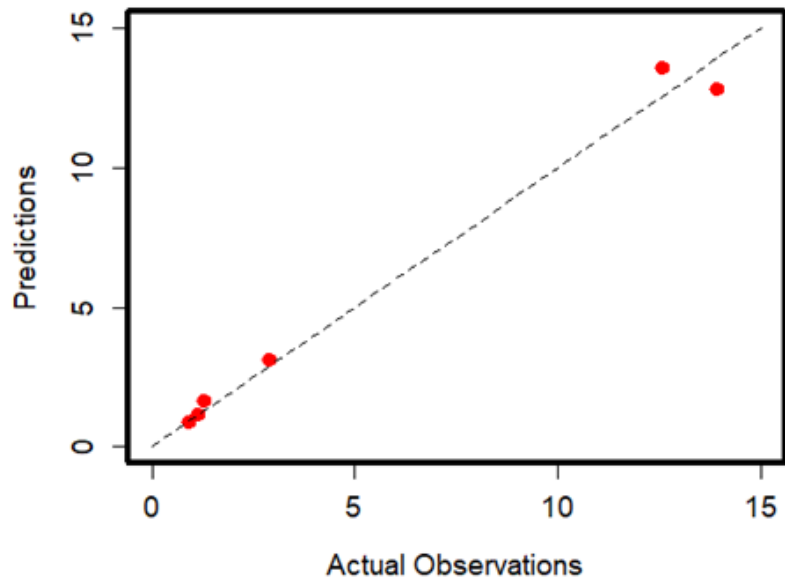
Figure 54 Actual observations versus GP model predictions for the vug case.

8.6. Effect of Natural Fractures

Natural fractures can be observed as microcracks or as mile-long features; these can be open or filled with fine-grained material and can take any direction based on the regional stresses (Narr et al. 2006). Widths of the fractures range from 10^{-5} to $5*10^{-2}$ cm (Dong et al. 1999). In the current study, four fracture properties (length, azimuth, fracture density, porosity) were studied at three injection rates. The length was studied over the range from 0.1 to 1 ft, and the height was assumed to be equal to the length. Shorter fractures can be studied in the lab, whereas longer ones fall beyond current model limitations. Fractures were assumed to be all vertical and parallel for simplicity. Two to twenty fractures were studied, and they were set either parallel or perpendicular on the model X-axis. Fractures porosity ranged from 0.6 to 1. Because it is impractical to simulate the actual fracture width, it was fixed to 0.05 ft. The simulated fracture width can be related to the natural fracture width using **Equation 17** (Dong et al. 1999) and **Equation 11**.

$$k_t = \frac{k_r w_r + k_f w_f}{w_r} \dots\dots\dots\dots\dots\dots\dots\dots\dots\dots\dots\dots\dots\dots\dots\dots\dots\dots\dots\dots\dots\dots\dots .. \; \textbf{\textit{Equation 17}}$$

where k_t is the total (simulated fracture) permeability, k_r is the rock permeability, k_f is the actual fracture permeability, w_r is the width of the rock (simulated fracture) and w_f is the width of the actual fracture.

Thirty simulations were run to study the effect of fracture length, angle, number and porosity on acid performance at three injection velocities. The fracture parameters along with the injection rates were initially selected randomly (eleven runs), then augmented using a Latin

hypercube sampling approach (nineteen runs) to ensure full coverage of the variables. Details of

the simulation runs are presented in **Table 7**.

Table 7 A list of the simulation run inputs (injection rate, fracture length, porosity, angle on X-axis, and number of fractures). 15 wt% HCl at 150⁰F.

Case	Injection rate, m/s	Length, ft.	Porosity	Angle on x-Axis, deg.	Number of fractures
NF1*	8.E-04	0	0	0	0
NF2	8.E-04	0.1	0.99	0	2
NF3	8.E-04	0.4	0.6	90	20
NF4	8.E-04	0.7	0.8	0	16
NF5	8.E-04	1	0.7	0	5
NF6	8.E-04	0.9	0.9	90	10
NF7	8.E-04	0.26	0.90	0	9
NF8	8.E-04	0.18	0.93	90	10
NF9	8.E-04	0.30	0.98	90	8
NF10	8.E-04	0.85	0.65	0	13
NF11	8.E-04	0.75	0.70	90	15
NF12	8.E-04	0.50	0.61	0	18
NF13*	8.E-03	0	0	0	0
NF14	8.E-03	0.1	0.6	0	16
NF15	8.E-03	0.4	0.8	90	2
NF16	8.E-03	0.7	0.9	0	5
NF17	8.E-03	1	0.99	90	20
NF18	8.E-03	0.9	0.7	90	10
NF19	8.E-03	0.41	0.73	0	11
NF20	8.E-03	0.89	0.88	0	7
NF21	8.E-03	0.69	0.86	0	5
NF22	8.E-03	0.58	0.69	0	16
NF23	8.E-03	0.64	0.67	0	19
NF24	8.E-03	0.60	0.63	0	12
NF25*	8.E-02	0	0	0	0
NF26	8.E-02	0.9	0.99	0	10
NF27	8.E-02	0.53	0.84	90	3
NF28	8.E-02	0.42	0.75	90	2
NF29	8.E-02	0.34	0.80	0	17
NF30	8.E-02	0.22	0.96	90	6
NF31	8.E-02	0.82	0.79	90	1
NF32	8.E-02	0.94	0.76	90	4
NF33	8.E-02	0.12	0.82	90	14

* Base case runs.

Figures 55 and 56 show the effects of fracture length, angle, number and porosity on the acid injection performance at the three studied rates. At 8E-4 m/s injection rate (**Figure 55 A and B and Figure 56 A and B**), the increase in the fracture length and number results in an earlier breakthrough. The PVBT indicator decreases with the increase of porosity until a certain limit is reached followed be an increasing trend. The composite effect (**Figure 56B**) shows that the increase in the fractures porosity, number, or length will be accompanied by a decrease in the PVBT indicator. The fracture orientation does not have a significant effect on acid propagation.

At 8E-3 m/s injection rate (**Figure 55 C and D and Figure 56 C and D**), the increase in the fracture length has no effect on acid volumes up to 0.5 ft., while longer fractures decrease the acid volumes required. The relation between fracture conductivity and the PVBT indicator is inversely proportional; the same correlation was observed between the number of fractures and the PVBT indicator. The composite effect (**Figure 56D**) shows that the increase in the fractures porosity, number, or length will be accompanied by a decrease in the PVBT indicator. The fracture orientation does not have a significant effect on acid propagation.
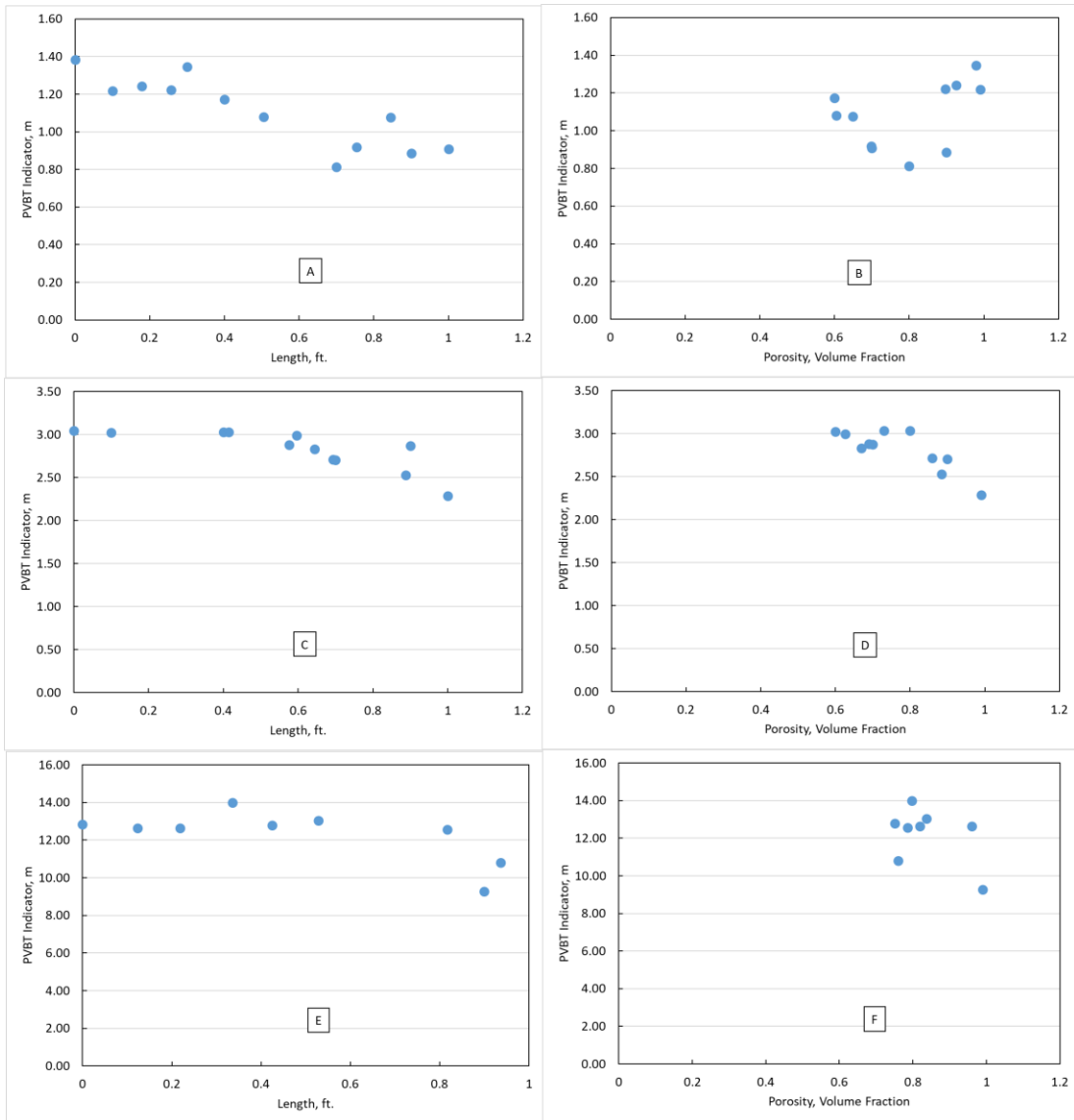
Figure 55 The effect of fracture length and porosity on PVBT indicator at different injection rates: (A) Effect of fracture length at 3E-4 m/s, (B) Effect of fracture porosity at 3E-4 m/s, (C) Effect of fracture length at 3E-3 m/s, (D) Effect of fracture porosity at 3E-3 m/s, (E) Effect of fracture length at 3E-2 m/s, and (F) Effect of fracture porosity at 3E-2 m/s.
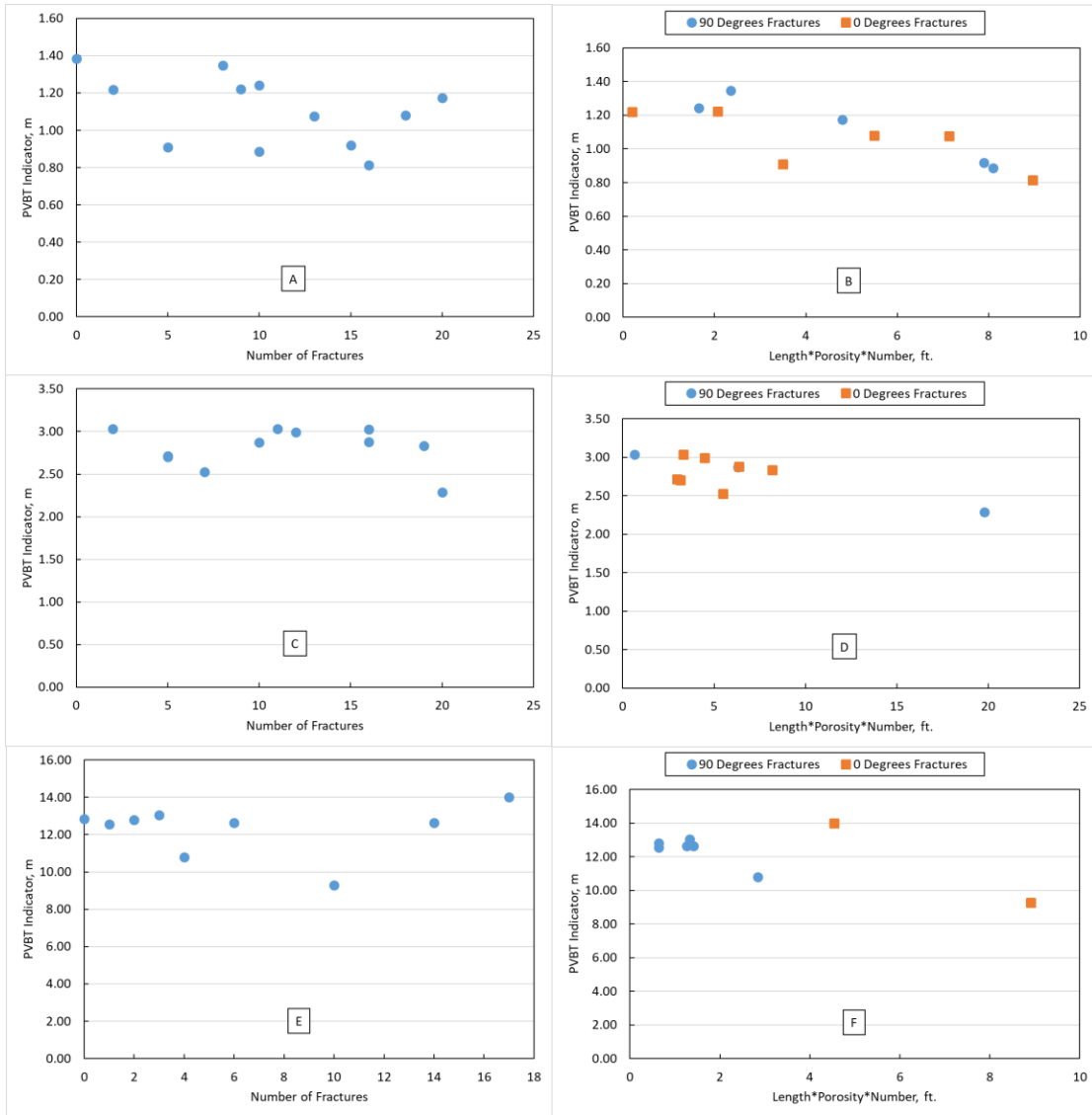
Figure 56 The effect of the number of fractures and orientation of PVBT indicator at different injection rates: (A) Effect of the number of fractures at 3E-4 m/s, (B) Effect of fracture orientation at 3E-4 m/s, (C) Effect of the number of fractures at 3E-3 m/s, (D) Effect of fracture orientation at 3E-3 m/s, (E) Effect of the number of fractures at 3E-2 m/s, and (F) Effect of fracture orientation at 3E-2 m/s.

At 8E-2 m/s injection rate (**Figures 55E and F and Figures 56E and F**), the increase in

the fracture length up to 0.6 ft. has no effect on PVBT indicator; longer fractures decrease the

81

acid volumes required. The correlation between fracture conductivity and PVBT indicator is inversely proportional. The PVBT indicator decreases with the increase in fractures number until a certain limit is reached followed by an increasing trend. The composite effect (**Figure 56F**) shows that the increase in the fracture porosity, number, or length will be accompanied by a decrease in the PVBT indicator. The fracture orientation does not have a large effect on acid propagation. The acid propagation at 8E-2 m/s for the base case (**Figure 43**) was parallel to the X-axis. The 0-degree angle fractures are perpendicular to the X-axis, resulting in a higher PVBT indicator for these cases when compared with the 90-degree fractures in **Figure 56F**. The conclusions drawn from linear models about the effect of fracture and/or vugs orientation (Izgec et al. 2010; Chen et. al 2018) are not applicable under field flow conditions. Based on results of this study, the fracture orientation has a minimal effect on fluid flow in general and should not be considered in acid designs.

Figures 57 and **58** present the simulation results of case NF11 in **Table 7**. **Figure 57** shows the porosity distribution before and after acid injection. Because the number of fractures is low, and the fractures are short in length, the dissolution patterns and PVBT indicator is close to the base case (**Figure 43** and **Table 7**). The same observation can be drawn from the final acid concentration (**Figure 58**).

Figure 57 Case NF11 porosity distribution before (top) and after (bottom) acid injection.

Figure 58 Case NF11 acid concentration after acid injection.

Figures 59 and 60 present the simulation results of case NF20 in Table 7. Figure 59 shows the porosity distribution before and after acid injection. In this case, the long and conductive fractures guided the flow of the acid, leaving a minimal amount of acid to invade the porous media. A comparison between Figures 43 and 59 shows the substantial effect of the fractures on the dissolution pattern. The final acid concentration (Figure 60) shows that the acid touched only three fractures and illustrates the effect of long conductive fractures on the dissolution pattern.

Figure 59 Case NF20 porosity distribution before (top) and after (bottom) acid injection.
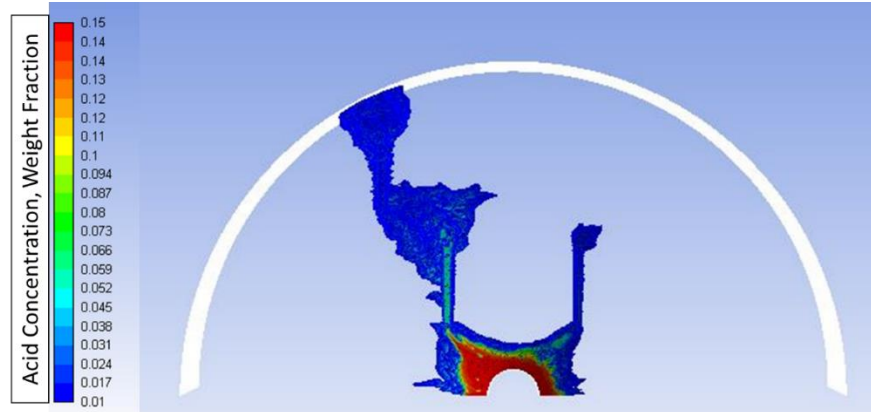
Figure 60 Case NF20 acid concentration after acid injection.

Figures **61** and **62** present the simulation results of case NF32 in Table 7. **Figure 61** shows the porosity distribution before and after acid injection. A comparison between the base case (**Figure 43**) and case NF32 (**Figure 61**) demonstrates that the existence of only four long fractures could have a substantial effect on the dissolution pattern and PVBT indicator (**Table 7**). The final acid concentration (**Figure 62**) confirms the actual dissolution pattern and shows that one of the fractures was not touched with the acid.
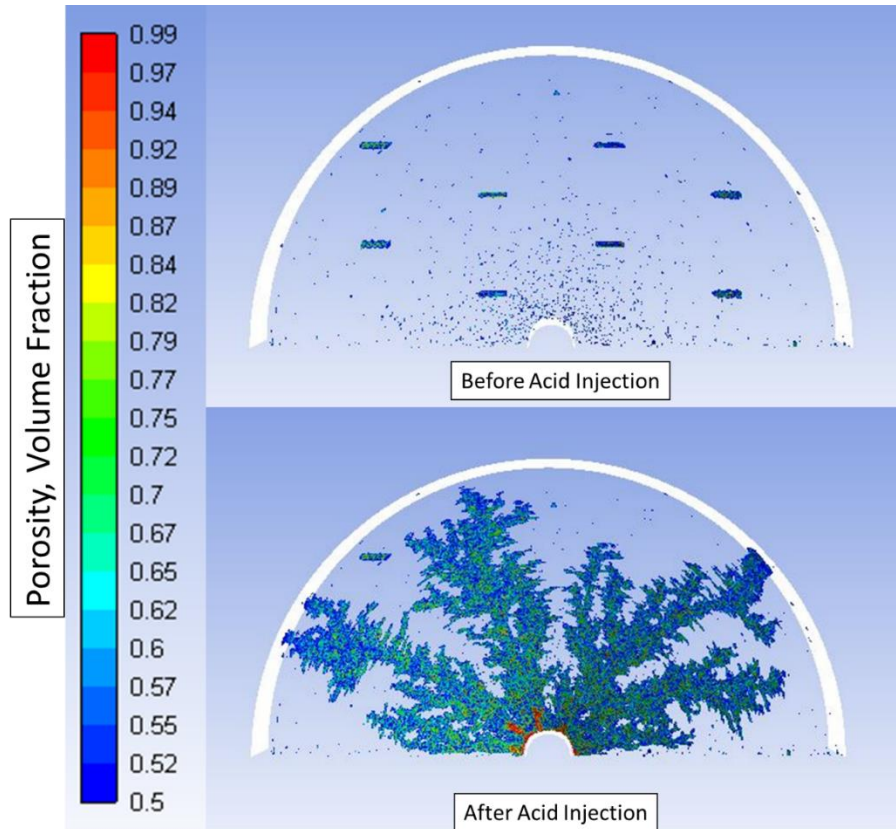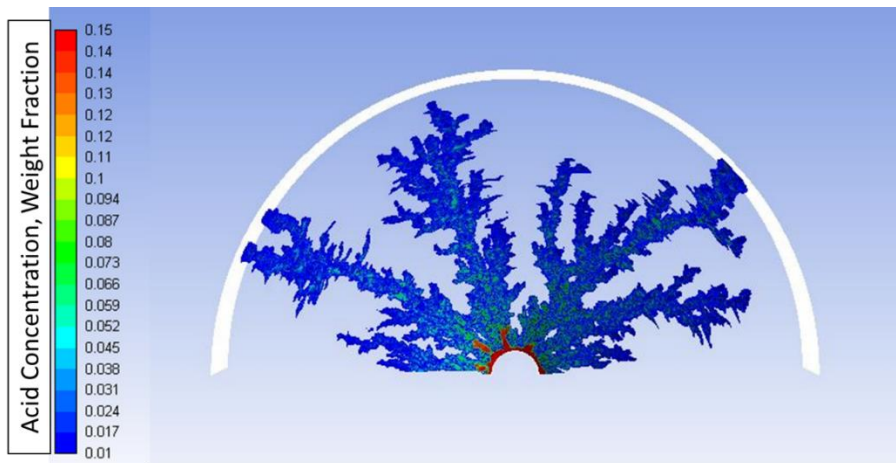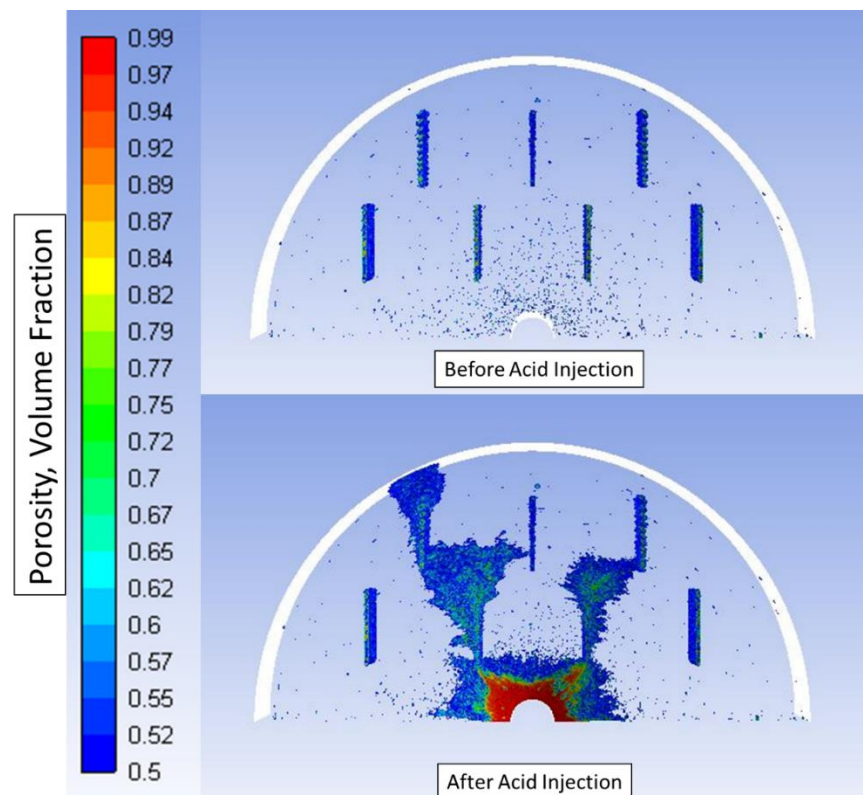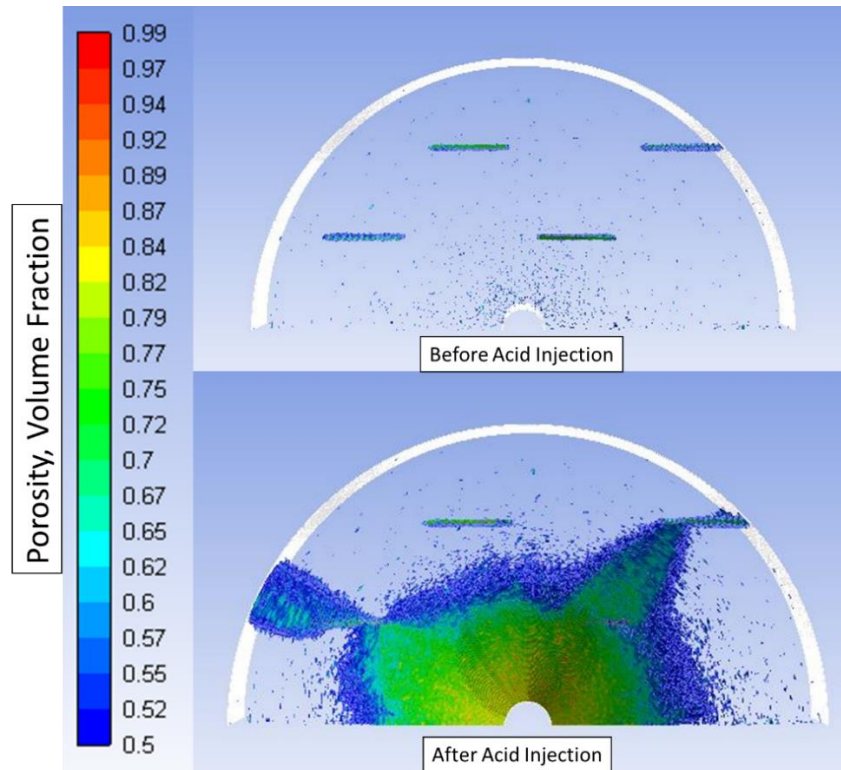
Figure 61 Case NF32 porosity distribution before (top) and after (bottom) acid injection.
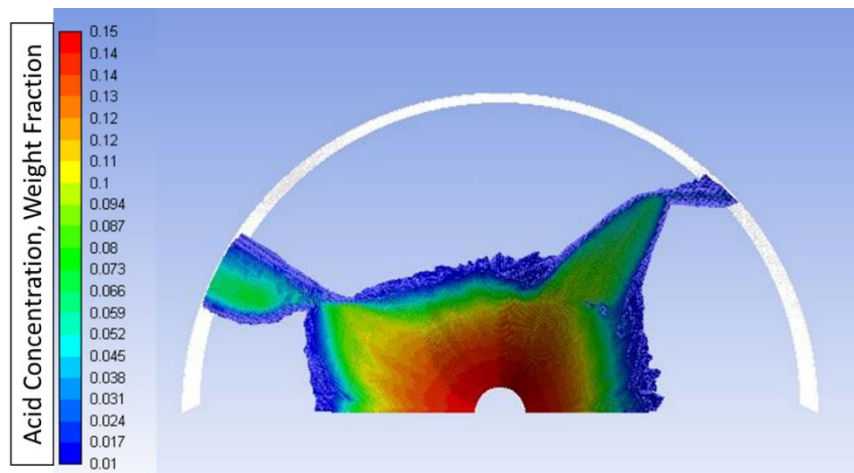
Figure 62 Case NF32 acid concentration after acid injection.

It can be concluded from the dissolution patterns of cases NF11, NF20, and NF32 that the acid will not reach all of the fractures, but it will flow into those fractures that carry the amount of acid injected. It is expected that at higher injection rates, more fractures will be touched by the acid.

Similar to the previous section, a surrogate model was generated to quantify the effect of natural fracture on acid treatment performance. The GP model was trained using twenty-seven observations as shown in **Figure 63.** A total of six points were randomly selected to test the GP model predictive capabilities. **Figure 64** shows the GP predictions for the test points. A mean absolute percentage error of 11.3% indicates that the GP is able to produce a satisfactory prediction performance. **Figure 65** shows the actual observations versus the predictions, which almost lie on the diagonal line.
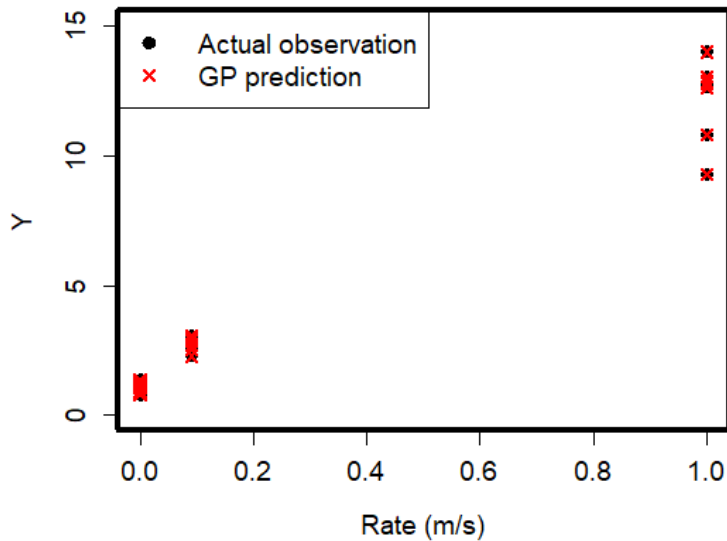
Figure 63 The match between actual observations (black dots) and GP model predictions (red x's) for the natural fractures case training data set. Y is the PVBT indicator.
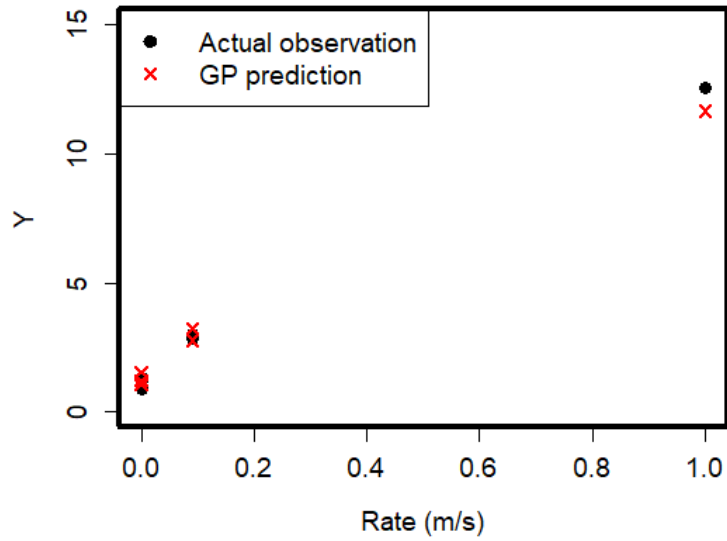
Figure 64 The match between actual observations (black dots) and GP model predictions (red x's) for the natural fractures case testing (blind) data set. Y is the PVBT indicator.
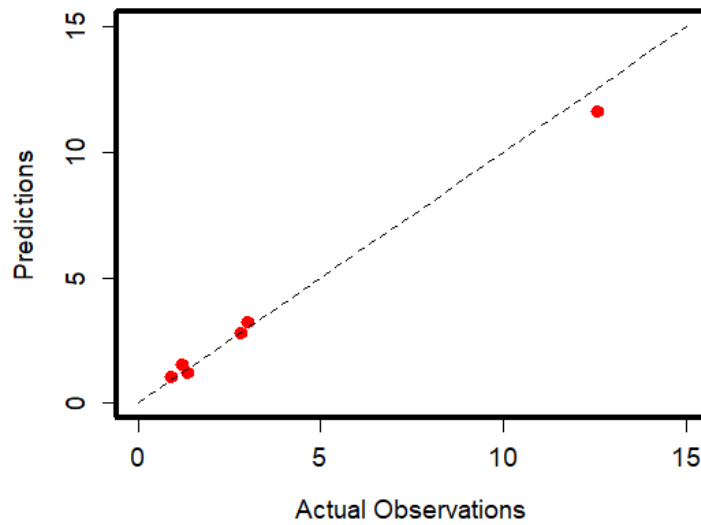
Figure 65 Actual observations versus GP model predictions for the natural fracture case.

8.7. Composite Effect of Vugs and Natural Fractures

In the previous sections, the effect of vugs and natural fractures were studied separately. But, the coexistence of vugs and fractures were observed in many carbonate fields (Camacho-Velazquez et al. 2005; Kang et al. 2006; Fadlelmula et al. 2015; Zhang et al. 2016; Yong et al. 2016). Lucia (2007) describes the coexistence of vugs and natural fractures as touching vugs. In the current section, the cases presented are combinations of cases from the two previous sections.

Case NFV1 is a combination of cases V8 and NF4. **Figure 66** shows the distribution of vugs and natural fractures (top part) and the porosity profile after acid injection (bottom). The existence of a conductive network of vugs and fractures limited the amount of acid that flows in the porous medium. **Figure 67** presents the final acid concentration and helps in determining the actual path of acid. Also, the large amount of acid in the vugs can be observed in Fig. 67. The coexistence of vugs and fractures helped the acid to flow more easily than in the cases where fractures and vugs exist separately. The PVBT indicators for cases NFV1, V8 and NF4 are 0.67, 0.82 and 0.81, respectively.

Case NFV2 is a combination of cases V22 and NF17. **Fig. 68** shows the distribution of vugs and natural fractures (top) and the porosity profile after acid injection (bottom). Similar to case NFV1, the existence of a conductive network of vugs and fractures limited the amount of acid that flows in the porous medium. **Fig. 69** presents the final acid concentration and helps in determining the actual path of acid. The coexistence of vugs and fractures provided an easy path for acid in comparison with the cases where fractures and vugs exist separately. Because the rate for NFV2 is a fold higher than case NFV1, the impact of the coexistence of vugs and fractures on the volume of acid required is less. The PVBT indicators for cases NFV2, V22 and NF17 are 2.21, 2.34, and 2.29, respectively.

89
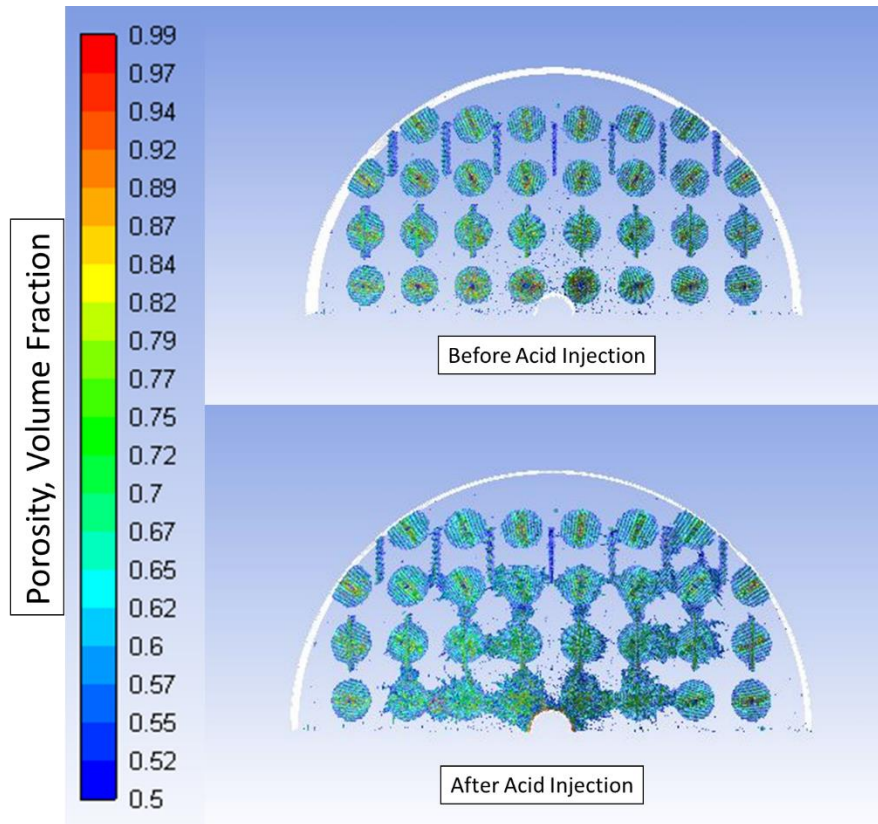
Figure 66 Case NFV1 porosity distribution before (top) and after (bottom) acid injection.

Case NFV3 is a combination of cases V36 and NF26. **Fig. 70** shows the distribution of vugs and natural fractures (top) and the porosity profile after acid injection (bottom). The presence of vugs drove the acid to contact higher volume of the formation. **Fig. 71** presents the final acid concentration and shows the acid passage. The reason behind the negative effect of the vugs is the high volume of acid consumed in vugs filling. The PVBT indicators for cases NFV3, V36 and NF26 are 11.2, 13.28 and 9.28, respectively.

Figure 67 Case NFV1 acid concentration after acid injection.
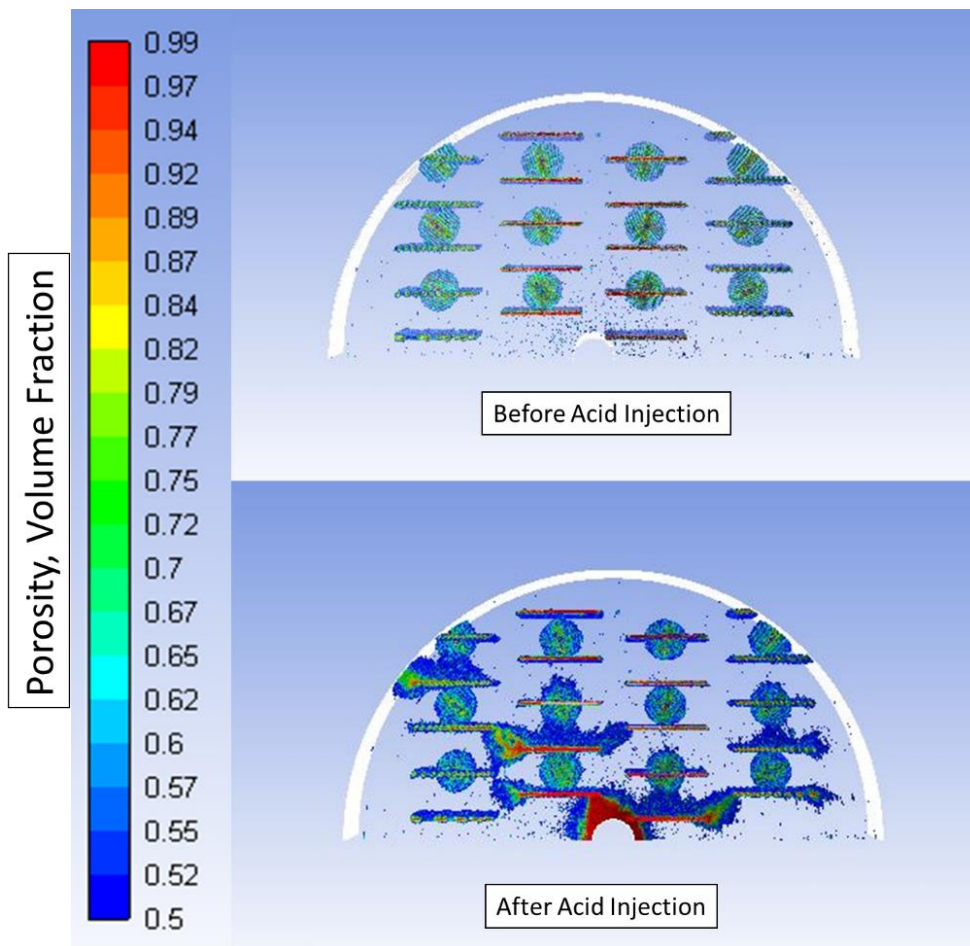
Figure 68Case NFV2 porosity distribution before (top) and after (bottom) acid injection.
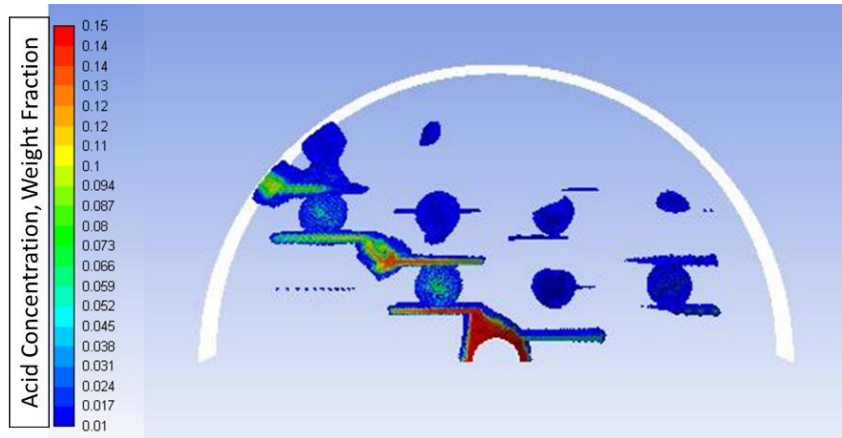
Figure 69 Case NFV2 acid concentration after acid injection.

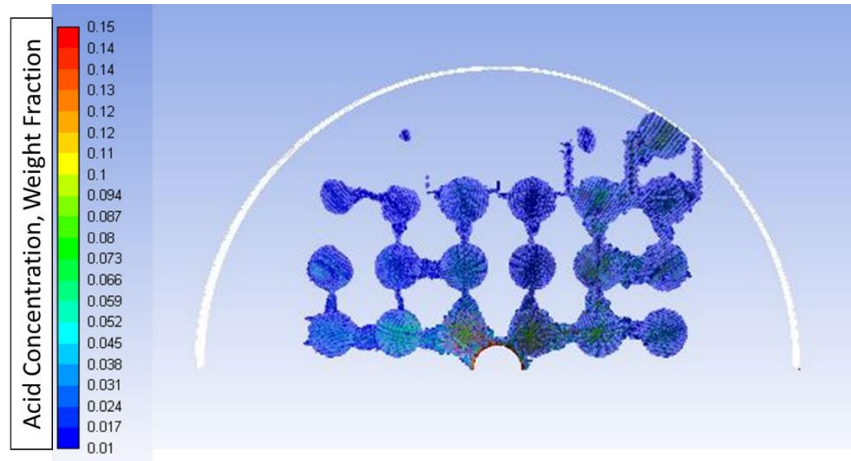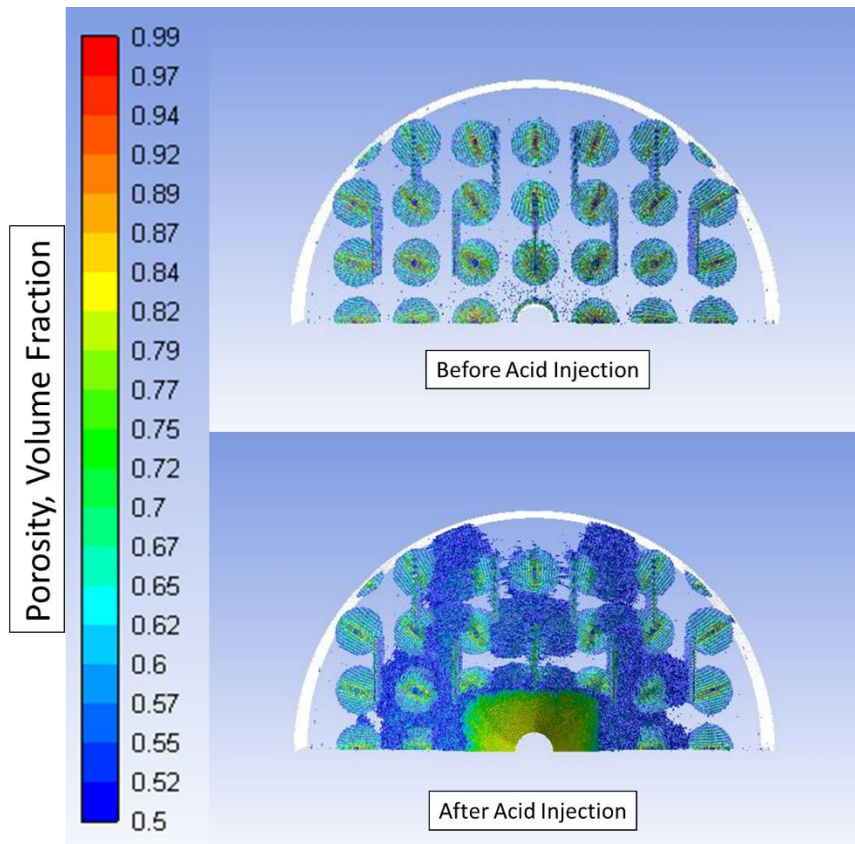**Figure 70 Case NFV3 porosity distribution before (top) and after (bottom) acid injection.**
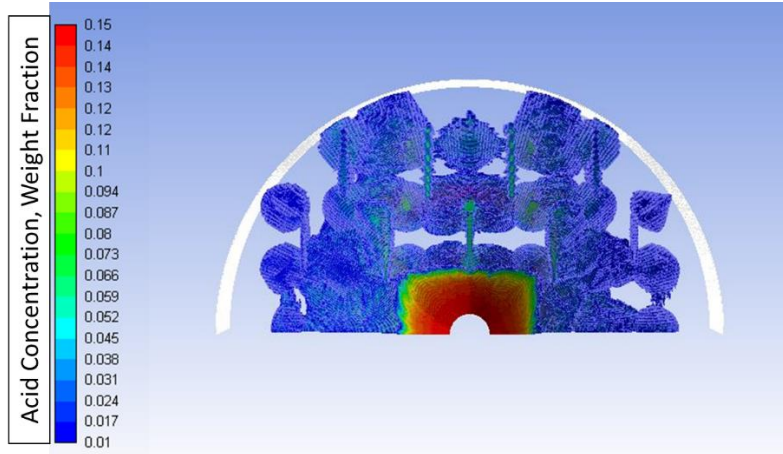
Figure 71 Case NFV3 acid concentration after acid injection.

9. CONCLUSIONS AND RECOMMENDATIONS [7]

The present work examines the simulation of experimental data for dolomite cores using the two-scale model utilizing Navier-Stokes formulation for describing the flow field. A comparison with Maheshwari et al. (2012) study showed that current model always provides lower PVBT. A set of acidizing experiments using dolomite cores were conducted and simulated using the two scale model. The tuning parameters were changed based on experimental data. The model was capable of matching experimental PVBT, along with the 3D wormhole propagation. The model capabilities of matching limestone experiments performed on different rock types were evaluated.

Large scale radial models were used to study acid propagation in the field. Two conditions were studied using the radial model and the results were compared with the traditional upscaling model. The effect of porosity distribution on the model output (PVBT) was investigated. Finally, a robust workflow was introduced for acid stimulation designs.

A 6.5 diameter large scale radial model was utilized to study the effect of vugs and natural fractures on acid flow. The scale of the vugs and fractures presented in the current work is beyond lab capabilities. Thirty-three simulations were run to study the effect of vugs, whereas thirty simulations were run to study the effect of natural fractures. The simulation runs were utilized to build two surrogate models. Three simulation runs were conducted to examine the effect of touching vugs. Based on the work done, the following conclusions can be drawn:

---

1) This model can be tuned using a few acidizing experiments, and then can be used in generating acid efficiency curve with a high degree of confidence, avoiding additional experimental work.

2) The porosity distributions from 7 carbonate rocks have demonstrated that porosity standard deviation can be used as a non-destructive tool for predicting acid performance in carbonates.

3) Current model can be used to predict acid performance in the field scale. the model can capture the wellbore enlargement associated with acidizing operations. Wellbore enlargement may result into crossflow of acid inside the formation.

4) Unlike linear core-flood experiments, deeper acid penetration under field conditions requires smaller pore volume of acid to breakthrough. Optimum PVBT in the field will always be lower than the one obtained from core-flood experiments.

5) The relation between different temperatures and acid concentrations derived from linear lab experiments is not always the same on the field scale.

6) Predicted field volumes using BG and Tardy et al. upscaling models are always higher than predicted using large scale model simulations.

7) Statistically built porosity distribution yield prediction with accuracy higher than 75%. A 25% extra volume can be added during design to consider the uncertainty associated with porosity distributions.

8) There is no direct relation between experimental optimum injection velocity and field optimum injection velocity. The optimum velocity changes experimentally by the change in the core dimensions and in the field by the depth of penetration of the acid.

9) The developed surrogate models can accurately predict acid performance in vuggy and naturally fractured carbonate reservoirs.

10) The effect of the vugs on acidizing can result in lower PVBT at low injection rates ($<=$ 8E-4 m/s) or higher PVBT at high injection rate ($>=$ 8E-2 m/s) when compared with the homogeneous case.

11) High acid concentrations are expected in the flowback after acidizing from vuggy carbonates. Accordingly, longer soaking time should be considered, before flowback from these reservoirs.

12) The effect of natural fractures on the studied injection rates on acidizing is an increase in acid propagation velocity. Acid does not contact all the fractures around the wellbore. The first fracture touched carries all the flow, unless the size and conductivity of the fracture are too small to carry the injected acid volume.

13) The coexistence of vugs and natural fractures lowers the PVBT when compared with the case where only vugs exist. If compared with the case where only fractures exist, the coexistence of vugs and fractures decreases the PVBT at injection rates lower than 8E-3 m/s and increases the PVBT at injection rate higher than 8E-2 m/s.

14) Unlike linear models, the orientation of the fractures and/or vugs does not impact acid performance.

This study furnishes the road for reliable field predictions of acid treatments for relatively homogeneous and extremely heterogeneous carbonate reservoirs. It is recommended to integrate the petrophysical data in the acid design and make use of reactive flow simulators to predict acid propagation under field conditions. Acid volumes predicted from the TSC model should be

multiplied by a safety factor of 1.25 to account for uncertainty associated with porosity

distribution. **Figure 72** introduces an acid stimulation design workflow relatively homogeneous

and extremely heterogeneous carbonate reservoirs. This design can be used in the presence or

absence of rock samples from the field. The workflow integrates the experimental, petrophysical,

and simulation studies in one platform to achieve accurate/reliable acid stimulation designs.
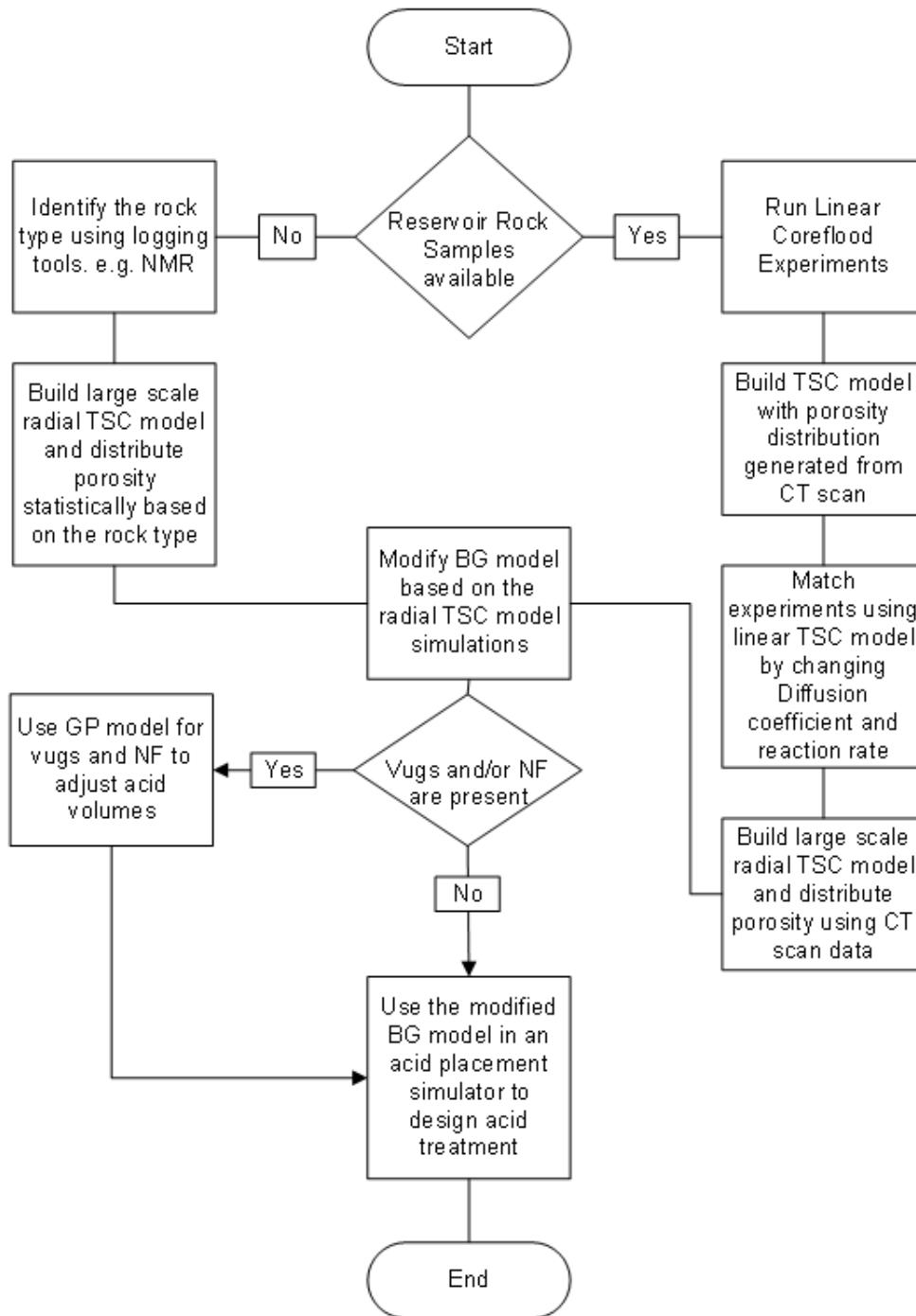
Figure 72 A petrophysical, experimental, and simulation-based workflow for acid design in carbonate formations.

REFERENCES

Aidagulov, G., Gwaba, D., Kayumov, R., et al. 2019. Effects of Pre-Existing Fractures on Carbonate Matrix Stimulation Studied by Large-Scale Radial Acidizing Experiments. Presented at the SPE Middle East Oil and Gas Show and Conference, Manama, Bahrain. SPE-163380-MS, 18-21 March. http://dx.doi.org/10.2118/195153-MS.

Akanni, O. O. and Nasr-El-Din, H. A. 2015. The Accuracy of Carbonate Matrix-Acidizing Models in Predicting Optimum Injection and Wormhole Propagation Rates. Presented at the SPE Middle East Oil & Gas Show and Conference. Manama, Bahrain, 8–11 March. SPE 172575-MS. http://dx.doi.org/10.2118/172575-MS.

Akanni, O. O., Nasr-El-Din, H. A. and Gusain, D. 2017. A Computational Navier-Stokes Fluid Dynamics Simulation Study of Wormhole Propagation in Carbonate Matrix Acidizing and Analysis of Factors Influencing the Dissolution Process. *SPE J.* **22** (6): 2049-2066. SPE-187962-PA. http://dx.doi.org/10.2118/187962-PA.

Akin, S. and Kovscek, A. 2003. Computed Tomography in Petroleum Engineering Research. Geological Society, London Special Publications 215:23-38. http://dx.doi.org/10.1144/GSL.SP.2003.215.01.03.

Ali, M. T. and Nasr-El-Din, H. A. 2019. A Robust Model to Simulate Dolomite-Matrix Acidizing. *SPE Prod & Oper* **34** (01): 109-129. SPE-191136-PA. http://dx.doi.org/10.2118/191136-PA.

Al-Muraikhi, H. R., Joshi, D., and Al-bloushi A. F. 2012. Integrated Workflow for Small Scale Reservoir Characterization Using borehole Image, NMR and Core Data. Presented at the SPE Kuwait International Petroleum Conference and Exhibition, Kuwait City, Kuwait, 10-12 December. SPE-163380-MS. http://dx.doi.org/10.2118/163380-MS.

Arbogast, T. and Brunson, D. 2007. A Computational Method for Approximating a Darcy–Stokes System Governing a Vuggy Porous Medium. *Computational Geosciences* **11** (3): 207–218. http://dx.doi.org/10.1007/s10596-007-9043-0.

Balakotaiah, V. and West, D. H. 2002. Shape Normalization and Analysis of Mass Transfer Controlled Regime in Catalytic Monoliths. *Chem Eng Sci* **57** (8): 1269-1286. http://dx.doi.org/10.1016/S0009-2509(02)00059-3.

Bazin, B. 2001. From Matrix Acidizing to Acid Fracturing: A Laboratory Evaluation of Acid/Rock Interactions. *SPE Prod & Fac* **16** (01): 22-29. SPE-66566-PA. http://dx.doi.org/10.2118/66566-PA.

Beletskaya, A., Ivanov, E., Stukan, M. et al. 2017. Reactive Flow Modeling at Pore Scale. Presented at the Russian Petroleum Technology Conference, Moscow, Russia, 16-18 October. SPE-187805-MS. http://dx.doi.org/10.2118/187805-MS.

Brinkman, H. C. 1949. A Calculation of the Viscous Force Exerted by a Flowing Fluid on a Dense Swarm of Particles. *Applied Scientific Research* **1** (1): 27–34. http://dx.doi.org/10.1007/BF02120313.

Buijse, M. A. and Glasbergen, G. 2005. A Semi-Empirical Model to Calculate Wormhole Growth in Carbonate Acidizing. Presented at the SPE Annual Technical Conference and Exhibition, Dallas, Texas, 9-10 October. SPE 96892-MS. http://dx.doi.org/10.2118/96892-MS.

Camacho-Velazquez, R., Vasquez-Cruz, M. A., Castrejon-Aivar, R. et al. 2005. Pressure Transient and Decline Curve Behaviors in Naturally Fractured Vuggy Carbonate Reservoirs. *SPE Res Eval & Eng* **8** (02): 95-112. SPE-77689-PA. http://dx.doi.org/10.2118/77689-PA.

Cannon, D. E., Minh, C. C., and Kleinberg, R. L. 1998. Quantitative NMR Interpretation. Presented at the SPE Annual Technical Conference and Exhibition, New Orleans, Louisiana, 27-30 September. SPE-49010-MS. http://dx.doi.org/10.2118/49010-MS.

Carman, C. 1956. *Flow of Gases through Porous Media*, first edition. New York: Academic Press.

Chen, Y., Ma, G., Li, T., et al. 2018. Simulation of Wormhole Propagation in Fractured Carbonate Rocks with Unified Pipe-Network Method. *Computers and Geotechnics* **98**: 58-68. https://doi.org/10.1016/j.compgeo.2017.11.009.

Cohen, C.E., Ding, D., Quintard, M. et al. 2008. From Pore Scale to Wellbore Scale: Impact of Geometry on Wormhole Growth in Carbonate Acidization. Chem. Eng. Sc. 63 (12) 3088. http://dx.doi.org/10.1016/j.ces.2008.03.021.

Daccord, G. 1987. Chemical dissolution of a porous medium by a reactive fluid. *Phys. Rev. Lett*. **58**: 479

Daccord, G., Lenormand, R., and Liétard, O. 1993. Chemical Dissolution of a Porous Medium by a Reactive Fluid—I. Model for the "Wormholing" Phenomenon. *Chem. Eng. Sci.* **48** (1): 169-178. http://dx.doi.org/10.1016/0009-2509(93)80293-Y.

De Oliveira, T., De Melo, A., Oliveira, J. et al. 2012. Numerical Simulation of the Acidizing Process and PVBT Extraction Methodology Including Porosity/Permeability and Mineralogy Heterogeneity. Presented at the International Symposium and Exhibition on Formation Damage Control. Lafayette, Louisiana. 15–17 January. SPE 151823-MS. http://dx.doi.org/10.2118/151823-MS.

Dong, C., Hill, A. D., and Zhu, D. 1999. Acid Etching Patterns in Naturally-Fractured Formations. Presented at the SPE Annual Technical Conference and Exhibition, Houston, Texas, 3-6 October. SPE-56531-MS. http://dx.doi.org/10.2118/56531-MS.

Dong, C., Zhu, D., and Hill, A. D. 2001. Acid Penetration in Natural Fracture Networks. SPE European Formation Damage Conference, The Hague, Netherlands, 21-22 May. SPE-68927-MS. http://dx.doi.org/10.2118/68927-MS.

Dong, K., Jin, X., Zhu, D., et al. 2014.The Effect of Core Dimensions on the Optimal Acid Flux in Carbonate Acidizing. Presented at the International Symposium and Exhibition on Formation Damage Control. Lafayette, Louisiana. 26–28 February. SPE-168146-MS. https://doi.org/10.2118/168146-MS.

Dong, R., Lee, S., and Wheeler, M. 2019. Numerical Simulation of Matrix Acidizing in Fractured Carbonate Reservoirs Using Adaptive Enriched Galerkin Method. Presented at the SPE Reservoir Simulation Conference, Galveston, Texas, 10-11 April. SPE-193862-MS.. http://dx.doi.org/10.2118/193862-MS.

Fadlelmula F., Fraim, M., He, J., et al. 2015. Discrete Fracture-Vug Network Modeling in Naturally Fractured Vuggy Reservoirs Using Multiple-Point Geostatistics: A Micro-Scale Case. Presented at the SPE Annual Technical Conference and Exhibition, Houston, Texas, 28-30 September. SPE-175092-MS. http://dx.doi.org/10.2118/175092-MS.

Fredd, C. N. and Fogler, H. S. 1998. Influence of Transport and Reaction on Wormhole Formation in Porous Media. *AIChE J.* **44** (9): 1933. http://dx.doi.org/10.1002/aic.690440902.

Fredd, C. N. and Fogler, H. S. 1999. Optimum Conditions for Wormhole Formation in Carbonate Porous Media: Influence of Transport and Reaction. *SPE J.* **4** (3): 196-205. SPE-56995-PA. http://dx.doi.org/10.2118/56995-PA.

Fredd, C. N. and Miller, M. J. 2000. Validation of Carbonate Matrix Stimulation Models. Presented at the International Symposium on Formation Damage Control, Lafayette, Louisiana, 23 – 24 February. SPE 58713-MS. http://dx.doi.org/10.2118/58713-MS.

Furui, K., Burton, R., Burkhead, D. et al. 2012. A Comprehensive Model of High-Rate Matrix-Acid Stimulation for Long Horizontal Wells in Carbonate Reservoirs: Part I--Scaling Up Core-Level Acid Wormholing to Field Treatments. *SPE J.* **17** (1): 271-279. http://dx.doi.org/10.2118/134265-PA.

Ghommem, M., Qiu, X., Brady, D. et al. 2016. Monitoring of Matrix Acidizing by Using Resistivity Measurements. Society of Petroleum Engineers. http://dx.doi.org/10.2118/181414-MS.

Ghommem, M., Zhao, W., Dyer, S. et al. 2015. Carbonate acidizing: Modeling, analysis, and characterization of wormhole formation and propagation. *J Pet Sci Eng* **131**: 18-33. http://dx.doi.org/j.petrol.2015.04.021.

Golfier, F., Zarcone, C., Bazin, B. et al. 2002. On the Ability of a Darcy-Scale Method Model to Capture Wormhole Formation During the Dissolution of a Porous Medium. *J. Fluid Mech.* **457**: 213-254. http://dx.doi.org/10.1017/S0022112002007735.

Gomaa, N. M., Azer, S. R., Ouzzane, D. E., et al. 2006. Case Study of Permeability, Vug Quantification, and Rock Typing in a Complex Carbonate. Presented at the SPE Annual Technical Conference and Exhibition, San Antonio, Texas, 21-24 September. SPE-102888-MS. http://dx.doi.org/doi:10.2118/102888-MS.

Gupta, N. and Balakotaiah, V. 2001. Heat and Mass Transfer Coefficients in Catalytic Monoliths. *Chem Eng Sci* **56** (16): 4771-4786. http://dx.doi.org/10.1016/S0009-2509(01)00134-8.

Hoefner, M. L. and Fogler, H. S. 1988. Pore Evolution and Channel Formation During Flow and Reaction in Porous Media. *AIChE J.* **34** (1): 45-54. http://dx.doi.org/10.1002/aic.690340107.

Huang, T., Hill, D., and Schechter, S. 1997. Reaction Rate and Fluid Loss: The Keys to Wormhole Initiation and Propagation in Carbonate Acidizing. Presented at the International Symposium

on Oilfield Chemistry, Houston, Texas, 18 – 21 February. SPE 37312-MS. http://dx.doi.org/10.1016/10.2118/37312-MS.

Huang, Z., Yao, J., Li, Y. et al. 2011. Numerical Calculation of Equivalent Permeability Tensor for Fractured Vuggy Porous Media Based on Homogenization Theory. *Communications in Computational Physics* **9** (01): 180-204. http://dx.doi.org/10.4208/cicp.150709.130410a.

Hung, K. M., Hill, A. D., and Sepehrnoori, K. 1989. A Mechanistic Model of Wormhole Growth in Carbonate Matrix Acidizing and Acid Fracturing. *J Pet Technol* **41** (1): 59-66. SPE-16886-PA. http://dx.doi.org/2118/16886-PA.

Ibrayev, F., Fernandez-Ibanez, F., and DeGraff, J. M. 2016. Using a Genetic-Based Approach to Enhance Natural Fracture Characterization in a Giant Carbonate Field. Presented at the SPE Annual Caspian Technical Conference and Exhibition, Astana, Kazakhstan, 1-3 November. SPE-182565-MS. http://dx.doi.org/10.2118/182565-MS.

Iwere, F. O., Moreno, J. E., Apaydin, O. G., et al. 2002. Vug Characterization and Pore Volume Compressibility for Numerical Simulation of Vuggy and Fractured Carbonate Reservoirs. Presented at the SPE International Petroleum Conference and Exhibition, Villahermosa, Mexico, 10-12 February. SPE-74341-MS. http://dx.doi.org/10.2118/74341-MS.

Izgec, O., Zhu, D., and Hill, A. D. 2010. Numerical and Experimental Investigation of Acid Wormholing during Acidization of Vuggy Carbonate Rocks. *J Pet Sci Eng* **74** (1): 51-66. http://dx.doi.org/10.1016/j.petrol.2010.08.006.

Kalia, N. and Balakotaiah, V. 2009. Effect of Medium Heterogeneities on Reactive Dissolution of Carbonates. *Chem Eng Sci* **64** (2): 376-390. http://dx.doi.org/10.1016/j.ces.2008.10.026.

Kalia, N. and Glasbergen, G. 2009. Wormhole Formation in Carbonates under Varying Temperature Conditions. Presented at the 8th European Formation Damage Conference.

Scheveningen, The Netherlands, 27–29 May. SPE 121803-MS. http://dx.doi.org/10.2118/121803-MS.

Kang, Z., Wu, Y.-S., Li, J. et al. 2006. Modeling Multiphase Flow in Naturally Fractured Vuggy Petroleum Reservoirs. Presented at the SPE Annual Technical Conference and Exhibition, San Antonio, Texas, 24-27 September. SPE-102356-MS. http://dx.doi.org/10.2118/102356-MS.

Liu, M., Zhang, S., and Mou, J. 2012. Effect of Normally Distributed Porosities on Dissolution Pattern in Carbonate Acidizing. *J Pet Sci Eng* **94–95** (0): 28-39. http://dx.doi.org/10.1016/j.petrol.2012.06.021.

Liu, P., Xue, H., Zhao, L., et al. 2016. Simulation of 3D multi-scale wormhole propagation in carbonates considering correlation spatial distribution of petrophysical properties. *J Natural Gas Sci Eng* **32**: 81-94, https://doi.org/10.1016/j.jngse.

Liu, X., Ormond, A., Bartko, K. et al. 1997. A Geochemical Reaction-Transport Simulator for Matrix Acidizing Analysis and Design. *J Pet Sci Eng* **17** (1–2): 181-196. http://dx.doi.org/10.1016/S0920-4105(96)00064-2.

Lucia, F. J. 2007. *Carbonate Reservoir Characterization*. 2nd edition. New York: Springer.

Lund, K., Fogler, S. and McCune, C. 1973. Acidization I. The Dissolution of Dolomite in Hydrochloric Acid. *Chem. Eng. Sci.* **28**: 691-700.

Lund, K., Fogler, S., McCune, C. et al. 1975. Acidization II. The Dissolution of Calcite in Hydrochloric Acid. *Chem. Eng. Sci.* **28**: 691-700.

Ma, G., Chen, Y., Jin, Y., et al. 2018. Modelling Temperature-Influenced Acidizing Process in Fractured Carbonate Rocks. *International J. Rock Mechanics and Mining Sciences* **105**: 73-84. https://doi.org/10.1016/j.ijrmms.2018.03.019.

Maheshwari, P. and Balakotaiah, V. 2013. Comparison of Carbonate HCl Acidizing Experiments with 3D Simulations. *SPE Prod & Oper* **28** (04): 402-413. SPE-164517-PA. http://dx.doi.org/10.2118/164517-PA.

Maheshwari, P., Gharbi, O., Thirion, A. et al. 2016. Development of a Reactive Transport Simulator for Carbonates Acid Stimulation. Society of Petroleum Engineers. http://dx.doi.org/10.2118/181603-MS.

Maheshwari, P., Ratnakar, R. R., Kalia, N. et al. 2012. 3-D Simulation and Analysis of Reactive Dissolution and Wormhole Formation in Carbonate Rocks. *Chem Eng Sci* **90** (0): 258-274. http://dx.doi.org/10.1016/j.ces.2012.12.032.

Mahrous, M., Sultan, A. and Sonnenthal, E. 2017. Towards Geochemically Accurate Modeling of Carbonate Acidizing with HCl Acid. Presented at the Annual Technical Conference and Exhibition, San Antonio, Texas, 9–11 October. SPE-187183-MS. http://dx.doi.org/10.2118/187183-MS.

Mai, A., and Kantzas, A. 2002. Porosity Distribution of Carbonate Reservoirs Using Low Field NMR. Presented at the Canadian International Petroleum Conference, Calgary, Alberta, 11-13 June. PETSOC-2002-193. http://dx.doi.org/10.2118/2002-193.

Mai, A., and Kantzas, A. 2003. Advances in Carbonate Characterization Using Low Field NMR. Presented at the Canadian International Petroleum Conference, Calgary, Alberta, 10-12 June. PETSOC-2003-106. http://dx.doi.org/ 10.2118/2003-106.

McCune, C., Fogler, S. and Kline, E. 1979. An Experimental Technique for Obtaining Permeability-Porosity Relationships in Acidized Porous Media. *Industrial Engineering Chemistry Fundamentals* **18** (2): 188–191. http://dx.doi.org/10.1021/i160070a016.

McDuff, D., Jackson, S., Shuchart, C. et al. 2010. Understanding Wormholes in Carbonates: Unprecedented Experimental Scale and 3D Visualization. *J Pet Technol* **62** (10)*:* 78-81. SPE-129329-JPT. http://dx.doi.org/10.2118/ 62 (10: 129329-JPT.

Nair, N. G., Bryant, S. L., and Jennings, J. W. 2008. Finding the Continuum Scale in Highly Heterogeneous Rocks: Example of a Large Touching Vug Carbonate. Presented at the SPE Annual Technical Conference and Exhibition, Denver, Colorado, 21-24 September. SPE-115347-MS. https://doi.org/10.2118/115347-MS.

Narr, W., Schechter, D. S., and Thompson, L. B. 2006. *Naturally Fractured Reservoir Characterization*. Society of Petroleum Engineers: Richardson, TX.

Nishikata, E., Ishii, T., Ohta, T. 1981. Viscosities of aqueous hydrochloric acid solutions, and densities and viscosities of aqueous hydroiodic acid solutions. *J Chem Eng Data* **26** (3): 254–256. https://doi.org/10.1021/je00025a008.

Panga, M. K. R., Balakotaiah, V., and Ziauddin, M. 2002. Modeling, Simulation and Comparison of Models for Wormhole Formation during Matrix Stimulation of Carbonates. Presented at the SPE Annual Technical Conference and Exhibition, San Antonio, Texas. 29 September-2 October. SPE 77369-MS http://dx.doi.org/10.2118/77369-MS.

Panga, M. K. R., Ziauddin, M., and Balakotaiah, V. 2005. Two-Scale Continuum Model for Simulation of Wormholes in Carbonate Acidization. *AIChE J.* **51** (12): 3231-3248. http://dx.doi.org/10.1002/aic.10574.

Popov, P., Qin, G., Bi, L. et al. 2007. Multiscale Methods for Modeling Fluid Flow through Naturally Fractured Carbonate Karst Reservoirs. Presented at the SPE Annual Technical Conference and Exhibition, Anaheim, California, 11-14 November. SPE-110778-MS. http://dx.doi.org/10.2118/110778-MS.

Qi, N., Chen, G., Liang, C., et al. 2019. Numerical simulation and analysis of the influence of fracture geometry on wormhole propagation in carbonate reservoirs. *Chem. Eng. Sci.* **198**: 124-143.

Rasmussen, E. C. and Williams, C. 2006. *Gaussian Processes for Machine Learning*. Boston: The MIT Press.

Rötting, T., Luquot, L., Carrera, J. et al., 2015. Changes in porosity, permeability, water retention curve and reactive surface area during carbonate rock dissolution. *Chemical Geology* **403**: 86-98. http://dx.doi.org/10.1016/j.chemgeo.2015.03.008.

Safari, A., Dowlatabad, M. M., Hassani, A., et al. 2016. Numerical simulation and X-ray imaging validation of wormhole propagation during acid core-flood experiments in a carbonate gas reservoir. *J Natural Gas Sci and Eng* **30**: 539-547, https://doi.org/10.1016/j.jngse.2016.02.036.

Safari, A., Rashidi, F., Kazemzadeh, E., et al. 2014. Determining optimum acid injection rate for a carbonate gas reservoir and scaling the result up to the field conditions: A case study. *J Natural Gas Sci Eng* **20**: 2-7. https://doi.org/10.1016/j.jngse.2014.05.017.

Santner, T., Williams, B., and Notz, W. 2013. *The Design and Analysis of Computer Experiments*. New York: Springer Science and Business Media.

Schwalbert, P., Zhu, D., and Hill, A. D. 2017. Extension of an Empirical Wormhole Model for Carbonate Matrix Acidizing Through Two-Scale Continuum 3D Simulations. Society of Petroleum Engineers. http://dx.doi.org/10.2118/185788-MS.

Shafiei, A., and Dusseault, M. B. 2012. Natural Fractures Characterization in a Carbonate Heavy Oil Field. Presented at the 46th U.S. Rock Mechanics/Geomechanics Symposium, Chicago, Illinois, 24-27 June. ARMA-2012-433.

Tansey, J. 2014. Pore-Network Modeling of Carbonate Acidization. Society of Petroleum Engineers. http://dx.doi.org/10.2118/173472-STU .

Tardy, P., Lecerf, B. and Christanti, Y. 2007. An Experimentally Validated Wormhole Model for Self-Diverting and Conventional Acids in Carbonate Rocks under Radial Flow Conditions. Presented at the European Formation Damage Conference, Scheveningen, The Netherlands, 30 May–1 June. SPE-107854-MS. http://dx.doi.org/10.2118/107854-MS.

Taylor, K. C., Nasr-El-Din, H. A., and Mehta, S. 2006. Anomalous Acid Reaction Rates in Carbonate Reservoir Rocks. Society of Petroleum Engineers. http://dx.doi.org/10.2118/89417-PA.

Wang, Y., Hill, D., and Schechter, S. 1993. The Optimum Injection Rate for Matrix Acidizing of Carbonate Formations. Presented at the SPE Annual Technical Conference and Exhibition, Houston, Texas, 3-6 October. SPE 26578-MS. http://dx.doi.org/10.2118/26578-MS.

Wang, Y., Hill, D., and Schechter, S. 1993. The Optimum Injection Rate for Matrix Acidizing of Carbonate Formations. Presented at the SPE Annual Technical Conference and Exhibition, Houston, Texas, 3-6 October. SPE 26578-MS. http://dx.doi.org/10.2118/26578-MS.

Wang, Z. 2011. *Study of Acid Response of Qatar Carbonate Rocks*. MS thesis, Texas A&M University, College Station, Texas (December 2011).

Wu, Y., Salama, A., and Sun, S. 2015. Parallel simulation of wormhole propagation with the Darcy–Brinkman–Forchheimer framework. *Computers and Geotechnics* **69**: 564-577. https://doi.org/10.1016/j.compgeo.

Yao, J., Huang, Z., Li, Y., et al. 2010. Discrete Fracture-Vug Network Model for Modeling Fluid Flow in Fractured Vuggy Porous Media. Presented at the International Oil and Gas Conference and Exhibition, Beijing, China, 8-10 June. SPE-130287-MS.

Yong, L., Baozhu, L., Jing, X., et al. 2016. Development Strategy Optimization and Application for Fractured-Vuggy Carbonate Gas Condensate Reservoirs. Presented at the Russian Petroleum Technology Conference, Moscow, Russia, 24-26 October.

Zakaria, A. S., Nasr-El-Din, H. A. and Ziauddin, M. E. 2015. Predicting the Performance of the Acid-Stimulation Treatments in Carbonate Reservoirs With Nondestructive Tracer Tests. *SPE J.* **20** (06): 1238-1253. SPE-174084-PA. http://dx.doi.org/10.2118/174084-PA.

Zakaria, A. S., Sayed, M., and Nasr-El-Din, H. A. 2014. New Insights into Propagation of Emulsified Acids in Vuggy Dolomitic Rocks. *SPE J.* **19** (01): 150-160. SPE-163288-PA. http://dx.doi.org/10.2118/163288-PA.

Zhang, J., Ma, P., Liu, Y., et al. 2016. Control Modes of Multitype Strike-Slip Fault Systems on Fractured-Vuggy Carbonate Reservoir Development. Presented at the 2016 SEG International Exposition and Annual Meeting, Dallas, Texas, 16-21 October. SEG-2016-13879380.

Ziauddin, M. E. and Bize, E. 2007. The Effect of Pore Scale Heterogeneities on Carbonate Stimulation Treatments. Society of Petroleum Engineers. Presented at the SPE Middle East Oil and Gas Show and Conference, Manama, Bahrain, 11-14 March. SPE-104627-MS. https://doi.org/10.2118/104627-MS.